Annual Report 2023/2024

Institute for Pulsed Power and Microwave Technology
Institut für Hochleistungsimpuls- und Mikrowellentechnik

John Jelonnek (ed)

Institute for Pulsed Power and Microwave Technology (IHM)

Institut für Hochleistungsimpuls- und Mikrowellentechnik (IHM)

Director: Prof. Dr.-Ing. John Jelonnek

The Institute for Pulsed Power and Microwave Technology (Institut für Hochleistungsimpuls- und Mikrowellentechnik, IHM) is working in the areas of pulsed power and high-power microwave technologies. Both, research and development of high-power sources and related applications are in the focus. Applications for pulsed power technologies are ranging from materials processing to bioelectrics. High-power microwave technologies are focusing on microwave sources (gyrotrons) for electron cyclotron resonance heating of magnetically confined plasmas and on applications for materials processing at microwave frequencies.

IHM is doing research, development, academic education, and, in close collaboration with the KIT division IMA and industrial partners, technology transfer. The focus is on the long-term goals of the Helmholtz Association of German Research Centres (HGF). During the currently running Program-Oriented Funding period (POF4), IHM is doing research work in the HGF programs "Nuclear Fusion (FUSION)", "Nuclear Waste Management, Safety and Radiation Research (NUSAFE)" and "Materials and Technologies for the Energy Transition (MTET)".

Projects funded by third-parties complement significantly the research work within all the different HGF programs. Considering the pulsed power technology and related applications, that includes the research on e.g. microalgae processing at large-scale relevant for industrial processes, the PEF-assisted extraction of valuable compounds and the development of powerful semiconductor-based marx-type pulse generators. Additionally, it includes the development of new materials that mitigate corrosion while being in contact with liquid metals and salts as required for future liquid metal batteries and the technical feasibility and scaling of CO_2-free methane pyrolysis in liquid high-temperature Sn respectively.

Considering the application of high-power microwaves to new and innovative energy-efficient industrial processes, third-party projects include the research on e.g. microwave assisted intermittent pultrusion of CFRP profiles, microwave assisted additive manufacturing with continuous carbon fiber reinforced thermoplastic filaments and the controlling and demolition of the distribution of weeds in crop fields.

All research areas are strongly interdisciplinary and require the profound knowledge on modern electron beam optics, high-power microwave technologies, vacuum electronics, material technologies, high voltage technologies and high voltage measurement techniques.

Table of Contents

1 Nuclear Fusion (FUSION): Microwave Plasma Heating

Contact: Prof. Dr.-Ing. John Jelonnek / Dr. Gerd Gantenbein (until May 2024)

The department for high-power microwave technology focuses on the research and development of high-power microwave sources (gyrotrons) and related components for electron cyclotron resonance heating and current drive (ECRH&CD) of magnetically confined nuclear fusion plasmas. Additionally, it includes the fundamental research on gyro-amplifiers for spectroscopy and space radar.

Following major activities have been carried out during the years 2023 and 2024:

- Finalization, initialization, conditioning and start of FULGOR, the most powerful and versatile gyrotron teststand in the world today
- Support in the finalization of the 1 MW 170 GHz hollow-cavity gyrotron for ITER
- R&D towards a DEMO relevant gyrotron within the EUROfusion Work Package Heating and Current Drive (WP HCD):
  - 2 MW-class multi-purpose and frequency step-tunable coaxial-cavity gyrotron technology operating at center frequencies of 136/170/204 GHz and up to 238 GHz
  - Development and validation of gyrotron key components
  - Design and manufacturing of the first-of-its-kind Multistage Depressed Collector (MDC) as key component for future highly efficient operating gyrotrons
  - Quasi-optical mode converters, broadband windows and Matching Optical Units including the advancement of simulation tools for the analysis of passive quasi-optical components
  - DEMO EC system design and collaboration with DEMO physics towards a widely usable flight simulator for different tokamaks and configurations
- Advanced developments towards a significant 1.5 MW, 140 GHz gyrotron upgrade for W7-X in collaboration with IPP Greifswald and NKUA, Athens and within EUROfusion WP W7X
- Design and validation of the first European 1 MW, 104 GHz industrial gyrotron for WEST in close collaboration with CEA, Cadarache, and NKUA, Athens
- Design of a first European 1 MW 117.5 GHz industrial gyrotron for DIII-D
- Fundamental research on megawatt-class fusion gyrotron systems based on highly efficient operation at the second harmonic of the cyclotron frequency in collaboration with NKUA, Athens and within an EUROfusion Enabling Research (ENR)
- Frequency stabilization of megawatt-class gyrotrons with a phase-locked loop for Collective Thomson Scattering (CTS) at W7-X in collaboration with IPP Greifswald and within an EUROfusion Engineering Grant (EEG)
- Theoretical pre-study for a first 240 GHz gyrotron for Proxima Fusion
- Fundamental research on a gyro-travelling wave tube with a helically corrugated interaction region at 263 GHz and 1 kW for the DFG SFB 1527 HyPERiON project

1.1 Parasitic free operation of the 1 MW, 170 GHz short-Pulse pre-prototype for ITER

Contact: Dr. Tomasz Rzesnicki

The effective suppression of the excitation of parasitic oscillations is one of the most important aspects during the design process of a gyrotron tube. In the most cases, the parasitic modes are directly responsible for a significant degradation of the gyrotron performance and reduction of the efficiency in the output power generation. The excitation of the parasitic oscillations in the gyrotron is mainly related to the combined beam-tunnel and cavity region, which is very challenging for numerical modelling and analysis. Therefore, a much more intensive experimental investigation on the possibilities to avoid the spurious modes in the gyrotron has been started. Within these activities, several versions of the setups, including different beam-tunnels and cavity designs, have already been experimentally tested with the 1 MW, 170 GHz short-pulse (SP) gyrotron pre-prototype available at KIT (see Fig. 1.1.1).
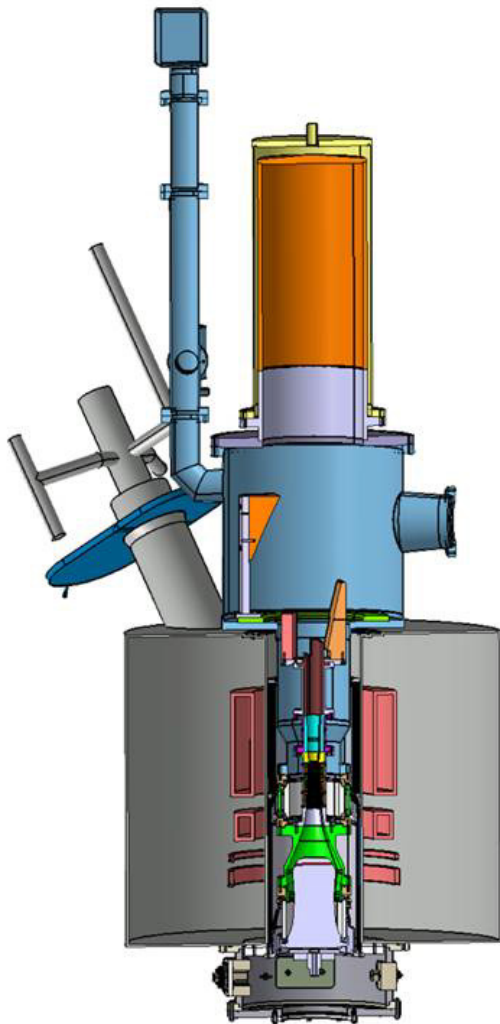
Fig. 1.1.1:   EU 1 MW short-pulse gyrotron prototype for ITER.

The problematic gyrotron area, susceptible to an excitation of parasitic modes, is concentrated close to the maximum magnetic field, between the beam tunnel and gyrotron cavity. The current and most common design of the beam tunnel structure consists of a stacked combination of copper and ceramic rings, ended up with the so-called spacer as a transition-part to the cavity. Recent theoretical studies have shown, that the so-called down-taper part of the cavity, could also contribute to the excitation of spurious backward-wave mode oscillations, even inside the cavity section. Taking into account the results of the theoretical analysis in combination with the findings and observations collected over the years during several experimental campaigns a new version of the beam tunnel combined with an optimized cavity and spacer design has been proposed. Following modifications have been introduced in the gyrotron setup:

a) the copper-ceramic structure is optimized in order to maximize its absorption capability at the parasitic frequencies
b) an alternative profile is introduced on the inner spacer wall, that additionally minimizes the risk for the parasitic excitation
c) the down-taper of the cavity section is optimized numerically in order to minimize the possibility of excitation of backward-wave modes
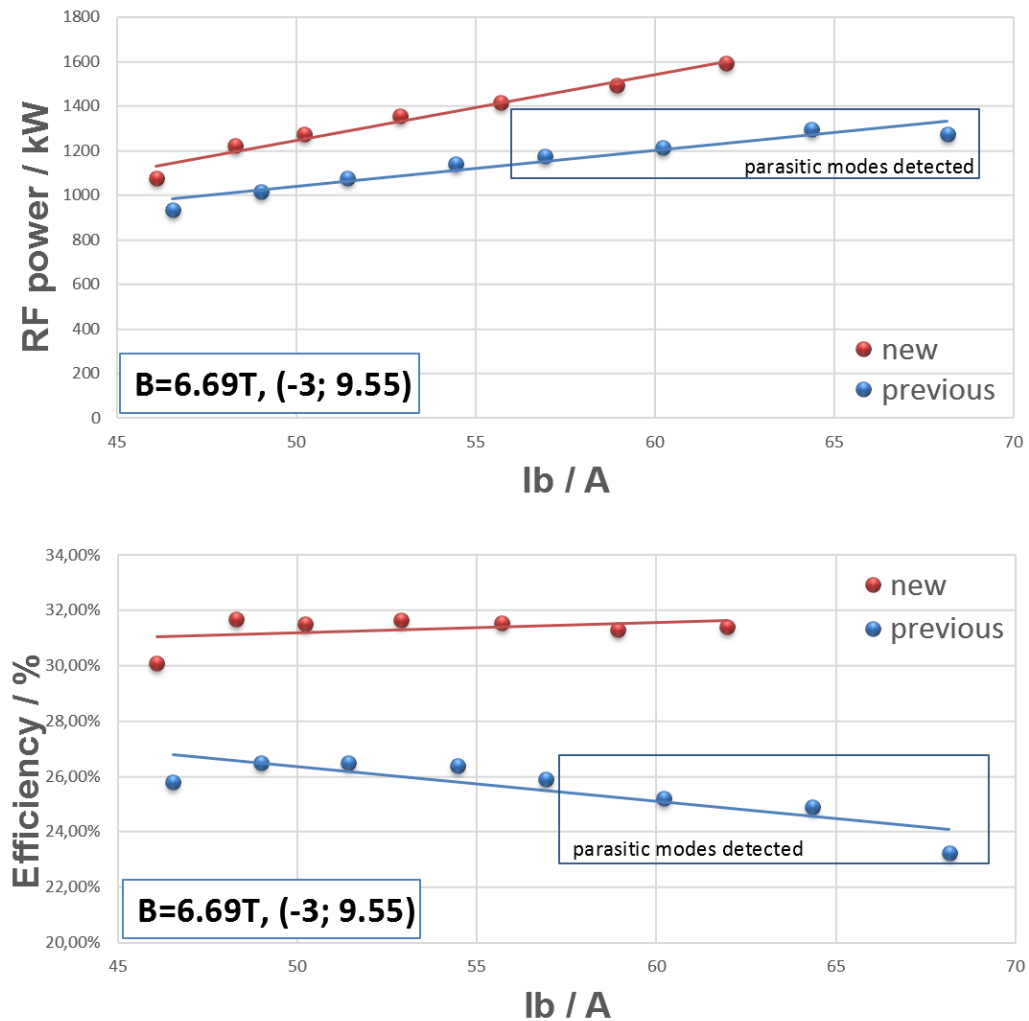
Fig. 1.1.2:   An example of measured RF power and efficiency vs. beam current, with visible saturation effect due to parasitic mode excitation.

The experimental verification is performed by using the modular short-pulse pre-prototype that is shown in Fig. 1.1.1. The gyrotron is operated in short-pulse regime (~1 ms) and at electron beam values between 45 A (nominal value) and slightly above 60 A. This is done in order to validate a safety margin for the possible excitation of parasitic modes. A comparison of the achieved power and efficiency versus the electron beam current for the new and previous gyrotron configurations are presented in Fig. 1.1.2. The gyrotron is able to generate output power in the range of 1.6 MW, hence it demonstrated a much higher efficiency than in the previous configuration without any parasitic modes. It resulted in a much more stable operation without any degradation and saturation effects on the output power and efficiency versus beam current.

In addition, the gyrotron is operated in depressed operation scheme. Due to much better stability of the operation due to suppression of the parasitic modes, for the first time the overall efficiency of the gyrotron is above of 50 %, as it is shown in the Fig. 1.1.3.
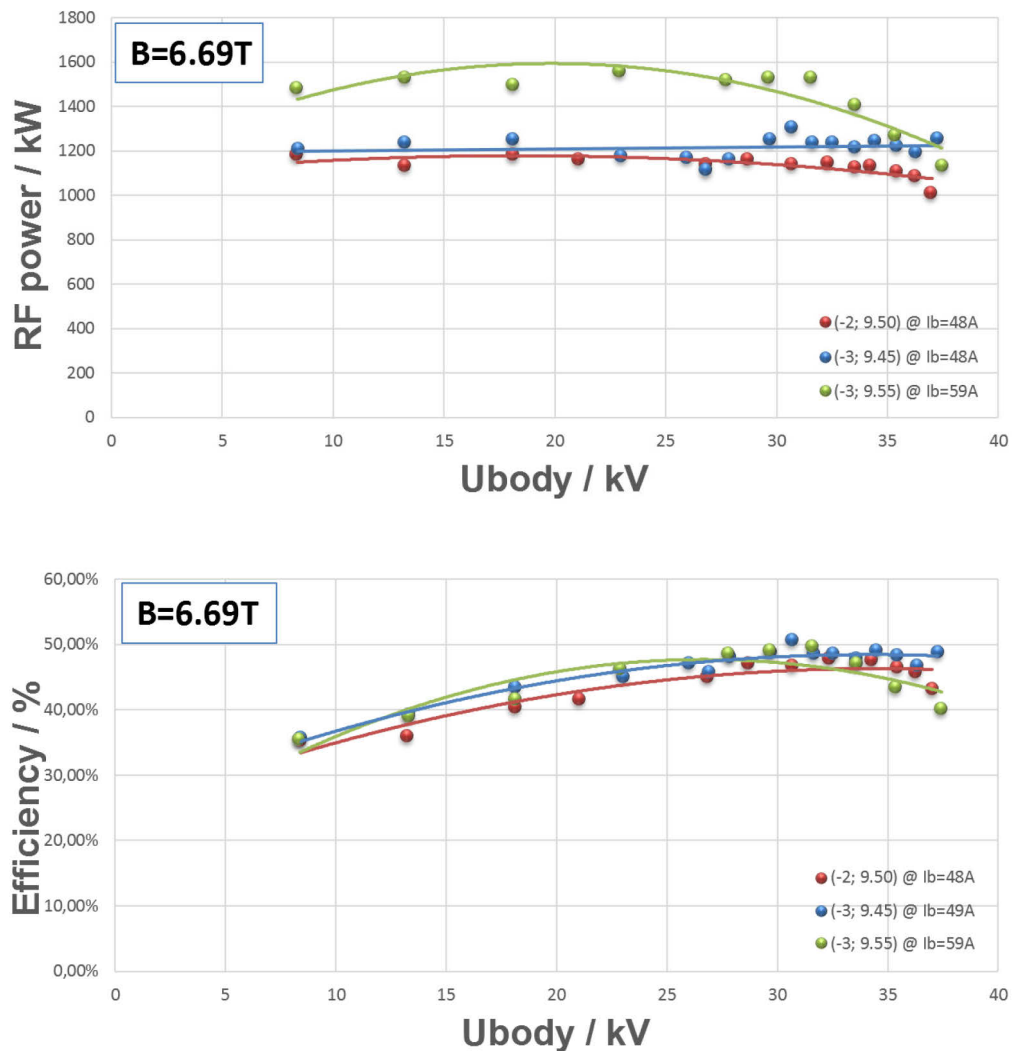
Fig. 1.1.3:   Achieved results in the depressed voltage operation with the improved gyrotron configuration.

1.2 Alternative scheme for radiative instability control

Contact: Chuanren Wu

In the EU-DEMO power plant, radiative instability will be controlled by the ECRH system. To compensate for the radiation, tens of megawatts will be deposited on the edge ($\rho \gtrsim 0.9$) of the confined plasma. Since the tokamak toroidal magnetic field decays with $B \propto 1/R$ while the ECRH frequency is approximately proportional to the magnetic field, dedicated low frequency gyrotrons are typically required to perform this task. In the current design, these dedicated gyrotrons will be idle most of the time. Therefore, it would not be optimal in view of system cost and gyrotron lifetime. To target this situation, alternative schemes have been explored. The basic idea is to combine this functionality with the beam lines of regular heating by using the same gyrotrons, transmission lines and single-disk torus windows. Two ideas have been conceptually explored, which are shown below. Idea 1 would be more resilient regarding plasma scenarios. However, it requires two gyrotron frequencies spaced by one octave and they should be rapidly switchable. This requires additional development of rapidly switchable harmonic gyrotrons which will be researched in a EUROfusion ENR-project starting from 2024. Furthermore, the slow-X mode of the wave requires an extremely large toroidal launching angle, and the principle relies on the broadband property of transmission lines at the considered frequency range.

Idea 2 requires only a single frequency of gyrotrons, while it relies on the harmonic absorption of the EC wave on the edge of the plasma. Compared to the first idea, this would only work with a tokamak where both resonances could be achieved by the same wave frequency. Besides, the polarizer should be fast enough to switch the wave polarizations in time.

As DEMO baseline may change in 2024, these possibilities will be further investigated considering the latest changes.
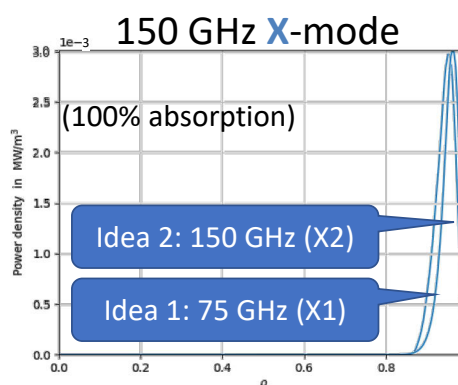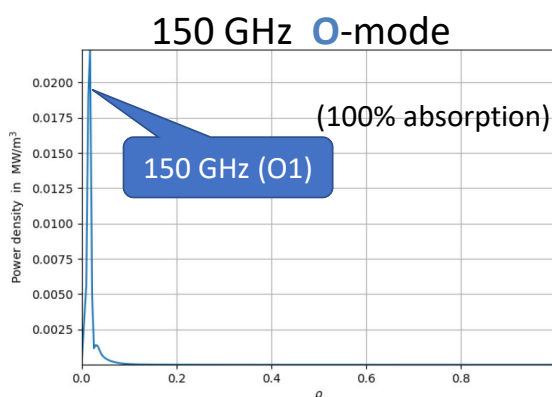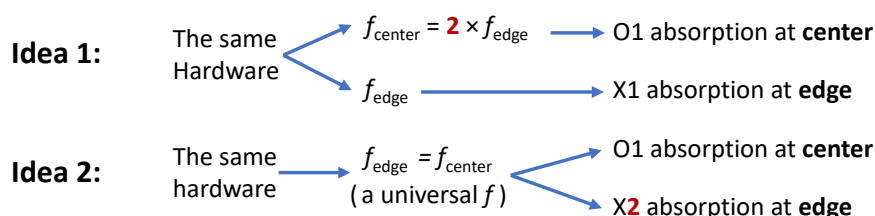
1.3 High-power fusion gyrotron cavities operating at the second harmonic of the electron cyclotron resonance frequency (EUROfusion ENR project)

Contact: Lukas Feuerstein, Dr.Stefan Illy

Operating gyrotrons at the second harmonic of the electron cyclotron frequency presents an appealing option due to the fact, that only halve of the magnetic field is required compared to those operating at the fundamental frequency. However, generating strong continuous wave radiation necessitates resonators capable of withstanding the Ohmic wall loading, requiring large overmoded cavities. In these cavities, certain competing fundamental modes couple more effectively with the electron beam than the intended second harmonic operating mode. Multiple methods and cavity designs were investigated to suppress the fundamental competitors and to ensure harmonic operation. The most promising technique for megawatt class harmonic gyrotrons is the use of impedance corrugated coaxial cavities. These cavities lower the quality factor of the fundamental competing modes, preventing them from oscillating.

Further improvements were made to the $TE_{34,19}$ harmonic cavity to enhance operating stability. It was also found that an axial variation of the depth of the coaxial insert corrugations can improve the suppression of the fundamental competing modes. Additionally, it was investigated whether the required beam parameters could be achieved with the currently available KIT-IHM coaxial electron guns. Therefore, the coaxial diode type gun and the triode type gun where simulated within different magnet systems. The triode type gun is preferable for the experimental investigation, because of the lower velocity spread of the particles and the extended adjustment options for the beam parameters. In a triode gun, the ratio of transversal to axial velocity α of the electrons can be set independently of their kinetic energy, as shown in Fig. 1.3.1. Additionally, we deployed the developed design strategy for fundamental $TE_{40,23}$ mode 204 GHz operation with an output power of 1.5 MW and an efficiency of > 20 % without depressed collector. Furthermore, a second harmonic 280 GHz gyrotron was designed for Collective Thompson Scattering Diagnostic applications. Despite the higher ohmic loading on the resonator walls due to the higher frequency, a theoretical output power of 0.7 MW could be achieved.

Within the framework of a leading EUROfusion Enabling Research project, research was conducted on the development of gyrotron cavity designs capable of rapidly switching between fundamental mode (s=1) operation at 85 GHz and second harmonic mode (s=2) operation at 170 GHz. By adjusting the parameters of the electron beam, primarily the velocity ratio α and the kinetic energy of the electrons, either the $TE_{17,10}$ or $TE_{34,19}$ mode can be excited. Such a gyrotron could be employed to reduce plasma instabilities, with plasma heating taking place in the second harmonic mode. Upon detection of a plasma instability, operation can be switched to fundamental mode within milliseconds to heat the plasma edge layers.
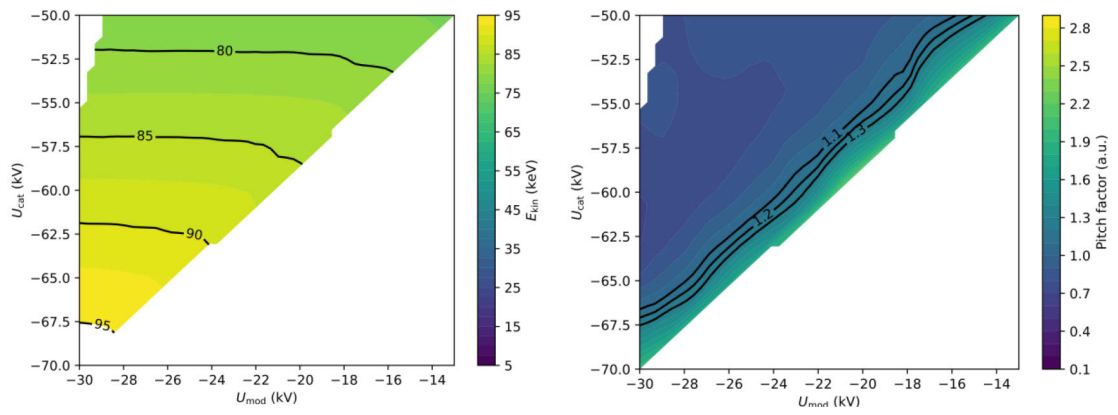
Fig. 1.3.1:   High Power Fusion Gyrotron Cavities Operating at the Second Harmonic of the Electron Cyclotron Frequency (EUROfusion ENR project). Operational maps of the triode electron gun in the 6.7 T Oxford Instruments magnet operating at 3.5 T. Left: electron beam energy at the cavity, right: obtained.

1.4 Frequency-stabilization of megawatt-class gyrotrons at Wendelstein 7-X

Contact: Laurent Krier

After the successful validation of the PLL system for a gyrotron operated at 174 GHz in 2022, the PLL system was used during the operation phase 2.1 in 2023 at the Wendelstein 7-X (W7-X) stellarator in Greifswald for the Collective Thomson Scattering (CTS) diagnostic. The CTS diagnostic requires consecutive short pulses from the gyrotron with a pulse length of 10 ms and a pulse repetition period of 140 ms. Furthermore, the notch filter of the CTS receiver is tuned to 173.92 GHz at which the gyrotron frequency shall also be tuned with the PLL system. The CTS scenario was tested for the 174 GHz gyrotron with the PLL system, and the result for 25 pulses are shown in Fig. 1.4.1.
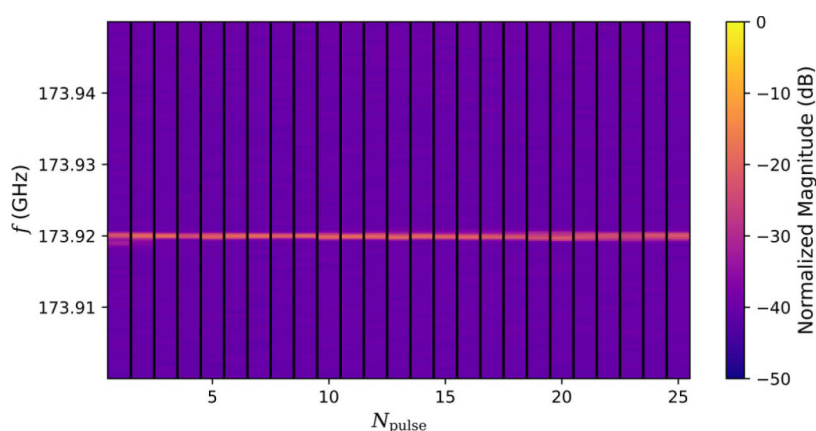
Fig. 1.4.1: Spectrum of a 174 GHz gyrotron for multiple pulses. The pulse repetition period is 140 ms and the pulse duration 10 ms. The spectrum of each pulse is taken between 3 ms and 6 ms, during which the CTS receiver is enabled. The center frequency of the notch filter is at 173.92 GHz.

In Fig. 1.4.1, the spectrum for each pulse is shown. The spectrum is calculated between 3 ms and 6 ms of a 10 ms gyrotron pulse, where the CTS receiver is also enabled. The gyrotron pulse is repeated every 140 ms. The spectrum in Fig. 1.4.1 shows that the gyrotron frequency is successfully stabilized for each pulse to 173.92 GHz, which is exactly the center of the CTS notch filter. After the successful tests, the gyrotron PLL was used for CTS measurements of the fast ion velocity distribution function at the W7-X stellarator during the last campaign.

Furthermore, a new concept was tested to improve the PLL system. The PLL system controls the gyrotron frequency with the body power supply, which is not able to counter the switching noise from the cathode power supply. For faster body voltage control, a fast amplifier is implemented in series to the existing body power supply. The maximum output voltage of the fast amplifier is 800 V peak-to-peak, which is sufficient to counter the remaining frequency noise.

First experiments show that it is possible to control the gyrotron frequency with the fast amplifier in series to the body power supply. The gyrotron frequency was successfully stabilized, and the frequency spectrum was improved compared to the frequency stabilization with the existing body power supply. However, the cathode power supply could not be countered fully, and sidebands at 3.3 kHz and 135 kHz are still present in the spectrum. The proof-of-principle experiments show that the concept with the fast amplifier is feasible but needs further investigations to remove the remaining noise.

1.5 Multistage depressed collectors for high-power megawatt-class gyrotrons

Contact: Benjamin Ell

Multistage Depressed Collector (MDC) technology is one of the key components for high power gyrotrons working at continuous waves to significantly increase the overall tube efficiency. A target gyrotron efficiency of ≥ 60 % is planned for the compact E×B MDC prototype for the first short-pulse experiments. The collector is optimized for the KIT 170-GHz, 2 MW coaxial-cavity short-pulse gyrotron. However, the basic design of the electrodes can be used in several gyrotron configurations, for example in multi-frequency operation and at different harmonics with the KIT 2 MW 170 GHz coaxial-cavity gyrotron. Other operation scenarios are the W7-X Upgrade SP gyrotron at 140 GHz operation in the designated 5.6 T Super Conducting (SC) magnet and 105 GHz operation of the same gyrotron in a 4.2 T SC magnet.

The compatibility of the MDC prototype with the updated configuration for second harmonic gyrotron operation at 170 GHz is presented. In the simulations, a high flexibility of voltage operation points was demonstrated as shown in Fig. 1.5.1 (a) with the possibility of achieving high collector efficiencies, whlie the reflected current is kept low. The optimal depression potentials are set to 45.9 kV and 62.8 kV for the first and second collector electrodes, respectively. A maximum collector efficiency of 85.3 % and a low reflected current of 30 mA were achieved without considering the space charge effect. The spent beam electrons are distributed as expected on the first electrode, as shown in Fig. 1.5.1 (b), while the maximum power loading density is in a very acceptable range for a short-pulse collector.

(a)

(b)
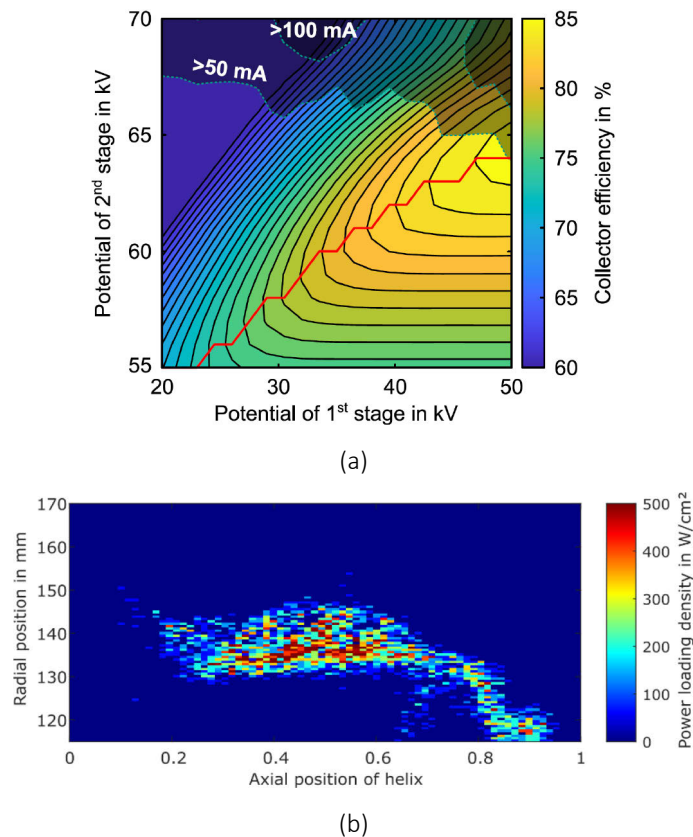
Fig. 1.5.1: Voltage operation points of the MDC short-pulse prototype for second harmonic operation with collector efficiency and reflected current (a) [Ref. Paper SOFT 24], and power loading density on the first electrode (b).

Fabrication of all parts of the first MDC prototype was finalized in 2023 and the MDC was assembled at KIT. The test assembly without vacuum housing is shown in Fig. 1.5.2 on the left. Due to the rapid availability of equipment the 140-GHz W7-X upgrade short-pulse gyrotron has been selected for first experiments. The configuration shown here is assembled with the shorter version of the bottom section which is compatible with the W7-X short-pulse gyrotron. A high collector efficiency of 75 % and a low reflected current were shown in the simulation for the W7-X gyrotron at 140 GHz, while at 105 GHz the collector efficiency dropped to 70 %. Experiments with the MDC prototype started end of 2024 with the W7-X gyrotron at 105 GHz in a 4.2 T magnet from CEA/WEST in the KIT FULGOR test-stand as shown in Fig. 1.5.2 on the right.
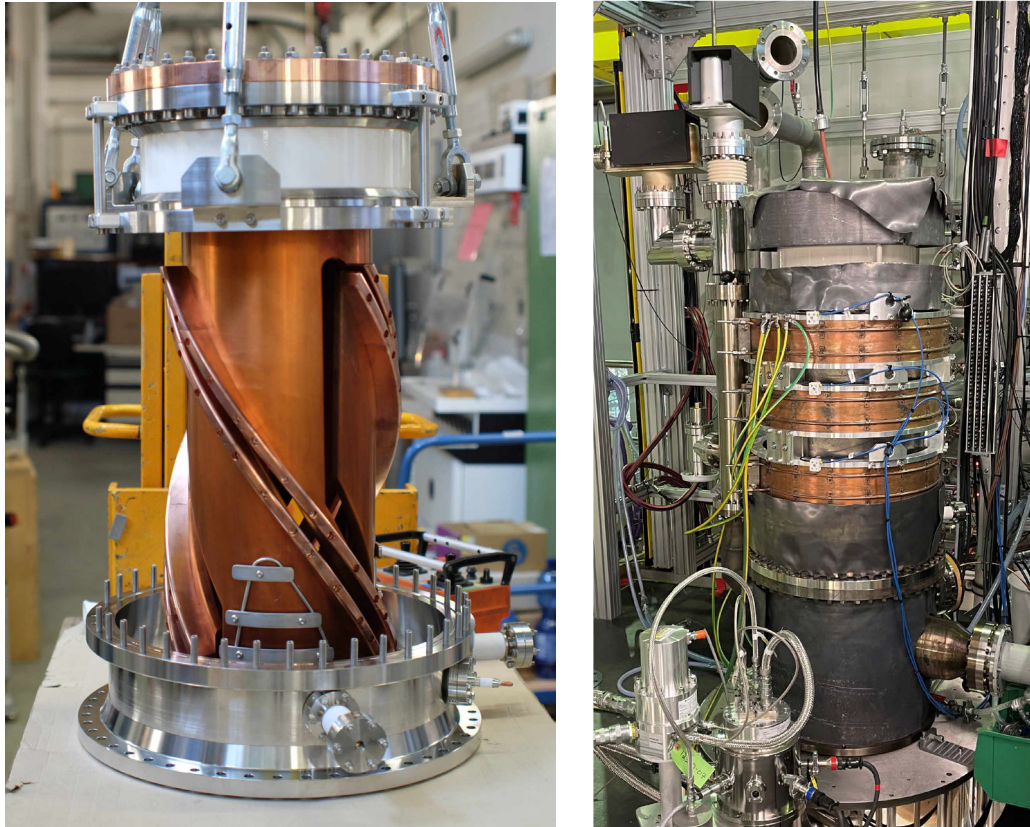
Fig. 1.5.2: Assembly demonstration of the MDC short-pulse prototype with both electrodes without vacuum housing (left) [Ref. Paper EC 24] and installed MDC on the W7-X gyrotron in the FULGOR test-stand (right).

1.6 Quasi-Optical (QO) mode converter, broadband window & Matching Optics Unit (MOU)

Contact: Dr. Jianbo Jin

1.6.1 Development of two-channel mirror-line launchers

A two-channel mirror-line launcher has been designed by weighting the wall perturbations to transform the co- & counter- rotating modes into Gaussian-like distributions. The field distributions operating in the co-rotating $TE_{34,19}$ mode and the counter-rotating $TE_{34,19}$-mode at 170 GHz are shown in Fig. 1.6.1.The Gaussian mode contents are estimated as 93.65 % at the launcher aperture.
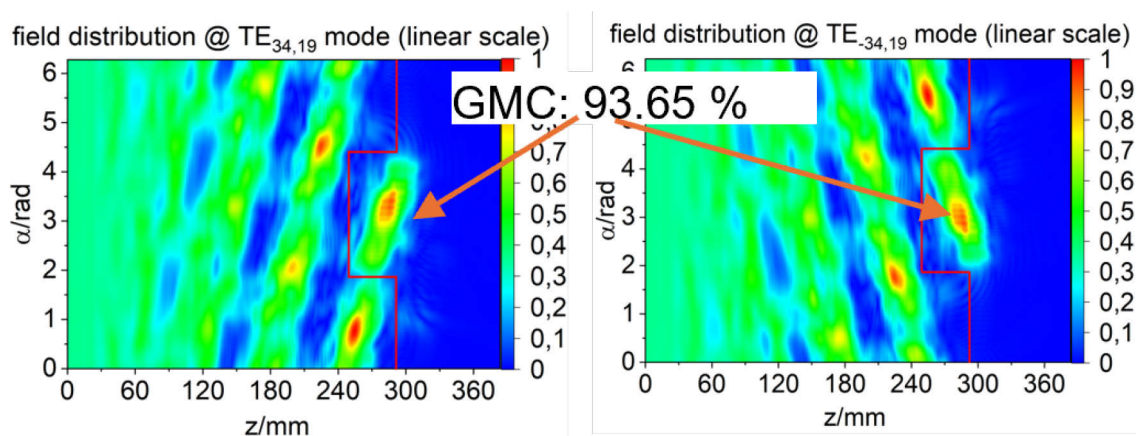
Fig. 1.6.1:   Field distribution on the launcher wall (linear scale)   @ $TE_{-34,19}$ (right), @$TE_{-34,19}$ (left).

1.6.2 Development of simulation tools for the simulation of EM resonances in broadband windows

HE_{11} mode transmission

The in-house computer code ASRET has been developed to calculate the transmission of the HE_{11} mode incident on a Brewster-angle window. As an example, a diamond disk with thickness of 1.8515 mm operating at136 GHz, 170 GHz, 204 GHz and 238 GHz is used in the window. Calculation results reveal that Brewster-angle windows can be employed for broadband transmission.

Implementation of dielectrics and interfaces between dielectrics and PEC into KARLESSS to identify unwanted EM resonances in Brewster-angle windows

In 2023 all the subroutines corresponding to the Electric Field Integral Equation (EFIE) have been developed and integrated into the in-house code KARLESSS.

In 2024, the KARLESSSS code has been improved to calculate both the electric and magnetic currents on the dielectric window disk. A new mesh generator has been developed to produce triangle meshes to match the surface of window disks very well. The triangle mesh on a window disk with radius of 44 mm is shown in Fig. 1.6.2 and the current distribution on the disk surface is shown in Fig. 1.6.3.
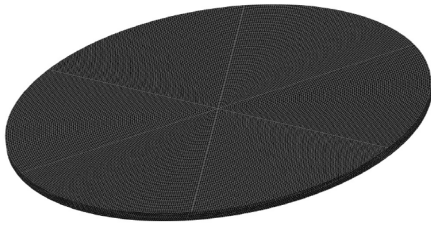
Fig. 1.6.2: Triangle meshes on the window disk.
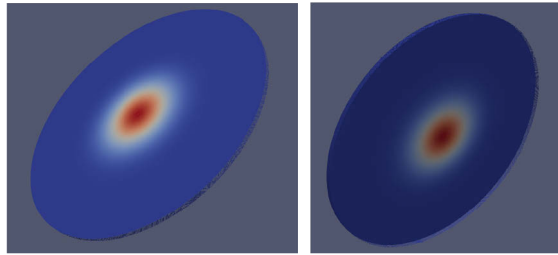
Fig. 1.6.3: Current distribution, front (left) & back view (right)

1.6.3 Broadband MOU for multi-frequency & frequency step-tunable gyrotrons

Abroadband MOU has been optimized for a multi-frequency gyrotron operating at four center frequencies 136 GHz ($TE_{28,13}$-mode) / 170 GHz ($TE_{35,16}$-mode) / 204 GHz ($TE_{42,19}$-mode) and 238 GHz ($TE_{49,22}$-mode) including broadband operation (+/-10 GHz). The field distributions at the entry of the HE_{11} waveguide are shown in Fig. 1.6.2, where the HE_{11}-mode contents (HMC) are estimated to 94.43 % at 136.29 GHz, 97.56 % at 170 GHz, 98.1 % at 203.71 GHz, and 95.89 % at 237.41 GHz, respectively. For the broadband (+/-10 GHz) operation with frequency steps of 2 GHz at the four different operating frequencies, all the forty HMCs are estimated as larger than 91 % and smaller than 98.1 %.

(a)

(b)

(c)

(d)
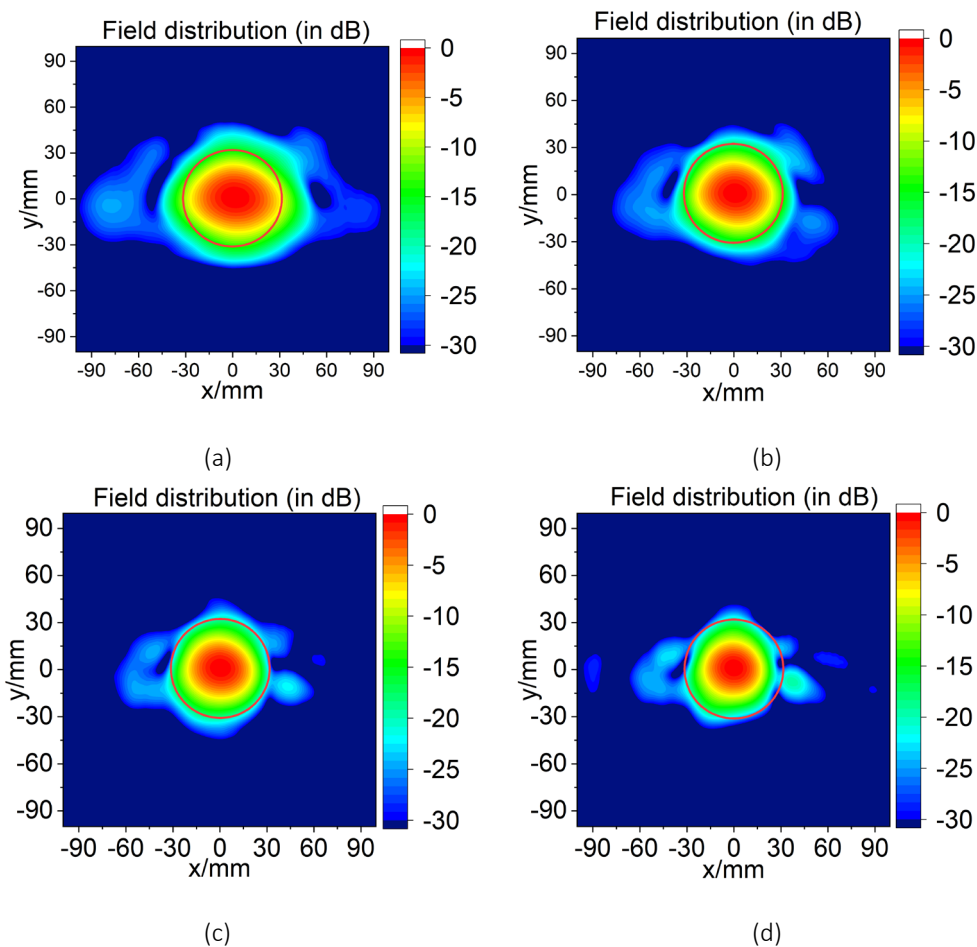
Fig. 1.6.4: Field distributions at entrance of HE_{11} waveguide, (a) @ 136.29 / (b) 170 / (c) 203.74/ (d) @ 237.48 GHz. The red circles denote the edge of the HE_{11} waveguide.

1.6.4 Investigation of constraints for direct feed to transmission line.

A QO system has been designed to transform the $TE_{24,8}$-mode at 117.5 GHz to match the HE_{11} waveguide located at the output window of the gyrotron. The HMC of the field distribution in the window plane is estimated as 98 %, so it can be directly fed into the HE_{11} transmission waveguide without MOU.

1.6.5 Development of launcher for a dual-harmonic gyrotron.

A mirror-line launcher has been synthesized for a highly efficient, megawatt-class fusion gyrotron that will operate at the fundamental and second harmonic of the electron cyclotron frequency. It is really a challenge to design a launcher to operate at such broadband frequencies, the $TE_{17,10}$ mode @ 85.66 GHz and the $TE_{34,19}$ mode @ 170.05 GHz. Fig. 1.6.5 shows the field distributions on the mirror-line launcher wall. The Gaussian Mode Contents (GMC) of the field on the launcher aperture are estimated as 97.05 % @ the $TE_{17,10}$ mode, 85.66 GHz, and 97.3 % @ the $TE_{34,19}$ mode, 170.05 GHz. In the graphs, the cuts are indicated with red lines. As shown in Fig. (left), the field on the straight cut (marked out with the elliptic dashed black line) is relatively strong. Therefore, the reflection on the straight cut is also relatively large and results in the "ripple" on the field distribution on the launcher wall. The launcher would be further optimized.
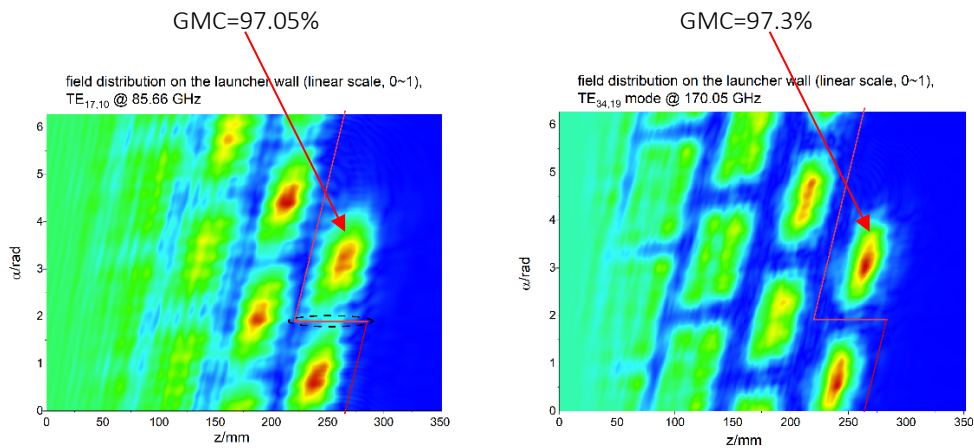
Fig. 1.6.5: Field distributions on launcher wall, operating in the $TE_{17,10}$ mode @ 85.66 GHz (left) and in the $TE_{34,19}$ mode @ 170.05 GHz (right).

1.7 Operation of FULGOR with a high power industrial gyrotron

Contact: Dr. Gerd Gantenbein

During the recent years the new high-power gyrotron teststand FULGOR has been built up. This unique facility will replace and complement the old teststand with a performance which is well beyond the state of art of gyrotron development. First operation of the teststand with a gyrotron has been show in 2022.

In 2023 on the FULGOR gyrotron teststand for megawatt-class gyrotrons a high-power industrial gyrotron has been installed and tested. These tests have been performed with a 1 MW, 105 GHz gyrotron within a collaboration of CEA IRFM, Cadarache, France, Thales, France and KIT. The design of the gyrotron was done under guidance of KIT in the previous years, the tube has been manufactured by Thales and it will be the first out of three gyrotrons which will be used for ECRH and CD at the WEST tokamak.

The tube and the corresponding magnet have been delivered to KIT in 2023, the operation of the cryogen-free superconducting (SC) magnet has been started and its performance according to the specifications has been shown. The gyrotron has been inserted into the magnet and equipped with the beam sweeping systems Fig. 1.7.1. All components have been connected to the cooling system. Prior to pulsing of the tube at nominal parameters the HV stability has been verified and the emitter has been conditioned up to nominal temperature.

Fig. 1.7.1:   TH1511 installed in the super conducting magnet (left), bottom part of the gyrotron with support structure, HV isolation oil tank and magnet (right).

In the first phase of operation short pulses up to 3 ms have been applied to the CEA-WEST Gyrotron. The gyrotron has been tested in non-depressed and depressed configuration where a part of the electron rest energy after interaction is recovered and the efficiency is increased. After conditioning the gyrotron showed a smooth and stable operation, nominal mode (TE$_{20,8}$) was oscillating close to 105 GHz. In non-depressed operation the peak output power was 1.2 MW with an efficiency of 30 % at a beam current close to 50 A. At reduced beam current (40 A) an efficiency of 35 % has been achieved. Depressed operation of the gyrotron with energy recovery showed an efficiency of close to 46 % with an output power of ~1 MW), at a depression voltage of 25-26 kV. See Fig. 1.7.2 and Fig. 1.7.3 for typical operating signals.

The RF output beam has been measured and analysed, the Gaussian has been calculated to 96.6 % and the beam propagating parameters are very close to the design values Fig. 1.7.4.

These first results are excellent starting points for long pulse operation of the gyrotron which is scheduled for the first half of 2024.
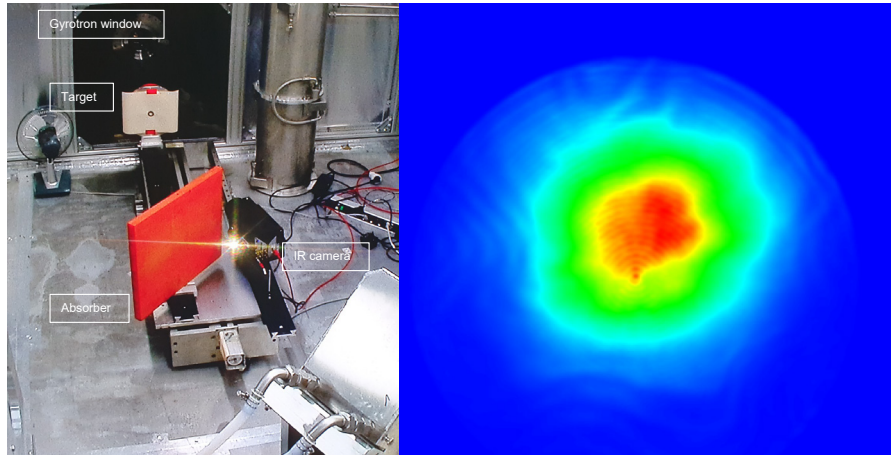
Fig. 1.7.2 : Experimental set up for monitoring the RF beam profile (left) and typical cross section of the beam measured by IR camera (right).
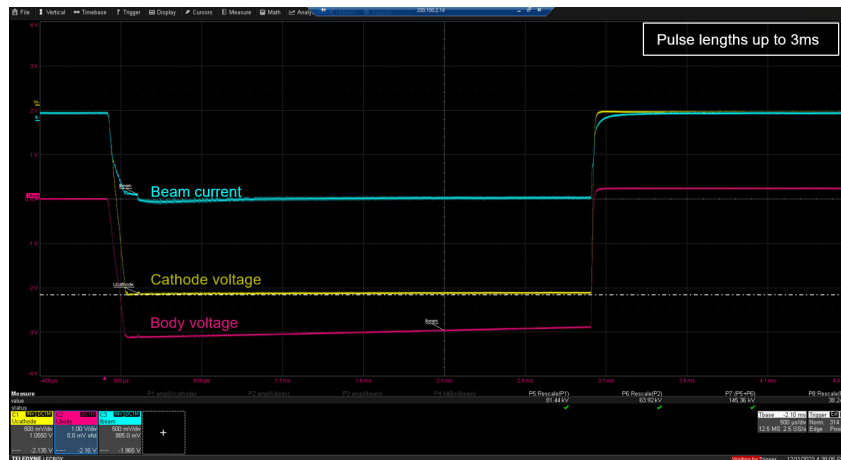
Fig. 1.7.3: Typical voltage and beam current signals during short pulse operation of TH1511 in depressed modus
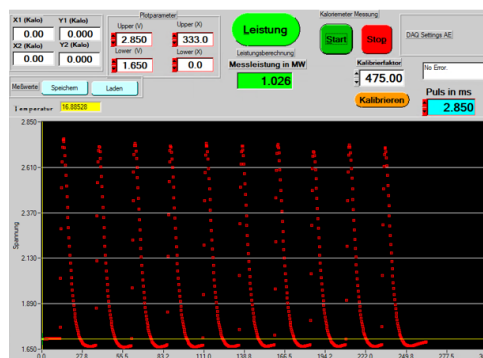
Fig. 1.7.4: Short pulse power measurement of TH1511

1.8 Exciting a world-record cavity-mode in cold tests operating at 238 GHz

Contact: Dr. Tomasz Rzesnicki

In 2022, the first 2 MW 170/204 GHz coaxial-cavity short-pulse pre-prototype has been presented for future fusion machines like DEMO. However, recent start-ups, like Proxima Fusion, request gyrotron operating in the frequency range from 238 GHz to 250 GHz for their fusion machines that work with higher magnetic fields. Therefore, the existing mode series has been extended to be capable operating the existing gyrotron at 238 GHz. The selected mode is given by the $TE_{46,27}$ ($\chi=147.5$). In this year, the given mode has been excited in cold tests in the quasi-optical mode generator according to Fig. 1.8.1. The cavity was designed for special use in the mode generator. The cavity is perforated with 4000 holes. A challenge is the very dense mode spectrum as depicted in Fig. 1.8.1. It can be calculated that approximately 5600 modes are capable of propagation at 238 GHz. The operating frequency has been determined to be 238.133 GHz. The measured quality factor is with 4500 in very good agreement with the simulated 4423. In Fig. 1.8.2 the measured field intensity and phase pattern of the vertical polarization of the $TE_{46,27}$ mode is depicted. This mode will replace the $TE_{40,23}$ mode at 204 GHz as the highest ever excited mode in cold measurement.
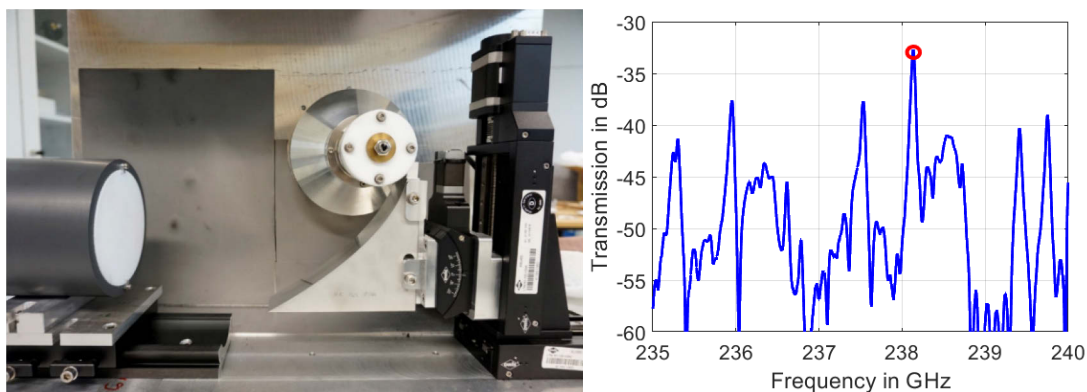
Fig. 1.8.1: Photo of the assembly and arrangement of the mode generator and measured frequency spectrum
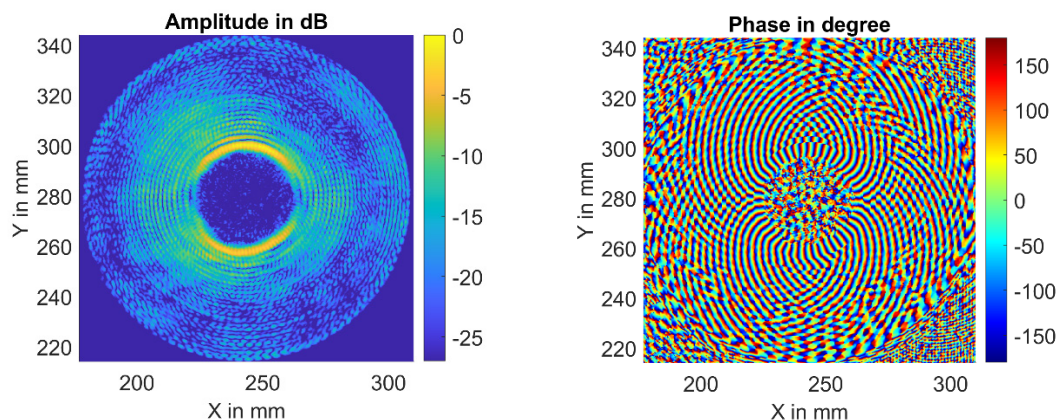
Fig. 1.8.2: Excited mode pattern of $TE_{46,27}$ mode at 238.133 GHz: amplitude (left) and phase (right)

1.9 Development of a gyro-amplifier for the SFB project HyPERiON

Contact: Max Vöhringer

In recent years, dynamic nuclear polarization (DNP) magic angle spinning NMR has gained increasing interest. To achieve the millimeter (mm)-waves with the desired power and frequency, high power oscillators (gyrotrons) are currently employed. Those devices use the relativistic electron cyclotron maser (ECM) interaction but are not capable of producing coherent pulse sequences. However, to create such coherent pulse sequences, amplifiers instead of oscillators are needed. One promising amplifier is the gyro-TWT with helically corrugated interaction region, the so-called helical gyro-TWT. The development of such an amplifier is the goal of the SFB 1527 HyPERiON Project B01. An output power of 1 kW at a frequency of 263 GHz is desired.

A system overview is given in Fig. 1.9.1 here the three parts of the entire system can be seen. First the solid-state pre-amplifier system Fig. 1.9.1 (left) it generates a lower power input signal Fig. 1.9.1 (green arrows) which is radiated by an antenna array into the second part, the quasi-optical feed system. The solid-state pre-amplifier is designed at IHE.
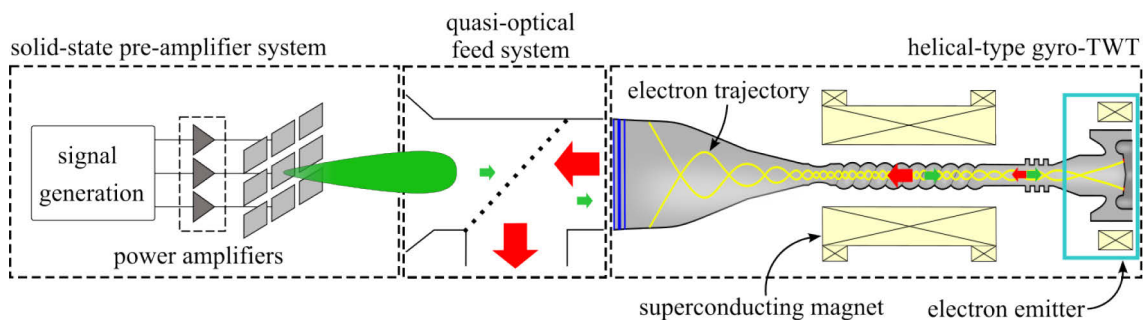
Fig. 1.9.1:   Schematic of amplifier system. The signal power flow after the solid-state pre-amplifier is depicted in green, the power flow during and after amplification in the gyro-TWT is red.

The input signal enters the power splitter Fig. 1.9.1 (center), it is used to separate the input from the output signal Fig. 1.9.1 (red arrows). The input signal is then fed into the combined input/output section of a high-power helical gyro-TWT Fig. 1.9.1 (right side). This feeding system enables a direct transition from the pre-amplifier array and is one of the unique aspects of this amplifier. Assuming an input power level of several hundred milliwatt up to 1 W, which is the goal of the preamplifier system, and a gyro-amplifier gain of above 20 dB, a new level of output power up to 1 kW in pulsed operation regime is expected over a wide bandwidth.

To operate a 263 GHz helical-type gyro-TWT a high magnetic flux density of 5.1 T is required. To create such high fields, superconducting magnets are utilized. Due to the long delivery times of such a magnet and the dependence of other components on the magnetic field profile, it was designed first. The requirements of the field in the emitter and collector regions were investigated. The magnet was designed in a way to produce a constant field at the interaction region to facilitate efficient energy transfer from electron beam to electromagnetic wave. Parallel to the magnet design, a suitable electron emitter was designed and published. The resulting Magnet geometry is shown in Fig. 1.9.2.
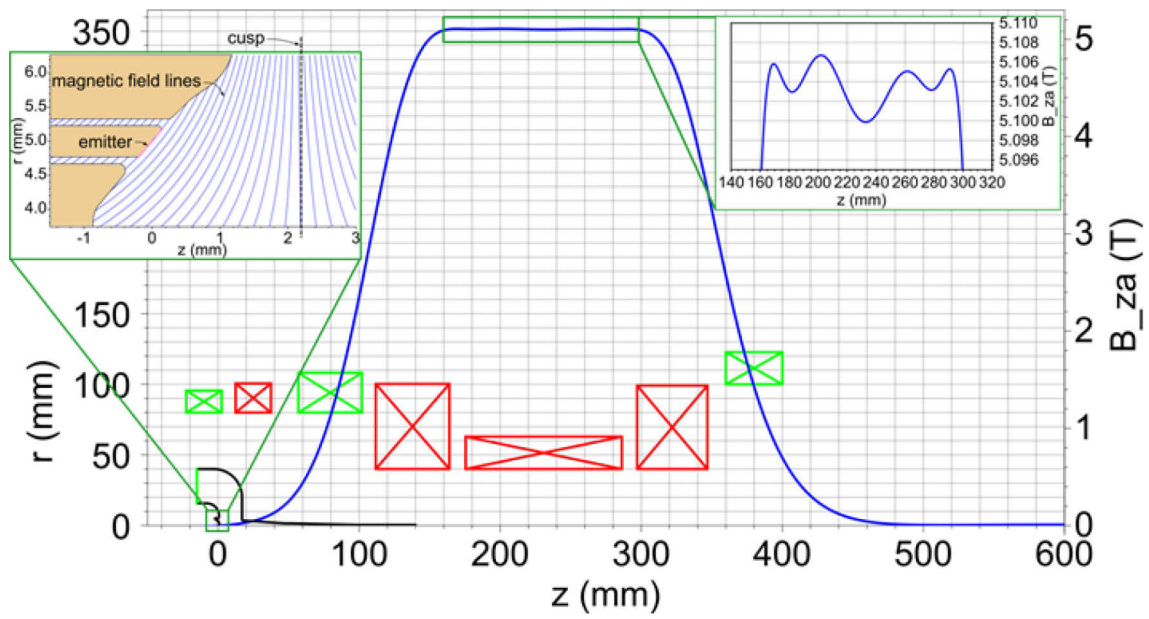
Fig. 1.9.2: Magnet coil configuration, red solenoids show positive winding direction, green solenoids negative winding direction.

The designed electron emitter is able to operate at multiple frequencies, e.g. 94 GHz, 140 GHz in addition to the desired 263 GHz with a current of up to 1 A and voltages up to 65 kV. Additionally, investigations into the design and manufacturing of the microwave components like the interaction region and polarizers were conducted.

1.10 Initial design studies on high frequency gyrotrons

Contact: André Schmidt

In recent years, interest in high-frequency gyrotrons for Electron Cyclotron Resonance Heating (ECRH) applications in compact fusion reactors has grown significantly. This includes Proxima Alpha, a high-field quasi-isodynamic stellarator. To address this need, plans are underway to develop a prototype gyrotron operating at approximately 240 GHz with an output power exceeding 1 MW. The prototype shall be tested at the FULGOR facility, which will be equipped with a newly commissioned 10.5 Tesla magnet system.

Various design options are being evaluated to optimize thermal management, minimize mode competition, and enhance operational stability. To manage the significant thermal loading, a high mode order must be employed. However, to suppress mode competition at such high mode orders, a coaxial cavity design with an inner insert is being considered. Advanced simulations have been performed to evaluate the electron beam interaction within this configuration. For the Magnetron Injection Gun (MIG), a triode design has been proposed for better electron beam control in the prototype. This triode has been simulated to assess whether the required precision can be achieved to meet operational demands.

Journal Publications

Gantenbein, G.; Avramidis, K.; Ell, B.; Delpech, L.; Feuerstein, L.; Illy, S.; Jelonnek, J.; Jin, J.; Krier, L.; Laqua, H. P.; Ruess, T.; Rzesnicki, T.; Stanculovic, S.; Thumm, M. (2023). Progress in High Power Gyrotron Development Projects at KIT. 2023 48th International Conference on Infrared, Millimeter, and Terahertz Waves (IRMMW-THz, Montreal, QC, Canada, 17-22 September 2023, Institute of Electrical and Electronics Engineers (IEEE). doi:10.1109/IRMMW-THz57677.2023.10299306

Stanculovic, S.; Avramidis, K.; Difonzo, R.; Gajetti, E.; Gantenbein, G.; Illy, S.; Jelonnek, J.; Leggieri, A.; Ruess, T.; Rzesnicki, T.; Savoldi, L. (2023). Advanced Experimental Investigations on Cooling Concepts of Cavities for Megawatt-Class CW Gyrotrons. 2023 48th International Conference on Infrared, Millimeter, and Terahertz Waves (IRMMW-THz), Montreal, QC, Canada, 17-22 September 2023, Institute of Electrical and Electronics Engineers (IEEE). doi:10.1109/IRMMW-THz57677.2023.10299069

D'Isa, F. A.; Pasch, E.; Beurskens, M. N. A.; Brunner, K. J.; Fuchert, G.; Pasqualotto, R.; Giudicotti, L.; W7-X Team. (2023). Analysis of dual laser Thomson scattering signals on W7-X. Journal of Instrumentation, 18 (11), Art.-Nr.: C11025. doi:10.1088/1748-0221/18/11/C11025

Rzesnicki, T.; Avramidis, K. A.; Chelis, I.; Gantenbein, G.; Feuerstein, L.; Illy, S.; Jelonnek, J.; Jin, J.; Leggieri, A.; Legrand, F.; Lievin, C.; Marek, A.; Ruess, T.; Stanculovic, S.; Thumm, M. (2023). Parasitic-modes free, high-performance operation of the European 1 MW, 170 GHz Short-Pulse Prototype Gyrotron for ITER. 2023 48th International Conference on Infrared, Millimeter, and Terahertz Waves (IRMMW-THz), 2 S., Institute of Electrical and Electronics Engineers (IEEE). doi:10.1109/IRMMW-THz57677.2023.10299287

Maksimenko, A.; Shcherbinin, V.; Thumm, M.; Jelonnek, J. (2023). Nonlinear Theory of Beam-Wave Interaction in Gyrotron Cavities with Gradual and Abrupt Transitions. 2023 48th International Conference on Infrared, Millimeter, and Terahertz Waves (IRMMW-THz), 1–2, Institute of Electrical and Electronics Engineers (IEEE). doi:10.1109/IRMMW-THz57677.2023.10299300

Illy, S.; Avramidis, K. A.; Chelis, I.; Ell, B.; Feuerstein, L.; Gantenbein, G.; Ioannidis, Z.; Jelonnek, J.; Jin, J.; Latsas, G.; Marek, A.; Peponis, D.; Rzesnicki, T.; Thumm, M.; Tigelis, I.; Wu, C. (2023). Progress in the Design of Megawatt-Class Fusion Gyrotrons Operating at the Second Harmonic of the Cyclotron Frequency. 2023 48th International Conference on Infrared, Millimeter, and Terahertz Waves (IRMMW-THz), 1–2, Institute of Electrical and Electronics Engineers (IEEE). doi:10.1109/IRMMW-THz57677.2023.10299170

Vöhringer, M.; Marek, A.; Illy, S.; Gantenbein, G.; Thumm, M.; Wu, C.; Jelonnek, J. (2023). Universal CUSP-Type Electron Gun for Helical Gyro-TWTs for DNP-NMR Applications. 2023 48th International Conference on Infrared, Millimeter, and Terahertz Waves (IRMMW-THz), 2 S., Institute of Electrical and Electronics Engineers (IEEE). doi:10.1109/IRMMW-THz57677.2023.10299143

Shcherbinin, V. I.; Tkachova, T. I.; Andrieieva, O. L.; Thumm, M.; Jelonnek, J. (2023). Full-Wave Analysis of a Complex Gyrotron Cavity with Coupled Smooth-Walled and Corrugated Resonators. 2023 48th International Conference on Infrared, Millimeter, and Terahertz Waves (IRMMW-THz), Montreal, QC, 17th-22nd September 2023, 1–2, Institute of Electrical and Electronics Engineers (IEEE). doi:10.1109/IRMMW-THz57677.2023.10299166

Ruess, T.; Gantenbein, G.; Illy, S.; Jin, J.; Rzesnicki, T.; Stanculovic, S.; Thumm, M.; Jelonnek, J. (2023). Study of 136/170 GHz Dual-Frequency Operation Based on the KIT 2 MW 170 GHz Coaxial-Cavity Pre-Prototype Gyrotron. 2023 48th International Conference on Infrared, Millimeter, and Terahertz Waves (IRMMW-THz), 1–2, Institute of Electrical and Electronics Engineers (IEEE). doi:10.1109/IRMMW-THz57677.2023.10298931

Peponis, D. V.; Avramidis, K. A.; Chelis, I. G.; Ioannidis, Z. C.; Illy, S.; Jelonnek, J.; Latsas, G. P.; Tigelis, I. G. (2023). Design of MW-Class Coaxial Gyrotron Cavities With Mode-Converting Corrugation Operating at the

Second Cyclotron Harmonic. IEEE Transactions on Electron Devices, 70 (12), 6587–6593. doi:10.1109/TED.2023.3326431

W7-X Team; Bannmann, S.; Ford, O.; Hoefel, U.; Poloskei, P.; Pavone, A.; Kwak, S.; Svensson, J.; Lazerson, S.; McNeely, P.; Rust, N.; Hartmann, D.; Pasch, E.; Fuchert, G.; Wolf, R. C. (2023). Fast forward modeling of neutral beam injection and halo formation including full Balmer-α emission prediction at W7-X. Journal of Instrumentation, 18 (10), Article no: P10029. doi:10.1088/1748-0221/18/10/P10029

Krychowiak, M.; König, R.; Barbui, T.; Brezinsek, S.; Brunner, J.; Effenberg, F.; Endler, M.; Feng, Y.; Flom, E.; Gao, Y.; Gradic, D.; Hacker, P.; Harris, J. H.; Hirsch, M.; Höfel, U.; Jakubowski, M.; Kornejew, P.; Otte, M.; Pandey, A.; Pedersen, T. S.; Puig, A.; Reimold, F.; Schmitz, O.; Schröder, T.; Winters, V.; Zhang, D.; W7-X Team. (2023). First feedback-controlled divertor detachment in W7-X: Experience from TDU operation and prospects for operation with actively cooled divertor. Nuclear Materials and Energy, 34, Art.-Nr.: 101363. doi:10.1016/j.nme.2023.101363

Girka, I. O.; Thumm, M. (2023). Propagation of short-wavelength electromagnetic surface waves along the transition layer between two plasma-like half-spaces in the Voigt geometry. Physics of Plasmas, 30 (9), Article no: 092101. doi:10.1063/5.0165416

Wu, C.; David, P.; Fable, E.; Frattolillo, D.; Di Grazia, L. E.; Mattei, M.; Siccinio, M.; Treutterer, W.; Zohm, H. (2023). Architecture Design and Internal Implementation of a Universal Coupling Between Controllers and Physics in a Tokamak Flight Simulator. Fusion Science and Technology, 1–6. doi:10.1080/15361055.2023.2234741

Girka, I. O.; Thumm, M. (2023). Do The Dispersion Properties of Electromagnetic Surface Waves at the Sharp Boundary Plasma-Metal in Slab Voigt Geometry Represent the Limiting Case of those for the Interface of two Plasmas?. Voprosy atomnoj nauki i techniki, 146 (4), 12–15. doi:10.46813/2023-146-012

Zhang, D.; Buttenschön, B.; Jablonski, S.; Kubkowska, M.; Ford, O.; Alcusón, J. A.; Beidler, C. D.; Burhenn, R.; Beurskens, M. N. A.; Langenberg, A.; Pablant, N.; Reimold, F.; Rahbarnia, K.; Smith, H. M.; Wegner, T.; Wurden, G.; Bozhenkov, S. A.; Feng, Y.; Brunner, K. J.; Fuchert, G.; Gao, Y.; Geiger, J.; Giannone, L.; Höfel, U.; Hirsch, M.; Huang, Z.; Knauer, J.; Kremeyer, T.; Krychowiak, M.; Kwak, S.; Laqua, H. P.; Laube, R.; Neuner, U.; Pasch, E.; Pavone, A.; von Stechow, A.; Svensson, J.; Thomsen, H.; W7-X Team. (2023). Observation of impurity accumulation and its compatibility with high plasma performance in W7-X. Plasma Physics and Controlled Fusion, 65 (10), Art.-Nr. 105006. doi:10.1088/1361-6587/acf0e7

W7-X Team; Alcusón, J. A.; Wegner, T.; Dinklage, A.; Langenberg, A.; Bähner, J.-P.; Buttenschön, B.; Edlund, E. M.; Fuchert, G.; García-Regaña, J. M.; Grulke, O.; Huang, Z.; Porkolab, M.; Stechow, A. V.; Xanthopoulos, P.; Zocco, A. (2023). Quantitative comparison of impurity transport in turbulence reduced and enhanced scenarios at Wendelstein 7-X. Nuclear Fusion, 63 (9), Article no: 094002. doi:10.1088/1741-4326/aceb76

Lazerson, S. A.; Kulla, D. A.; Hartmann, D. A.; McNeely, P.; Rust, N.; W7-X Team. (2023). Gyro orbit simulations of neutral beam injection in Wendelstein 7-X. Nuclear Fusion, 63 (9), Art.-Nr. 096012. doi:10.1088/1741-4326/ace9ec

W7-X Team; Vaz Mendes, S.; Rahbarnia, K.; Slaby, C.; Thomsen, H.; Schilling, J.; Borchardt, M.; Kleiber, R.; Könies, A.; Bähner, J.-P.; von Stechow, A.; Sunn Pedersen, T.; Klinger, T. (2023). Broadband Alfvénic excitation correlated to turbulence level in the Wendelstein 7-X stellarator plasmas. Nuclear Fusion, 63 (9), Art.-Nr.: 096008. doi:10.1088/1741-4326/ace53c

Shcherbinin, V. I.; Thumm, M.; Jelonnek, J. (2023). High-Q Cavity With Distributed Bragg Reflector for Second-Harmonic Gyrotrons Driven by Low-Power Electron Beams. 24th International Vacuum Electronics Conference (IVEC), 1–2, Institute of Electrical and Electronics Engineers (IEEE). doi:10.1109/IVEC56627.2023.10157117

Miyazaki, A.; Lofnes, T.; Caspers, F.; Spagnolo, P.; Jelonnek, J.; Ruess, T.; Steinmann, J. L.; Thumm, M. (2023). Millimeter-Wave WISP Search with Coherent Light-Shining-Through-a-Wall Toward the STAX Project. Annalen der Physik, 536 (1), Art.Nr.: 2200619. doi:10.1002/andp.202200619

W7-X Team; Bosch, H.-S.; Eeten, P. van; Grulke, O.; Bräuer, T.; Degenkolbe, S.; Nagel, M.; Rummel, T.; Schacht, J.; Spring, A.; Winter, A. (2023). Preparing the operation of Wendelstein 7-X in the steady-state regime. Fusion Engineering and Design, 193, Art.-Nr.: 113830. doi:10.1016/j.fusengdes.2023.113830

Leggieri, A.; Albajar, F.; Alberti, S.; Avramidis, K. A.; Bariou, D.; Bin, W.; Bruschi, A.; Chelis, I.; Difonzo, R.; Ell, B.; Fanale, F.; Feuerstein, L.; Gajetti, E.; Gantenbein, G.; Genoud, J.; Goodman, T. P.; Hogge, J.-P.; Illy, S.; Ioannidis, Z.; Jelonnek, J.; Jin, J.; Kohler, S.; Latsas, G.; Laqua, H.; Legrand, F.; Lievin, C.; Marchesin, R.; Marek, A.; Marsen, S.; Noke, F.; Peponis, D.; Ponomarenko, S.; Ruess, T.; Rzesnicki, T.; Sanchez, F.; Savoldi, L.; Stanculovic, S.; Stange, T.; Tigelis, I.; Torreblanca, H.; Vallée, E.; Wolf, R.; Zelkas, A.; Thumm, M. (2023). Progress of European Industrial Gyrotron Developments for Nuclear Fusion. 24th International Vacuum Electronics Conference (IVEC), Chengdu, China, 25-28 April 2023, 1–2, Institute of Electrical and Electronics Engineers (IEEE). doi:10.1109/IVEC56627.2023.10157606

Jin, J.; Gantenbein, G.; Illy, S.; Jelonnek, J.; Thumm, M. (2023). Improved Synthesis of Quasi-Optical Launchers Used in Injection Locked Gyrotrons. 24th International Vacuum Electronics Conference (IVEC), Chengdu, China, 25-28 April 2023, 1–2, Institute of Electrical and Electronics Engineers (IEEE). doi:10.1109/IVEC56627.2023.10157968

Feuerstein, L.; Marek, A.; Wu, C.; Illy, S.; Thumm, M.; Jelonnek, J. (2023). Design of a Second Harmonic MW-Level Coaxial Gyrotron Cavity. 2023 24th International Vacuum Electronics Conference (IVEC), Chengdu, China, 25-28 April 2023, 1–2, Institute of Electrical and Electronics Engineers (IEEE). doi:10.1109/IVEC56627.2023.10156958

Jelonnek, J.; Gantenbein, G.; Illy, S.; Rzesnicki, T.; Ell, B.; Feuerstein, L.; Jin, J.; Krier, L.; Marek, A.; Ruess, T.; Stanculovic, S.; Thumm, M.; Vöhringer, M.; Wu, C. (2023). Advanced Developments for Gyrotrons Considering Designs, Tools and Test Facilities at KIT. 24th International Vacuum Electronics Conference (IVEC), 1–2, Institute of Electrical and Electronics Engineers (IEEE). doi:10.1109/IVEC56627.2023.10157915

W7-X Team; Krier, L.; Avramidis, K. A.; Braune, H.; Gantenbein, G.; Illy, S.; Jelonnek, J.; Laqua, H. P.; Marsen, S.; Moseev, D.; Noke, F.; Ruess, T.; Stange, T.; Thumm, M.; Wolf, R. C. (2023). Short-pulse frequency stabilization of a MW-class ECRH gyrotron at W7-X for CTS diagnostic. Fusion Engineering and Design, 192, Art.-Nr.: 113828. doi: 10.1016/j.fusengdes.2023.113828

Romba, T.; Reimold, F.; Jaspers, R. J. E.; Edmondson, A. J.; Ford, O. P.; Geiger, B.; Jabłoński, S.; Kubkowska, M.; Neelis, T. W. C.; Poloskei, P. Z.; Vanó, L.; Klinger, T.; W7-X Team. (2023). Evaluation and validation of radial impurity density profiles from CXRS using neutral beam modelling in W7-X. Plasma Physics and Controlled Fusion, 65 (7), Artkl.Nr.: 075011. doi:10.1088/1361-6587/acd5c8

Romba, T.; Reimold, F.; Jaspers, R. J. E.; Ford, O. P.; Vanó, L.; Klinger, T.; W7-X Team. (2023). Suppression of anomalous impurity transport in NBI-heated W7-X plasmas. Nuclear Fusion, 63 (7), Artkl.Nr.: 076023. doi:10.1088/1741-4326/acd5e1

Jagielski, B.; Wenzel, U.; Sunn Pedersen, T.; Melzer, A.; Pandey, A.; Mackel, F.; W7-X Team. (2023). D-Mag — a laboratory for studying plasma physics and diagnostics in strong magnetic fields. Journal of Instrumentation, 18 (06), Artkl.Nr.: P06006. doi:10.1088/1748-0221/18/06/P06006

Fortuna-Zalesna, E.; Zielinski, W.; Ciupiński, Ł.; Spychalski, M.; Dhard, C. P.; Naujoks, D.; Rasinski, M.; Brezinsek, S.; W7-X Team. (2023). Erosion and redeposition pattern on the W7-X graphite test divertor unit tile. Fusion Engineering and Design, 191, Artkl.Nr.: 113589. doi:10.1016/j.fusengdes.2023.113589

Shcherbinin, V. I.; Thumm, M.; Jelonnek, J. (2023). Low Ohmic Losses and Mode Selectivity Provided by a Distributed Bragg Reflector for Cavities of Terahertz Gyrotrons. IEEE Transactions on Electron Devices, 70 (7), 3848–3854. doi:10.1109/TED.2023.3274505

ASDEX Upgrade Team; Fable, E.; David, P.; Kudlacek, O.; Hopf, C.; Sieglin, B.; Stober, J.; Treutterer, W.; Weiland, M.; Wu, C.; Zohm, H. (2023). A practical protocol to emulate a reactor scenario on present machines, with application to the ASDEX Upgrade tokamak via predictive modeling. Nuclear Fusion, 63 (7), Article no: 074001. doi:10.1088/1741-4326/acd205

W7-X Team; Schmidt, B. S.; Salewski, M.; Moseev, D.; Baquero-Ruiz, M.; Hansen, P. C.; Eriksson, J.; Ford, O.; Gorini, G.; Järleblad, H.; Kazakov, Y. O.; Kulla, D.; Lazerson, S.; Mencke, J. E.; Mykytchuk, D.; Nocente, M.; Poloskei, P.; Rud, M.; Snicker, A.; Stagner, L.; Äkäslompolo, S. (2023). 4D and 5D phase-space tomography using slowing-down physics regularization. Nuclear Fusion, 63 (7), Article no: 076016. doi:10.1088/1741-4326/acd6a6

W7-X Team; Kontula, J.; Äkäslompolo, S.; Ikäheimo, A.; Lazerson, S.; Kurki-Suonio, T.; Hartmann, D.; Rust, N.; McNeely, P.; Kazakov, Y. O.; Ongena, J. (2023). Predictive simulations of NBI ion power load to the ICRH antenna in Wendelstein 7-X. Plasma Physics and Controlled Fusion, 65 (7), Article no: 075008. doi:10.1088/1361-6587/acd07e

W7-X Team; Wegner, T.; Bähner, J.-P.; Buttenschön, B.; Langenberg, A.; von Stechow, A. (2023). Overview of core impurity transport in the first divertor operation of Wendelstein 7-X. Journal of Plasma Physics, 89 (3), Article: 955890302. doi:10.1017/S0022377823000417

Jabłoński, B.; Puig Sitjes, A.; Makowski, D.; Jakubowski, M.; Gao, Y.; Fischer, S.; Winter, A.; Wendelstein 7-X Team. (2023). Implementation and performance evaluation of the real-time algorithms for Wendelstein 7-X divertor protection system for OP2.1. Fusion Engineering and Design, 190, Art.-Nr.: 113524. doi:10.1016/j.fusengdes.2023.113524

Merlo, A.; Böckenhoff, D.; Schilling, J.; Lazerson, S. A.; Pedersen, T. S.; W7-X Team. (2023). Physics-regularized neural network of the ideal-MHD solution operator in Wendelstein 7-X configurations. Nuclear Fusion, 63 (6), Arkl.Nr.: 066020. doi:10.1088/1741-4326/acc852

W7-X Team; Haak, V.; Bozhenkov, S. A.; Feng, Y.; Kharwandikar, A.; Kremeyer, T.; Naujoks, D.; Perseo, V.; Schlisio, G.; Wenzel, U. (2023). Overview over the neutral gas pressures in Wendelstein 7-X during divertor operation under boronized wall conditions. Plasma Physics and Controlled Fusion, 65 (5), Article no: 055024. doi: 10.1088/1361-6587/acc8fb

di Grazia, L. E.; Fable, E.; Frattolillo, D.; Mattei, M.; David, P.; Wu, C. (2023). Development of magnetic control for the EU-DEMO flight simulator and application to transient phenomena. Fusion Engineering and Design, 191, Artkl.Nr.: 113579. doi: 10.1016/j.fusengdes.2023.113579

Shcherbinin, V. I.; Tkachova, T. I.; Thumm, M.; Jelonnek, J. (2023). Self-Consistent Modeling of Beam-Wave Interaction in Complex Gyrotron Cavities with Azimuthal Slots. 2022 IEEE 2nd Ukrainian Microwave Week (UkrMW), Ukraine, 14-18 November 2022, 258–262, Institute of Electrical and Electronics Engineers (IEEE). doi:10.1109/UkrMW58013.2022.10037054

W7-X Team; Laqua, H. P.; Avramidis, K. A.; Braune, H.; Chelis, I.; Gantenbein, G.; Illy, S.; Ioannidis, Z.; Jelonnek, J.; Jin, J.; Krier, L.; Lechte, C.; Leggieri, A.; Legrand, F.; Marsen, S.; Moseev, D.; Oosterbeek, H.; Rzesnicki, T.; Ruess, T.; Stange, T.; Thumm, M.; Tigelis, I.; Wolf, R. C. (2023). The ECRH-Power Upgrade at the Wendelstein 7-X Stellarator. (E. Poli, Y. Liu & V. Udintsev, Hrsg.) EPJ Web of Conferences, 277, Art.-Nr.: 04003. doi:10.1051/epjconf/202327704003

Wagner, D.; Leuterer, F.; Plaum, B.; Schütz, H.; Stober, J.; Thumm, M. (2024). Beam Quality Measurements at the ASDEX Upgrade ECRH system. 2024 49th International Conference on Infrared, Millimeter, and

Terahertz Waves (IRMMW-THz), Perth, Australia, 01-06 September 2024, Institute of Electrical and Electronics Engineers (IEEE). doi:10.1109/IRMMW-THz60956.2024.10697576

Leggieri, A.; Avramidis, K. A.; Chelis, I.; Difonzo, R.; Ell, B.; Feuerstein, L.; Gajetti, E.; Gantenbein, G.; Gontard, J.; Illy, S.; Ioannidis, Z.; Jelonnek, J.; Jin, J.; Kohler, S.; Laqua, H.; Legrand, F.; Lievin, C.; Marchesin, R.; Marsen, S.; Noke, F.; Oumar, I. M.; Ponomarenko, S.; Ruess, T.; Rzesnicki, T.; Savoldi, L.; Stanculovic, S.; Stange, T.; Tigelis, I.; Vallée, E.; Wolf, R.; Thumm, M. (2024). Thales TH1507U 140 GHz 1.5 MW CW Industrial Gyrotron for W7-X ECRH System Upgrade. Joint International Vacuum Electronics Conference and International Vacuum Electron Sources Conference (IVEC + IVESC), 23-25 April 2024 , Monterey, 1–2, Institute of Electrical and Electronics Engineers (IEEE). doi:10.1109/IVECIVESC60838.2024.10694887

Leggieri, A.; Albajar, F.; Alberti, S.; Avramidis, K. A.; Bertazzoni, R.; Bin, W.; Bonetti, D.; Braunmueller, F. H.; Bruschi, A.; Cammi, A.; Chelis, I.; Dall'Acqua, D.; Difonzo, R.; Feuerstein, L.; Gajetti, E.; Gantenbein, G.; Garavaglia, S.; Genoud, J.; Gontard, J.; Goodman, T. P.; Granucci, G.; Hogge, J.-P.; Illy, S.; Introini, C.; Ioannidis, Z.; Jelonnek, J.; Jin, J.; Legrand, F.; Lievin, C.; Marchesin, R.; Oumar, I. M.; Romano, A.; Rzesnicki, T.; Sanchez, F.; Savoldi, L.; Stanculovic, S.; Tigelis, I.; Vallée, E.; Thumm, M. (2024). Industrial Qualification of the THALES TH1509U European 170 GHz 1 MW CW Gyrotron. 25th Joint International Vacuum Electronics Conference and International Vacuum Electron Sources Conference (IVEC + IVESC), 23-25 April 2024, Monterey, 1–2, Institute of Electrical and Electronics Engineers (IEEE). doi:10.1109/IVECIVESC60838.2024.10694857

Ruess, T.; Wagner, D.; Feuerstein, L.; Gantenbein, G.; Rzesnicki, T.; Stanculovic, S.; Thumm, M.; Jelonnek, J. (2024). Quasi-Optical Mode Generator for Excitation of Very High-Order Modes up to 240 GHz. 49th International Conference on Infrared, Millimeter, and Terahertz Waves (IRMMW-THz), 1st-6th September 2024, Perth, 1–2, Institute of Electrical and Electronics Engineers (IEEE). doi:10.1109/IRMMW-THz60956.2024.10697753

Ponomarenko, S.; Laqua, H. P.; Avramidis, K. A.; Gantenbein, G.; Gontard, J.; Hollmann, F.; Illy, S.; Ioannidis, Z. C.; Jelonnek, J.; Jin, J.; Kohler, S.; Krier, L.; Leggieri, A.; Legrand, F.; Lietaer, G.; Lievin, C.; Marsen, S.; Moseev, D.; Noke, F.; Rzesnicki, T.; Stange, T.; Thumm, M.; Wolf, R. C. (2024). Experimental Results of the Novel 1.5-MW-Class 140-GHz Continuous-Wave Gyrotron for the Wendelstein 7-X Stellarator. IEEE Electron Device Letters, 45 (12), 2550–2553. doi:10.1109/LED.2024.3484218

Wendelstein 7-X Team; Han, X.; Smith, D. R.; Windisch, T.; Laube, R.; Den Hartog, D.; Seyfert, C.; Gallenberger, T.; Jaehnig, K.; Geiger, B.; McKee, G.; Grulke, O. (2024). Beam emission spectroscopy diagnostic design and capabilities for two-dimensional turbulence measurements on Wendelstein 7-X. Journal of Instrumentation, 19 (11), Article no: P11004. doi:10.1088/1748-0221/19/11/P11004

Genoud, J.; Alberti, S.; Hogge, J.-P.; Avramidis, K.; Braunmüller, F.; Bruschi, A.; Bin, W.; Dubray, J.; Fasel, D.; Gantenbein, G.; Garavaglia, S.; Goodman, T.; Illy, S.; Jin, J.; Legrand, F.; Marchesin, R.; Pagonakis, I.; Siravo, U.; Toussaint, M. (2024). Experimental characterization of the TCV dual-frequency gyrotron and validation of numerical codes including the effect of After Cavity Interaction. (E. Poli, E. Choi, S. Wang & G. Yun, Hrsg.) EPJ Web of Conferences, 313, Art.-Nr.: 04008. doi:10.1051/epjconf/202431304008

Poli, E.; Figini, L.; Fable, E.; Siccinio, M.; Snicker, A.; Wu, C.; Zohm, H. (2024). ECCD studies for EU-DEMO plasmas. (E. Poli, E. Choi, S. Wang & G. Yun, Hrsg.) EPJ Web of Conferences, 313, Art.-Nr.: 01005. doi:10.1051/epjconf/202431301005

Braunmueller, F.; Goodman, T. P.; Genoud, J.; Albajar, F.; Alberti, S.; Avramidis, K. A.; Bertazzoni, R.; Bin, W.; Bonetti, D.; Bruschi, A.; Cammi, A.; Cavinato, M.; Chelis, I.; Dall'Acqua, D.; Difonzo, R.; Feuerstein, L.; Gajetti, E.; Gantenbein, G.; Garavaglia, S.; Gontard, J.; Granucci, G.; Hogge, J.-P.; Illy, S.; Introini, C.; Ioannidis, Z.; Jelonnek, J.; Jin, J.; Leggieri, A.; Legrand, F.; Lievin, C.; Marchesin, R.; Oumar, I. M.; Picas, O.; Romano, A.; Rzesnicki, T.; Sanchez, F.; Savoldi, L.; Stanculovic, S.; Tigelis, I.; Vallée, E.; Thumm, M. (2024). Results on the 1 MW CW 170 GHz gyrotron TH1509UA for ITER and DTT at the FALCON test stand. EPJ Web of Conferences, 313, Art.-Nr.: 04005. doi:10.1051/epjconf/202431304005

Wagner, D.; Leuterer, F.; Monaco, F.; Schütz, H.; Stober, J.; Thumm, M. (2024). In-situ Low Power Tests of the ASDEX Upgrade ECRH Transmission Lines. EPJ Web of Conferences, 313, Article no: 04001. doi:10.1051/epjconf/202431304001

Ell, B.; Wu, C.; Feuerstein, L.; Gantenbein, G.; Illy, S.; Ruess, T.; Rzesnicki, T.; Stanculovic, S.; Thumm, M.; Weggen, J.; Jelonnek, J. (2024). Fabrication and assembly of the gyrotron multi-stage depressed collector prototype at KIT. EPJ Web of Conferences, 313, Art.-Nr.: 04006. doi:10.1051/epjconf/202431304006

Maksymenko, O.; Shcherbinin, V.; Feuerstein, L.; Jelonnek, J.; Thumm, M. (2024). Capacity of an Irregular Gyrotron Cavity to Provide an Increase in Output Power. Joint International Vacuum Electronics Conference and International Vacuum Electron Sources Conference (IVEC + IVESC 2024), 2 S., Institute of Electrical and Electronics Engineers (IEEE). doi:10.1109/IVECIVESC60838.2024.10694816

Ruess, T.; Eppli, J.; Feuerstein, L.; Gantenbein, G.; Illy, S.; Jin, J.; Rzesnicki, T.; Stanculovic, S.; Thumm, M.; Jelonnek, J. (2024). Recent Developments of the 2 MW Coaxial-Cavity Pre-Prototype Gyrotron Towards Multi-Frequency Operation. 2024 Joint International Vacuum Electronics Conference and International Vacuum Electron Sources Conference (IVEC + IVESC), Monterey, 23rd-25th April 2024, 01–02, Institute of Electrical and Electronics Engineers (IEEE). doi:10.1109/IVECIVESC60838.2024.10694856

Feuerstein, L.; Shcherbinin, V. I.; Avramidis, K. A.; Chelis, I.; Illy, S.; Jelonnek, J.; Peponis, D.; Tigelis, I.; Thumm, M.; Wu, C. (2024). MW Level 280 GHz 2nd Harmonic Coaxial Gyrotron Cavity with Variable Corrugation Depth. 2024 Joint International Vacuum Electronics Conference and International Vacuum Electron Sources Conference (IVEC + IVESC), Monterey, CA, USA, 23-25 April 2024, 01–02, Institute of Electrical and Electronics Engineers (IEEE). doi:10.1109/IVECIVESC60838.2024.10694886

W7-X Team; Bold, D.; Reimold, F.; Niemann, H.; Gao, Y.; Jakubowski, M.; Killer, C.; Winters, V. R.; Maaziz, N. (2024). Impact of spatially varying transport coefficients in EMC3-Eirene simulations of W7-X and assessment of drifts. Nuclear Fusion, 64 (12), 126055. doi:10.1088/1741-4326/ad845c

Mayer, M.; Balden, M.; Bräuer, T.; Cipciar, D.; Dhard, C. P.; Drews, P.; Elgeti, S.; Höschen, D.; Killer, C.; D. Naujoks; Sandri, N.; Schmid-Dencker, J.-H.; Vanó, L.; Viebke, H.; Volzke, O.; W7-X Team. (2024). Properties of boron layers deposited during boronisations in W7-X. Nuclear Materials and Energy, 41, Art.-Nr.: 101778. doi:10.1016/j.nme.2024.101778

W7-X Team; Winters, V. R.; Reimold, F.; Feng, Y.; Zhang, D.; Perseo, V.; Flom, E. R.; Henke, F.; Kriete, D. M.; Maaziz, N.; Partesotti, G.; Jakubowski, M.; König, R.; Krychowiak, M.; Brunner, K. J.; Knauer, J.; Rahbarnia, K. (2024). First experimental confirmation of island SOL geometry effects in a high radiation regime on W7-X. Nuclear Fusion, 64 (12), Art.-Nr.: 126047. doi:10.1088/1741-4326/ad820e

W7-X Team; Bussiahn, R.; Tamura, N.; McCarthy, K. J.; Buttenschön, B.; Brandt, C.; Dinklage, A.; Langenberg, A. (2024). Commissioning of the tracer-encapsulated solid pellet (TESPEL) injection system for Wendelstein

7-X and first results for OP1.2b. Plasma Physics and Controlled Fusion, 66 (11), Art.-Nr.: 115020. doi:10.1088/1361-6587/ad8185

W7-X Team; Partesotti, G.; Reimold, F.; Ruhnau, J.; Tsikouras, A.; Kubeneck, D.; Zhang, D.; Geißler, P. (2024). Development of a compact bolometer camera concept for investigation of radiation asymmetries at Wendelstein 7-X. Review of Scientific Instruments, 95 (10), Art.-Nr.: 103503. doi:10.1063/5.0207762

W7-X Team; Swee, C.; Geiger, B.; Ford, O.; O'Mullane, M.; Poloskei, P.; Reimold, F.; Romba, T.; Wegner, T. (2024). High-n Rydberg transition spectroscopy for heavy impurity transport studies in W7-X (invited). Review of Scientific Instruments, 95 (9), Art.-Nr.: 093539. doi:10.1063/5.0219589

W7-X Team; Wappl, M.; Bozhenkov, S. A.; Beurskens, M. N. A.; Bannmann, S.; Kuczyński, M. D.; Smith, H. M.; Brunner, K. J.; Ford, O. P.; Fuchert, G.; Knauer, J. P.; Langenberg, A.; Pablant, N. A.; Pasch, E.; Poloskei, P. Z.; Wolf, R. C. (2024). Web apps for profile fitting and power balance analysis at Wendelstein 7-X. Review of Scientific Instruments, 95 (9), Article no: 093529. doi:10.1063/5.0225315

W7-X Team; Terry, J. L.; Stechow, A. von; Baek, S. G.; Ballinger, S. B.; Grulke, O.; Sehren, C. von; Laube, R.; Killer, C.; Scharmer, F.; Brunner, K. J.; Knauer, J.; Bois, S. (2024). Realization of a gas puff imaging system on the Wendelstein 7-X stellarator. Review of Scientific Instruments, 95 (9), Art.-Nr.: 093517. doi:10.1063/5.0219336

W7-X Team; Kwak, S.; Hoefel, U.; Krychowiak, M.; Langenberg, A.; Svensson, J.; Trimino Mora, H.; Ghim, Y.-C. (2024). Bayesian modelling of multiple plasma diagnostics at Wendelstein 7-X. Nuclear Fusion, 64 (10), Article no: 106022. doi:10.1088/1741-4326/ad6e02

W7-X Team; Chaudhary, N.; Hirsch, M.; Andreeva, T.; Geiger, J.; Wolf, R. C.; Wurden, G. A. (2024). Electron transport barrier and high confinement in configurations with internal islands close to the plasma edge of W7-X. Nuclear Fusion, 64 (10), Article no: 106038. doi:10.1088/1741-4326/ad703e

W7-X Team; Verdier, T.; Vann, R. G. L.; Jacobsen, A. S.; Jensen, T.; Rasmussen, J.; Ragona, R.; Nielsen, S. K. (2024). An ultrafast digitizer for continuous measurements from microwave fusion diagnostics. Fusion Engineering and Design, 206, Article no: 114597. doi:10.1016/j.fusengdes.2024.114597

W7-X Team; Fuchert, G.; Wagner, J.; Henschke, L. V.; Pasch, E.; Beurskens, M. N. A.; Bozhenkov, S. A.; Brunner, K. J.; Chen, S.; Frank, J. M.; Hirsch, M.; Knauer, J.; Wolf, R. C. (2024). Calibration techniques for Thomson scattering diagnostics on large fusion experiments. Review of Scientific Instruments, 95 (8), Article no: 083533. doi:10.1063/5.0219161

W7-X Team; Bannmann, S.; Ford, O.; Poloskei, P. Z.; Svensson, J.; Pavone, A.; Kwak, S.; Hoefel, U.; Pasch, E.; Fuchert, G.; Smith, H. M.; Lazerson, S.; McNeely, P.; Rust, N.; Hartmann, D.; Wolf, R. C. (2024). Particle transport in reduced turbulence neutral beam heated discharges at Wendelstein 7-X. Nuclear Fusion, 64 (10), Article no: 106015. doi:10.1088/1741-4326/ad6b37

Grulke, O.; Albert, C.; Alcuson Belloso, J. A.; Aleynikov, P.; Aleynikova, K.; Alonso, A.; Anda, G.; Andreeva, T.; Arvanitou, M.; Ascasibar, E.; Aymerich, E.; Avramidis, K.; Bähner, J.-P.; Baek, S.-G.; Balden, M.; Baldzuhn, J.; Ballinger, S.; Banduch, M.; Bannmann, S.; Bañón Navarro, A.; Baylor, L.; Beidler, C. D.; Beurskens, M.; Biedermann, C.; Birkenmeier, G.; Bluhm, T.; Boeckenhoff, D.; Boeyaert, D.; Bold, D.; Borchardt, M.; Borodin, D.; Bosch, H.-S.; Bouvain, H.; Bozhenkov, S.; Bräuer, T.; Braune, H.; Brandt, C.; Brezinsek, S.; Brunner, K. J.; Büschel, C.; Bussiahn, R.; Buzás, A.; Buttenschoen, B.; Bykov, V.; Calvo, I.; Cappa, A.; Carovani, F.; Carralero,

D.; Carls, A.; Carvalho, B.; Castaño-Bardawil, D.; Chaudhary, N.; Chelis, I.; Chen, S.; Cipciar, D.; Coenen, J. W.; Conway, G.; Cornelissen, M.; Corre, Y.; Costello, P.; Crombe, K.; Cseh, G.; Csillag, B.; Cu Castillo, H. I.; Czymek, G.; Damm, H.; Davies, R. J.; Day, C.; Degenkolbe, S.; De Wolf, R.; Dekeyser, W.; Demby, A.; Despontin, P.; Dhard, C. P.; Dinklage, A.; d'Isa, F. A.; Dittmar, T.; Dreval, M.; Drevlak, M.; Drews, P.; Droste, J.; Dunai, D.; Dyhring, C.; Eeten, P. van; Edlund, E.; Endler, M.; Ennis, D. A.; Escoto, F. J.; Espinosa, M. S.; Estrada, T.; Fehling, D.; Feuerstein, L.; Fellinger, J.; Feng, Y.; Fernando, D. L. C.; Fischer, S.; Flom, E. R.; Ford, O.; Fornal, T.; Frank, J.; Frerichs, H.; Fuchert, G.; Gantenbein, G.; Gao, Y.; Garcia, K.; García-Cortés, I.; García-Regaña, J. M.; Geiger, B.; Geiger, J.; Geissler, P.; Gerard, M.; Godino-Sedano, G.; Gonda, T.; González, A.; Goriaev, A.; Gradic, D.; Grahl, M.; Greuner, H.; Grigore, E.; Gruca, M.; Guerrero Arnaiz, J. F.; Haak, V.; Ham, L. van; Hammond, K.; Hamstra, B.; Han, X.; Hansen, S. K.; Harris, J.; Hartmann, D.; Hathiramani, D.; Hegedus, S.; Heinrich, S.; Helander, P.; Henke, F.; Henneberg, S.; Henschke, L.; Hirsch, M.; Hoefel, U.; Hoefler, K.; Hoermann, S.; Hollfeld, K.-P.; Holtz, A.; Höschen, D.; Houry, M.; Huang, J.; Huang, J.; Hubeny, M.; Hunger, K.; Hwangbo, D.; Ida, K.; Igitkhanov, Y.; Illy, S.; Ioannidis, Z.; Jablczynska, M.; Jablonski, S.; Jabłoński, B.; Jagielski, B.; Jakubowski, M.; Jelonnek, J.; Jenko, F.; Jin, J.; Johansson, A.; Jouniaux, G.; Kajita, S.; Kallmeyer, J.-P.; Kamionka, U.; Kasparek, W.; Kawan, C.; Kazakov, Y. O.; Kenmochi, N.; Kernbichler, W.; Kharwandikar, A. K.; Khokhlov, M.; Killer, C.; Kirschner, A.; Kleiber, R.; Klepper, C. C.; Klinger, T.; Knauer, J.; Knieps, A.; Kobayashi, M.; Kocsis, G.; Kolesnichenko, Y.; Könies, A.; Kontula, J.; Kornejew, P.; Korteweg, S. A.; Koschinsky, J.; Koster, J.; Kovtun, Y.; Krämer-Flecken, A.; Krause, M.; Kremeyer, T.; Krier, L.; Kriete, D. M.; Krychowiak, M.; Ksia˛zek, I.; Kubkowska, M.; Kuczyński, M. D.; Kulla, D.; Kumar, A.; Kurki-Suonio, T.; Kuzmych, I.; Kwak, S.; Lancelotti, V.; Langenberg, A.; Laqua, H.; Laqua, H. P.; Larsen, M. R.; Lazerson, S.; Lechte, C.; Lee, B.; LeViness, A.; Lewerentz, M.; Liang, Y.; Liao, L.; Litnovsky, A.; Liu, J.; Loizu, J.; Lopez-Cansino, R.; Lopez Rodriguez, L. D.; Lorenz, A.; Lunsford, R.; Luo, Y.; Lutsenko, V.; Maaziz, N.; Machielsen, M.; Mackenbach, R.; Makowski, D.; Maragkoudakis, E.; Marchuk, O.; Markl, M.; Marsen, S.; Martínez, J.; Marushchenko, N.; Masuzaki, S.; Maurer, D. A.; Mayer, M.; McCarthy, K. J.; McNeely, P.; Medina Roque, D.; Meineke, J.; Meitner, S.; Mendes, S. vaz; Menzel-Barbara, A.; van Milligen, B.; Mishchenko, A.; Moiseenko, V.; Möller, A.; Möller, S.; Moseev, D.; Motojima, G.; Mulas, S.; Mulholland, P.; Nagel, M.; Nagy, D.; Narbutt, Y.; Naujoks, D.; Nelde, P.; Neu, R.; Neubauer, O.; Neuner, U.; Nicolai, D.; Nielsen, S.; Nührenberg, C.; Ochoukov, R.; Offermanns, G.; Ongena, J.; Oosterbeek, J. W.; Otte, M.; Pablant, N.; Panadero Alvarez, N.; Pandey, A.; Partesotti, G.; Pasch, E. A.; Pavlichenko, R.; Pawelec, E.; Pedersen, T. S.; Perseo, V.; Peterson, B.; Pisano, F.; Plaum, B.; Plunk, G.; Podavini, L.; Polei, N. S.; Poloskei, P.; Ponomarenko, S.; Pons-Villalonga, P.; Porkolab, M.; Proll, J.; Pueschel, M. J.; Puig Sitjes, A.; Ragona, R.; Rahbarnia, K.; Rasiński, M.; Rasmussen, J.; Refy, D.; Reimold, F.; Richou, M.; Riemann, J. S.; Riße, K.; Riva Villén, J. de la; Roberg-Clark, G.; Rodriguez, E.; Rohde, V.; Romazanov, J.; Romba, T.; Rondeshagen, D.; Rud, M.; Ruess, T.; Rummel, T.; Runov, A.; Ruset, C.; Rust, N.; Ryc, L.; Rzesnicki, T.; Salewski, M.; Sánchez, E.; Sanchis Sanchez, L.; Satheeswaran, G.; Schacht, J.; Scharff, E.; Schilling, J.; Schlisio, G.; Schmid, K.; Schmitt, J. C.; Schmitz, O.; Schneider, M.; Van Schoor, M.; Schröder, T.; Schroeder, R.; Schweer, B.; Sereda, S.; Shanahan, B.; Sias, G.; Simko, S.; Singh, L.; Siusko, Y.; Slaby, C.; Śle˛czka, M.; Smith, B. S.; Smith, D. R.; Smith, H.; Spolaore, M.; Spring, A.; Stange, T.; Stechow, A. von; Stepanov, I.; Stern, M.; Stroth, U.; Suzuki, Y.; Swee, C.; Syrocki, L.; Szabolics, T.; Szepesi, T.; Takacs, R.; Takahashi, H.; Tamura, N.; Tantos, C.; Terry, J.; Thiede, S.; Thienpondt, H.; Thomsen, H.; Thumm, M.; Thun, T.; Togo, S.; Tork, T.; Trimino Mora, H.; Tsikouras, A.; Turkin, Y.; Vano, L.; Varoutis, S.; Vecsei, M.; Velasco, J. L.; Verstraeten, M.; Vervier, M.; Viezzer, E.; Wagner, J.; Wang, E.; Wang, F.; Wappl, M.; Warmer, F.; Wegner, T.; Wei, Y.; Weir, G.; Wendler, N.; Wenzel, U.; White, A.; Wilms, F.; Windisch, T.; Winter, A.; Winters, V.; Wolf, R.; Wurden, G.; Xanthopoulos, P.; Xiang, H. M.; Xu, S.; Yamada, H.; Yang, J.; Yi, R.; Yokoyama, M.; Zamorski, B.; Zanini, M.; Zarnstorff, M.; Zhang, D.; Zhou, S.; Zhu, J.; Zimmermann, J.; Zocco, A.; Zoletnik, S. (2024). Overview of the first Wendelstein 7-X long pulse campaign with fully water-cooled plasma facing components. Nuclear Fusion, 64 (11), Article no: 112002. doi:10.1088/1741-4326/ad2f4d

W7-X Team; Lopez-Cansino, R.; Perseo, V.; Viezzer, E.; Ford, O. P.; Kriete, M.; Romba, T.; Rueda-Rueda, J.; Poloskei, P. Z.; Reimold, F. (2024). 2D core ion temperature and impurity density measurements with Coherence Imaging Charge Exchange Recombination Spectroscopy (CICERS) at Wendelstein 7-X (invited). Review of Scientific Instruments, 95 (8), Art.-Nr.: 083524. doi:10.1063/5.0219483

W7-X Team; Ford, O. P.; Langenberg, A.; Romba, T.; Pölöskei, P.; Zanini, M.; Bannmann, S.; Gonda, T.; Ida, K.; Lopez Cansino, R.; Pablant, N.; de la Riva Villen, J.; Swee, C.; Yoshinuma, M.; Alonso, A.; Geiger, B.; Perseo, V.; Viezzer, E. (2024). Visible core spectroscopy at Wendelstein 7-X. Review of Scientific Instruments, 95 (8), Art.-Nr.: 083526. doi:10.1063/5.0219469

W7-X Team; Wilms, F.; Bañón Navarro, A.; Windisch, T.; Bozhenkov, S.; Warmer, F.; Fuchert, G.; Ford, O.; Zhang, D.; Stange, T.; Jenko, F. (2024). Global gyrokinetic analysis of Wendelstein 7-X discharge: unveiling the importance of trapped-electron-mode and electron-temperature-gradient turbulence. Nuclear Fusion, 64 (9), Art.-Nr.: 096040. doi:10.1088/1741-4326/ad6675

W7-X Team; LeViness, A.; Lazerson, S. A.; Jansen van Vuuren, A.; Rueda-Rueda, J.; Beurskens, M.; Bozhenkov, S.; Brunner, K. J.; Ford, O. P.; Fuchert, G.; Garcìa-Muñoz, M.; Isobe, M.; Killer, C.; Knauer, J.; Ogawa, K.; Pablant, N.; Pasch, E.; Poloskei, P.; Romba, T. (2024). Validation of a synthetic fast ion loss detector model for Wendelstein 7-X. Nuclear Fusion, 64 (9), Art.-Nr.: 096034. doi:10.1088/1741-4326/ad6885

Bruschi, A.; Hogge, J.-P.; Jelonnek, J.; Strauss, D.; Wu, C.; Aiello, G.; Avramidis, K.; Baiocchi, B.; Birlan, D.; Chavan, R.; Chelis, I.; Clement, A.; Collaku, A.; Crisinel, F. P.; Difonzo, R.; Ell, B.; Fanale, F.; Fanelli, P.; Figini, L.; Gajetti, E.; Gantenbein, G.; Garavaglia, S.; Goodman, T. P.; Illy, S.; Ioannidis, Z.; Jin, J.; Latsas, G.; Marraco Borderas, C. L.; Marsen, S.; Moro, A.; Noël, M.; Peponis, D.; Pinna, T.; Platania, P.; Rispoli, N.; Ruess, T.; Rzesnicki, T.; Salvitti, A.; Savoldi, L.; Scherer, T.; Schreck, S.; Simonetto, A.; Spaeh, P.; Stanculovic, S.; Stange, T.; Thumm, M.; Tigelis, I. G.; Tsironis, C.; Wagner, D.; Xydou, A. (2024). Conceptual Design of a Modular EC Heating System for EU-DEMO. Nuclear Fusion, 54 (10), Art.-Nr.: 106003. doi:10.1088/1741-4326/ad66e3

W7-X Team; LeViness, A.; Lazerson, S. A.; Jansen van Vuuren, A.; Rueda-Rueda, J.; Ayllon-Guerola, J.; Bozhenkov, S.; Corl, D.; Ellis, R.; Galdon-Quiroga, J.; Garcia-Dominguez, J.; Garcia-Munoz, M.; Hidalgo-Salaverri, J.; Ogawa, K.; Pablant, N.; Segado-Fernandez, J. (2024). Simulation of a scintillator-based fast ion loss detector for steady-state operation in Wendelstein 7-X (invited). Review of Scientific Instruments, 95 (7), Art.-Nr.: 073529. doi:10.1063/5.0214788

W7-X Team; Lazerson, S. A.; Kulla, D.; McNeely, P.; Rust, N.; Ham, L. van; Hartmann, D. (2024). OPTEMIST: A neutral beam for measuring quasi-omnigenity in Wendelstein 7-X. Physics of Plasmas, 31 (7), Art.-Nr.: 072506. doi:10.1063/5.0218670

W7-X Team; Csillag, B. G.; Anda, G.; Cseh, G.; Dunai, D.; Ford, O. P.; Flom, E.; Gradic, D.; Henke, F.; Krychowiak, M.; Nagy, D.; Otte, M.; Réfy, D. I.; Tőkési, K.; Vécsei, M.; Zoletnik, S. (2024). Charge exchange recombination spectroscopy on the alkali beam of Wendelstein 7-X. Review of Scientific Instruments, 95 (7), Art.-Nr.: 073524. doi:10.1063/5.0219461

W7-X Team; Ford, O. P.; Beurskens, M.; Bozhenkov, S. A.; Lazerson, S.; Vanó, L.; Alonso, A.; Baldzuhn, J.; Beidler, C. D.; Biedermann, C.; Burhenn, R.; Fuchert, G.; Hartmann, D.; Hirsch, M.; Langenberg, A.; Laqua, H.; McNeely, P.; Pablant, N.; Pasch, E.; Reimold, F.; Romba, T.; Rust, N.; Schroeder, R.; Scott, E. R.; Stange, T.; Smith, H. M.; Gradic, D.; Wolf, R. C.; Zhang, D. (2024). Turbulence-reduced high-performance scenarios in Wendelstein 7-X. Nuclear Fusion, 64 (8), Art.-Nr.: 086067. doi:10.1088/1741-4326/ad5e99

W7-X Team; Swee, C.; Geiger, B.; Ford, O.; Nornberg, M.; O'Mullane, M.; Poloskei, P.; Reimold, F.; Romba, T.; Wegner, T. (2024). Impurity transport study based on measurement of visible wavelength high-n charge exchange transitions at W7-X. Nuclear Fusion, 64 (8), Article no: 086062. doi:10.1088/1741-4326/ad5aad

W7-X Team; Kriete, D. M.; Perseo, V.; Gradic, D.; Ennis, D. A.; König, R.; Maurer, D. A. (2024). Multi-delay coherence imaging spectroscopy optimized for ion temperature measurements in the divertor plasma of the Wendelstein 7-X stellarator. Review of Scientific Instruments, 95 (7), Art.-Nr.: 073503. doi:10.1063/5.0208586

W7-X Team; Feng, Y.; Winters, V.; Zhang, D.; Geiger, J.; Gao, Y.; Reiter, D.; Helander, P.; Beidler, C. D.; Endler, M.; Gradic, D.; Jakubowski, M.; König, R.; Kremeyer, T.; Krychowiak, M.; Naujoks, D.; Otte, M.; Perseo, V.; Reimold, F.; Schlisio, G. (2024). Conditions and benefits of X-point radiation for the island divertor. Nuclear Fusion, 64 (8), Article no: 086027. doi:10.1088/1741-4326/ad5606

Wendelstein 7-X Team; Hansen, S. K.; Porkolab, M.; Bähner, J.-P.; Stechow, A. von; Grulke, O.; Edlund, E. M. (2024). Localized phase contrast imaging at the Wendelstein 7-X stellarator. Physics of Plasmas, 31 (6), Article no: 062302. doi:10.1063/5.0197958

W7-X Team; González-Jerez, A.; García-Regaña, J. M.; Calvo, I.; Carralero, D.; Estrada, T.; Sánchez, E.; Barnes, M. (2024). Electrostatic microturbulence in W7-X: comparison of local gyrokinetic simulations with Doppler reflectometry measurements. Nuclear Fusion, 64 (7), Article no: 076029. doi:10.1088/1741-4326/ad411a

W7-X Team; Syrocki, Ł.; Kubkowska, M.; Jabłoński, S.; Neuner, U. (2024). Theoretical interpretation of W soft X-ray spectra collected by the pulse height analysis system on Wendelstein 7-X stellarator. Physics of Plasmas, 31 (6), Article no: 063303. doi:10.1063/5.0210977

W7-X Team; Gao, Y.; Geiger, J.; Jakubowski, M. W.; Pandey, A.; Bozhenkov, S.; Feng, Y.; Endler, M.; Baldzuhn, J.; Perseo, V.; Kremeyer, T.; Schlisio, G.; Puig Sitjes, A.; Otte, M.; Naujoks, D.; Krychowiak, M.; König, R.; Zhang, D.; Szepesi, T.; Kocsis, G.; Cseh, G.; Buzás, A.; Pisano, F.; Knieps, A. (2024). Heat and particle exhaust in high-performance plasmas in Wendelstein 7-X. Nuclear Fusion, 64 (7), Article no: 076060. doi:10.1088/1741-4326/ad5364

W7-X Team; Zanini, M.; Aymerich, E.; Böckenhoff, D.; Merlo, A.; Aleynikova, K.; Brandt, C.; Braune, H.; Brunner, K. J.; Hirsch, M.; Höfel, U.; Knauer, J.; Laqua, H. P.; Marsen, S.; Pavone, A.; Rahbarnia, K.; Schilling, J.; Smith, T.; Stange, T.; Thomsen, H.; Wolf, R. C.; Zocco, A. (2024). Automated W7-X sawtooth crashes detection and characterization. Nuclear Fusion, 64 (7), Art.-Nr.: 076027. doi:10.1088/1741-4326/ad490b

W7-X Team; Jansen van Vuuren, A.; Garcia-Dominguez, J.; Hidalgo-Salaverri, J.; Segado-Fernandez, J.; LeViness, A.; Ayllon-Guerola, J.; Rueda-Rueda, J.; Lazerson, S. A.; Galdon-Quiroga, J.; Garcia-Munoz, M.; Pablant, N. (2024). Development of a scintillator based fast-ion loss detector for the Wendelstein 7-X stellarator. Fusion Engineering and Design, 204, Article no: 114520. doi:10.1016/j.fusengdes.2024.114520

W7-X Team; Varoutis, S.; Tantos, C.; Strobel, H.; Day, C.; Dhard, C. P.; Haak, V.; Igitkhanov, Y.; Naujoks, D. (2024). Numerical simulation of neutral gas dynamics in the W7-X sub-divertor. Nuclear Fusion, 64 (7), 076011. doi:10.1088/1741-4326/ad49b5

W7-X Team; Langenberg, A.; Warmer, F.; Fuchert, G.; Ford, O.; Bozhenkov, S.; Andreeva, T.; Lazerson, S.; Pablant, N. A.; Gonda, T.; Beurskens, M. N. A.; Brunner, K.-J.; Buttenschön, B.; Dinklage, A.; Hartmann, D.;

Knauer, J.; Marchuk, O.; Pasch, E.; Reimold, F.; Stange, T.; Wegner, T.; Grulke, O.; Wolf, R. C. (2024). Achieving stationary high performance plasmas at Wendelstein 7-X. Physics of Plasmas, 31 (5), Article no: 042022. doi:10.1063/5.0199958

W7-X Team; Pandey, A.; Bohm, S.; Carls, A.; Cordes, C.; Endler, M.; Fellinger, J.; Freundt, S.; Gallowski, K.; Hammond, K.; Hathiramani, D.; Isberner, G.; Kallmeyer, J. P.; Krause, M.; Kügler, J.; Otte, M.; Pedersen, T. S.; Rondeshagen, D.; Ruhnau, J.; Schröder, T.; Sieber, T.; Wendorf, J. (2024). Pop-up Langmuir probe diagnostic in the water cooled divertor of Wendelstein 7-X. Review of Scientific Instruments, 95 (4), Article no: 043503. doi:10.1063/5.0188738

W7-X Team; Bannmann, S.; Ford, O.; Hoefel, U.; Poloskei, P. Z.; Pavone, A.; Kwak, S.; Svensson, J.; Lazerson, S.; McNeely, P.; Rust, N.; Hartmann, D.; Pasch, E.; Fuchert, G.; Langenberg, A.; Pablant, N.; Brunner, K. J.; Wolf, R. C. (2024). Bayesian inference of electron density and ion temperature profiles from neutral beam and halo Balmer-α emission at Wendelstein 7-X. Plasma Physics and Controlled Fusion, 66 (6), Article no: 065001. doi:10.1088/1361-6587/ad3c1d

W7-X Team; Winters, V. R.; Reimold, F.; Feng, Y.; Perseo, V.; Beurskens, M.; Bozhenkov, S.; Brunner, K. J.; Fuchert, G.; Koenig, R.; Knauer, J.; Krychowiak, M.; Pasch, E.; Scott, E.; Zhang, D. (2024). Impurity leakage mechanisms in the Wendelstein 7-X island divertor under friction-dominated conditions. Nuclear Fusion, 64 (5), Article no: 056042. doi:10.1088/1741-4326/ad3768

Moseev, D.; Ponomarenko, S.; Laqua, H. P.; Stange, T.; Nielsen, S. K.; Braune, H.; Gantenbein, G.; Illy, S.; Jelonnek, J.; Kasparek, W.; Kuleshov, A.; Krier, L.; Lechte, C.; Marsen, S.; Nishiura, M.; Plaum, B.; Ragona, R.; Ruess, T.; Salewski, M.; Stordiau, P.; Thumm, M.; Wolf, R. C.; Zimmermann, J.; W7-X team. (2024). Commissioning and first results of the 174 GHz collective Thomson scattering diagnostic at Wendelstein 7-X. Journal of Instrumentation, 19 (03), Art.-Nr. C03056. doi:10.1088/1748-0221/19/03/C03056

W7-X Team; Lopez-Cansino, R.; Perseo, V.; Viezzer, E.; Kriete, D. M.; Ford, O. P.; Romba, T.; Poloskei, P. Z. (2024). First measurements with a Coherence Imaging Charge Exchange Recombination Spectroscopy (CICERS) diagnostic at Wendelstein 7-X. Plasma Physics and Controlled Fusion, 66 (4), 045012. doi:10.1088/1361-6587/ad290e

Wendelstein 7-X Team; Büschel, C.; Kleiber, R.; Könies, A.; Drevlak, M.; Borchardt, M.; Rahbarnia, K.; Thomsen, H.; Vaz Mendes, S.; Brandt, C.; Knauer, J.; Brunner, K. J. (2024). Synthetic Mirnov diagnostic for the validation of experimental observations. Review of Scientific Instruments, 95 (2), Article no: 023506. doi:10.1063/5.0190619

Mondal, D.; Yuvaraj, S.; Rawat, M.; Thumm, M.; Kartikeyan, M. V. (2024). Investigations on the Output System of 300-GHz Gyrotrons. IEEE Transactions on Plasma Science, 52 (3), 690–697. doi:10.1109/TPS.2024.3357837

Spaeh, P.; Bruschi, A.; Chavan, R.; Clément, A.; Crisinel, F.; Cufar, A.; Fanale, F.; Garavaglia, S.; Hogge, J. P.; Sanchez, A. M.; Noël, M.; Rispoli, N.; Strauss, D.; Wu, C. (2024). Design Progress of Structural Components of the EU DEMO EC Equatorial Launcher. IEEE Transactions on Plasma Science, 52 (9), 3580–3585. doi:10.1109/TPS.2024.3353822

Chelis, I. G.; Avramidis, K. A.; Peponis, D. V.; Ioannidis, Z. C.; Latsas, G. P.; Illy, S.; Jelonnek, J.; Tigelis, I. G. (2024). High-Frequency MW-class Coaxial Gyrotron Cavities Operating at the Second Cyclotron Harmonic. IEEE Transactions on Electron Devices, 71 (3), 2140–2146. doi:10.1109/TED.2024.3356472

Introini, C.; Badodi, N.; Bertazzoni, R.; Carannante, G.; Hogge, J.-P.; Illy, S.; Leggieri, A.; Sanchez, F.; Sanchez, F.; Savoldi, L. (2024). Sensitivity Analysis of the Lumped Thermal Model of the EU 170 GHz Gyrotron Magnetron Injection Gun. IEEE Transactions on Plasma Science, 52 (9), 3836–3841. doi:10.1109/TPS.2023.3348171

W7-X Team; Poloskei, P. Z.; Geiger, B.; Jansen van Vuuren, A.; Äkäslompolo, S.; Ford, O. P.; Spanier, A.; Neelis, T. W. C.; McNeely, P.; Hartmann, D. (2024). Experimental characterization of the active and passive fast-ion H-alpha emission in W7-X using FIDASIM. Nuclear Fusion, 64 (2), Art.-Nr.: 026008. doi:10.1088/1741-4326/ad0dd4

W7-X Team; Ponomarenko, S.; Moseev, D.; Stange, T.; Krier, L.; Stordiau, P.; Braune, H.; Gantenbein, G.; Jelonnek, J.; Kuleshov, A.; Laqua, H. P.; Lechte, C.; Marsen, S.; Nielsen, S. K.; Oosterbeek, J. W.; Plaum, B.; Ragona, R.; Rasmussen, J.; Ruess, T.; Salewski, M.; Thumm, M.; Zimmermann, J. (2024). Development of the 174 GHz collective Thomson scattering diagnostics at Wendelstein 7-X. Review of Scientific Instruments, 95 (1), Article no: 013501. doi:10.1063/5.0174444

W7-X Team; Boeyaert, D.; Feng, Y.; Frerichs, H.; Kremeyer, T.; Naujoks, D.; Reimold, F.; Schmitz, O.; Winters, V.; Bozhenkov, S.; Fellinger, J.; Jakubowski, M.; König, R.; Krychowiak, M.; Perseo, V.; Schlisio, G.; Wenzel, U. (2024). Analysis of the neutral fluxes in the divertor region of Wendelstein 7-X under attached and detached conditions using EMC3-EIRENE. Plasma Physics and Controlled Fusion, 66 (1), Article no: 015005. doi:10.1088/1361-6587/ad0e22

W7-X Team; Csillag, B.; Zoletnik, S.; Killer, C.; Vecsei, M.; Anda, G.; Dunai, D.; Hegedus, S.; Refy, D.; Nagy, D.; Otte, M. (2024). Statistical analysis of plasma filaments in the island divertor of Wendelstein 7-X. Nuclear Fusion, 64, Article no: 016017. doi:10.1088/1741-4326/ad0af7

Wu, C.; David, P.; Fable, E.; Frattolillo, D.; Di Grazia, L. E.; Mattei, M.; Siccinio, M.; Treutterer, W.; Zohm, H. (2024). Architecture Design and Internal Implementation of a Universal Coupling Between Controllers and Physics in a Tokamak Flight Simulator. Fusion Science and Technology, 80 (6), 766–771. doi:10.1080/15361055.2023.2234741

2 Renewable Energy (RE): Bioenergy -Feedstocks and Pretreatment-

Contact: Prof. Dr.-Ing. Georg Müller

2.1 PEF-Processing of microbial biomass

Contact: Dr. Wolfgang Frey

2.1.1 PEF-assisted solvent extraction of lipids from oleaginous yeasts: Study on the different strains' characteristics, conditions of downstream processing and solvent efficiency.

Oleaginous yeasts are considered to be a promising renewable source of lipids that can be transformed into various oleochemicals, such as biodiesel or biolubricants. Yeasts' ability to use low-cost carbon sources and to produce lipids at high rates, combined with their short cultivation times and independence from arable lands and climate conditions, make them strong competitors to vegetable oils. In this context, the Elegant project, the frame of this research, aims to develop a sustainable and cost-efficient process to produce and extract oils from oleaginous yeast for its usage as biolubricants. In particular, the IHM work is focused on the downstream process, exploring the use of Pulsed Electric Fields (PEF) processing as a low-energy cell-pretreatment and identifying green solvents for the effective extraction of intracelullar lipids from yeasts.

Four strains of oleaginous yeasts (*Cutaneotrichosporon oleaginosum, Saitozyma podzolica*, *Apiotrichum porosum* and *Scheffersomyces segobiensis*) were cultivated and provided by the Institut für Bio- und Lebensmitteltechnik 2 (BLT2, KIT). Biomasses were grown in a bioreactor with glucose as carbon source under different cultivation conditions (nitrogen limitation, phosphate limitation and unlimited conditions). Yeast biomasses were characterized in terms of cell dry weight (CDW), electrical conductivity (mS/cm), pH and total lipid content ($\%_{CDW}$). The harvested biomass was pretreated in continuous flow at 6 mL/min by PEF (40 kV/cm, 50 kJ/L or 150 kJ/L) before undergoing solvent extraction (20 h of extraction time). Various solvents or solvent systems including ethanol, hexane, MTBE, ethyl-acetate or MeTHF were tested. Lipid yields were determined gravimetrically after solvent evaporation. Whether an incubation time of 24 h after PEF and the medium's osmolarity during this incubation could contribute to increasing lipids yield was also studied.

Fig. 2.1.1 and Fig. 2.1.2 show the values of cell dry weight and total lipid content for the different yeast strains under all the cultivation conditions investigated. High cell dry weigths values ranging from 20 to 35 g/L were obtained for all the strains in at least one of the cultivation conditions. In the case of lipid content, the maximun values were obtained under nitrogen limitation conditions being 48 %, 36 % and 29 % respectively for *C. oleaginosum*, *S. podzolica* and *A. porosum*. On the contrary, the maximum lipid content obtained for *S. segobiensis* was less than 16 % under phosphate limitation. Furthermore, electrical conductivity values ranged from 5 to 10 mS/cm under nitrogen conditions, while under unlimited of phosphate limitation these values were 10 times higher (50 to 100 mS/cm). Based on these results, the following lipid extraction experiments were focused on *C. oleaginosum*, *S. podzolica* and *A. porosum* grown under nitrogen conditions.
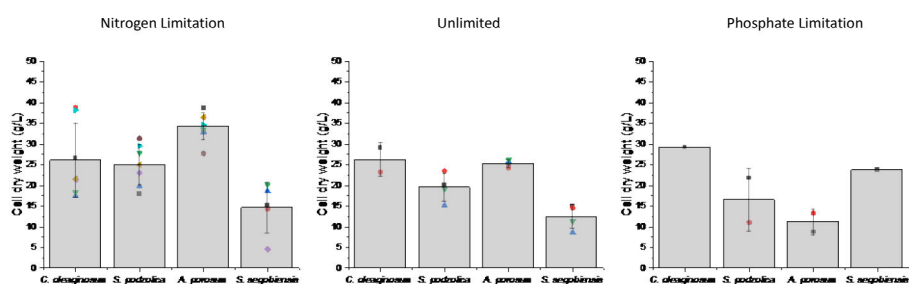
Fig. 2.1.1:   Cell dry weight (grams per litter of biomass) obtained for the different yeast strains studied grown under nitrogen limitation, unlimited conditions of phosphate limitation.
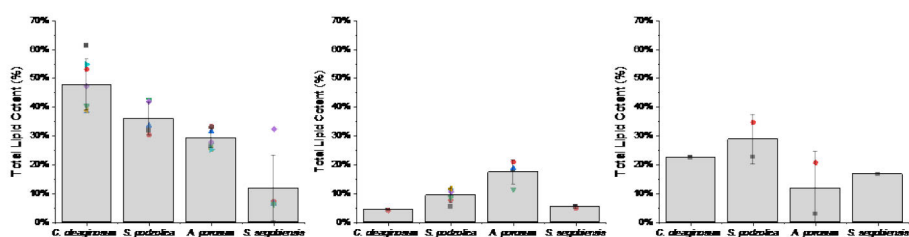
Fig. 2.1.2:   Total lipid content (% of the CDW) obtained for the different yeast strains studied grown under nitrogen limitation, unlimited conditions of phosphate limitation.

Lipid extraction experiments revealed that great extraction yields from 80 to 99 % of the total lipids were reached in all the strains evaluated, although by different strategies, Table 1. The successful lipid extraction on *S. podzolica* and *A. porosum* required PEF treatment plus an incubation period before solvent admixture. On the other hand, no pre-treatment was necessary for *C. oleaginosum* achieving after the solvent extraction step lipid yields from 70 to 90 % of the total content either by ethanol-hexane blends or alternative solvents like MTBE or MeTHF.

Strain	% Total Lipid Content Extracted	Downstream Processing
C. oleaginosum	87.3 %	**Untreated** biomass + Extraction in MTBE or **MeTHF**
S. podzolica	83 %	**PEF** + 24h **incubation** (↓ osmo) + Extraction in **MeTHF**
A. porosum	83 %	**PEF** + 24h **incubation** (↓ osmo) + Extraction in **Ethanol-hexane** blend

Table 1: Relation between the downstream processing conditions for each yeast strain studied and the total lipid yield obtained. PEF treatments: 50 kJ/kg. Biomass to solvent ratio: 37 g/L. Extraction time: 20 h.

After PEF processing of *S. podzolica*, an incubation step of 24 hours in the same treatment media increased the extraction yields from 23 to 62.8 % of the total lipids when using ethanol-hexane blends. However, the lipid yields improved even more (up to 99 %) when the incubation after PEF was performed in a low osmolarity medium. When same PEF and incubation conditions were applied and the extraction was performed in MeTHF, 83 % of the total lipids were extracted. In the case of *A. porosum,* only PEF plus incubation in a low osmolarity medium was efficient for lipid extraction (78 % of total lipids) using ethanol-hexane blends. The high efficieny of MeTHF - considered as a green solvent and easy to recycle - in extracting lipids from *C. oleaginosum* and *S. podzolica* opens a promising approach for further optimization.

Collaboration: BLT 2 - Electro Biotechnology, CS

2.1.2 Cultivation of oil-producing yeasts at IHM

At the end of this year, we took a significant step for our research infrastructure, namely the acquisition of a modern commercial biofermenter. The Minifors 2, manufactured by INFORS HT, enables us to precisely cultivate and research a wide range of microorganisms.

The Minifors 2 is characterized by its modern technology, which enables precise control of the cultivation conditions. The culture vessel has a working volume of 3 liters, which corresponds to a working volume of 2 liters. Parameters such as temperature, stirring speed and gassing are fully adjustable via an integrated digital touchscreen, creating a customized environment for different microorganisms. Particularly noteworthy is the integrated pump system, which not only enables automatic sensory monitoring and regulation of the pH value, but also allows nutrients to be added easily during the cultivation process.

As part of the Elegant project at the IHM, we are planning to use the Minifors 2 for the cultivation of oil-producing yeasts in the so-called fed-batch process. Our current focus is on the yeast strain *Cutaneotrichosporon oleaginosum*, which is of great interest due to its potential as an oil producer for biotechnological applications. This yeast culture is cultivated in the absence of light with glucose as the main carbon source. In the future, we intend to investigate other substances such as glycerol and molasses as more cost-effective alternatives.

After successfully carrying out a test cultivation, the Minifors 2 was used for production of biomass from *S. podzolica* and *C. oleaginosum* for subsequent lipid extraction experiments.

Collaboration: BLT 2 - Electro Biotechnology, CS

2.1.3 Lipid Extraction with Ethanol from *Auxenochlorella protothecoides* (A.p.)

It is well known that ethanol has been extensively used in food and pharmaceutical industries, because ethanol is a sustainable and environment-friendly organic solvent. In the past years, the Bioelectrics group has demonstrated that ethanol-hexane blends can extract lipids from A.p. effectively. Compared with ethanol-hexane blends, using a water-ethanol mixture for lipid extraction first and then transferring the lipids to the second organic phase consisting of pure n-Hexane, leaving the water-ethanol phase lipid-free, can be more economical.

In order to obtain the best extraction conditions, this study mainly focussed on the effect of ethanol concentration, ethanol volume and buffers with different pH on extraction efficiency. Furthermore, the influence of incubation time and extraction time was studied for ethanol percentages of 95 %.

For all processing conditions the lipid yield increases with the concentration of ethanol added to the biomass, Fig. 2.1.3, (A). Due to the azeotropic nature of ethanol water mixtures, ethanol recycling for re-use in extraction requires high amounts of energy if the required purity exceeds 96 %. Thus, further extraction experiments were performed with ethanol at a purity of 95 %.

The determination of the extraction time kinetics revealed, that after 3 h of extraction a stationary yield value was achieved. An extraction time of 20 h only marginally increases the lipid yield. Already 15 min after solvent admixture a yield value of 25.1%CDW could be obtained, Fig. 2.1.3, (B).
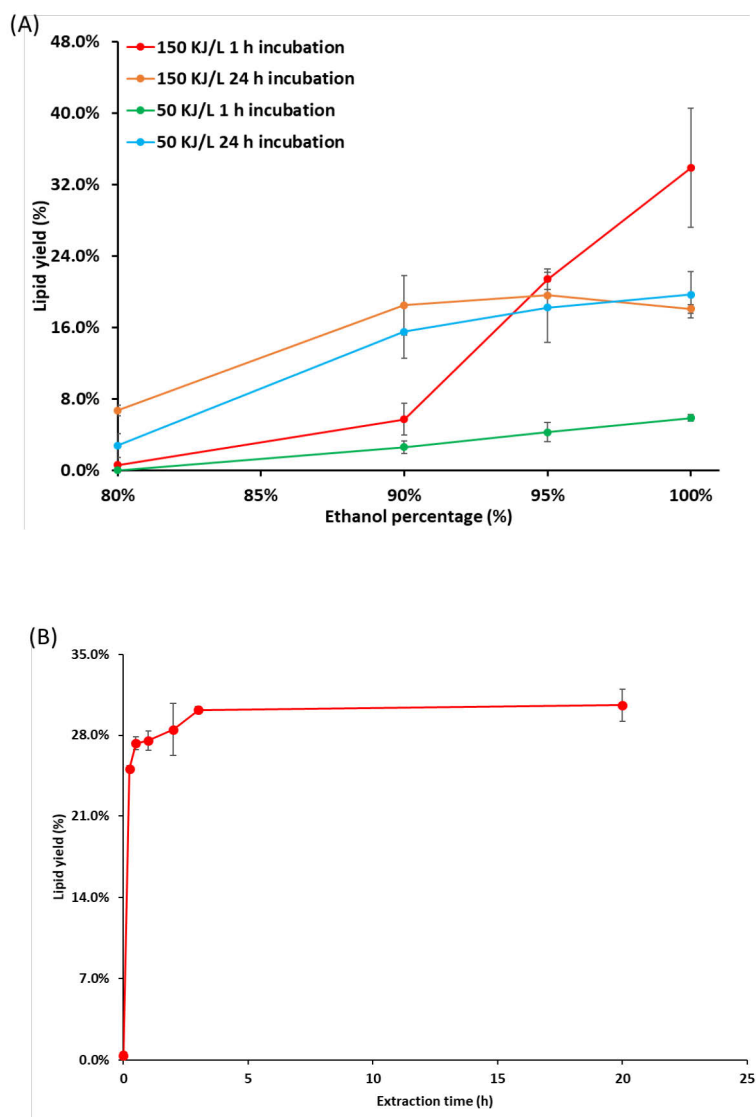
Fig. 2.1.3:   (A) Lipid extraction with different ethanol concentrations, PEF treatment energies and incubation times; (B) Lipid extraction with different extraction time (95% ethanol, 4 h incubation). Lipid yield is given in percentage of dry cell weight (dw). The average of the total lipid content was 38 %$_{dw}$.

Results on variation of the incubation time after PEF treatment demonstrate, that the lipid yield exhibits a maximum at about 8 h of incubation after PEF treatment with 150 kJ/L Fig. 2.1.4, (A), wheras at 50 kJ/L longer incubation periods were more advantageous, Fig. 2.1.4, (B). The highest lipid yield of 32 %$_{dw}$ could be achieved with a PEF treatment at 150 kJ/L.

To verify above measured tendency, a more detailed study on the effect of ethanol purity, specific PEF treatment energy and duration of incubation after PEF treatment was performed. The Response Surface Method (RSM) was utilized to better illustrate the influence of the three factors on the lipid extraction from *A.p*. In the RSM experiments, the extraction time was set to 3 h, and the PEF energy was 0, 50 kJ/L, 150 kJ/L, the ethanol purity was 90%, 95%, 100%, incubation time was 1 h, 4 h and 24 h. We carried out ESM analysis for the data from 71 experimental groups of independent batches of *A.p*. microalgae.
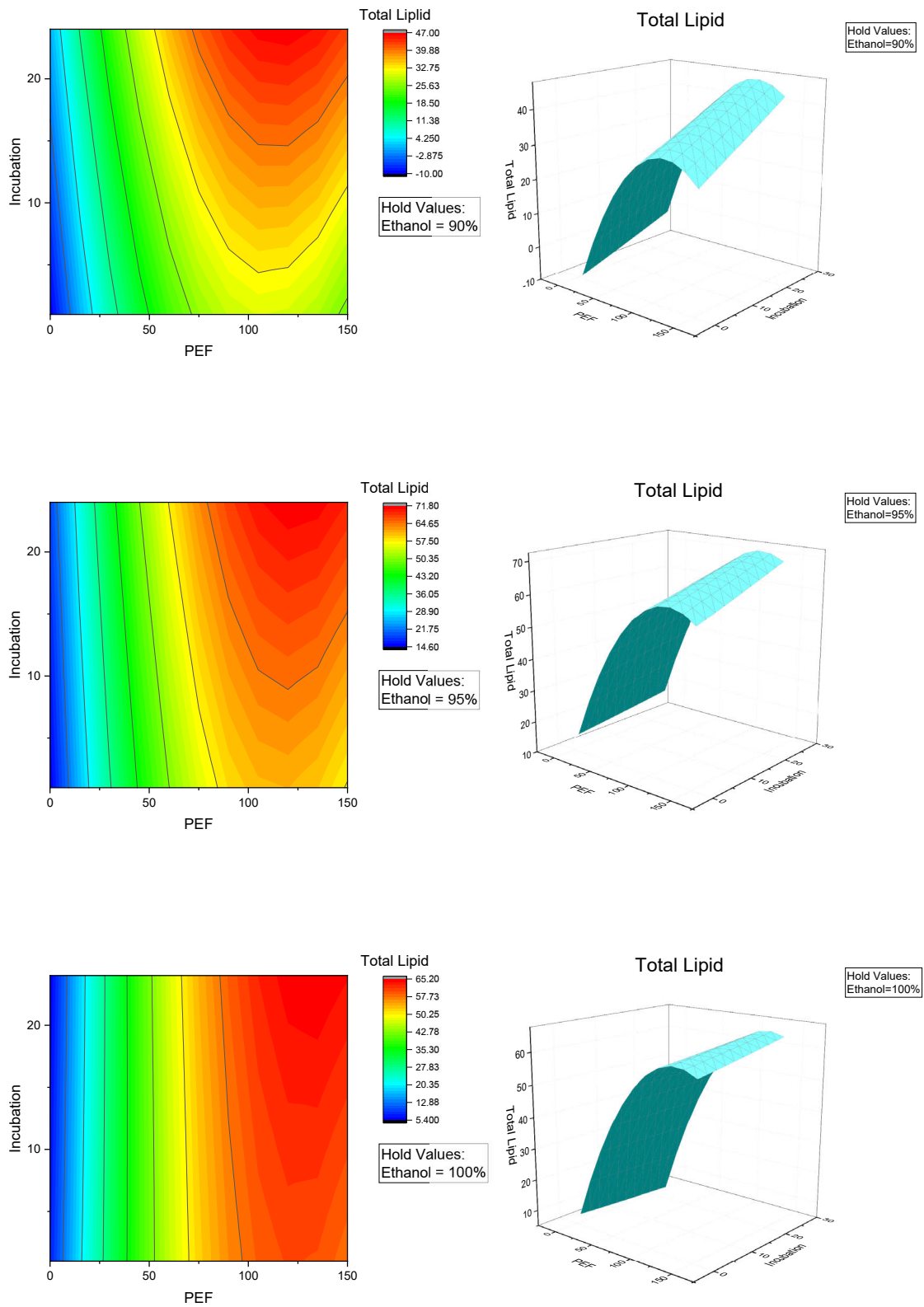
Fig. 2.1.4: The ESM analysis of the effects of PEF energy, ethanol percentage and incubation time on percentage of total lipid content extracted from *A. protothecoides*.

RSM analysis revealed, that an ethanol purity of 95 % and higher is required for achieving lipid yields on the order of 70 %. Extraction with ethanol at a purity of 90 % only allows to recover 47 % of the intracellularly stored lipids, Fig. 2.1.4, upper row. For all cases, the lipid yield increases with specific PEF-treatment energy and with incubation time. The higher the ethanol purity, the broader is the range of incubation time periods which result in high lipid yields.

Future techno-economic evaluations have to show whether the application of ethanol with a purity of 95 % for lipid extraction at a moderate yield of around 70 % can equalize increased solvent recycling efforts needed for the highly efficient ethanol/hexane extraction, which requires higher volumes of solvents per unit of recovered lipids.

2.1.4 PEFassisted protein extraction from mixed cultures of microalgae and bacteria

This study was supported by the Deutsche Bundesstiftung Umwelt (DBU) as part of an international collaboration with the Centre for Physical Sciences and Technology, Vilnius, Lithuania. Microalage demonstrate remarkable potential to reshape protein production and consumption patterns, with benefits that outshine traditional protein sources. The rapid growth and the efficient nutrient utilization make them an environmentally friendly protein source. They require minimal land and water, in stark contrast to resource-intensive livestock farming. Algae cultivation also thrives in diverse environments, using spaces unsuitable for traditional agriculture.

However, there are a number of challenges associated with large-scale cultivation under aseptic conditions. Some of the key reasons include contamination issue and the genetic homogeneity of monocultures. Maintaining aseptic conditions is costly and challenging due to the potential for contamination by other microorganisms. Bacteria, fungi, or other algae can quickly proliferate in the culture, leading to a loss of the desired monoculture. Monocultures often result in genetic homogeneity, making the population more vulnerable to diseases or environmental changes that affect specific genetic traits. Therefore, the cultivation of mixed cultures of microalgae and bacteria is an approach that has gained much attention in recent years and offers several advantages over monoculture, such as: symbiotic relationships between bacteria and microalgae, recycling of wastewater and other organic waste substrates by bacteria, and increased stability of the culture to environmental fluctuations, resulting in a more robust and reliable culture system.

In our previous study we have shown that the interaction between microalgae (*Chlorella vulgaris*) and bacteria (*Delftia sp.*) is not solely determined by species specificity, rather, it is a dynamic process of adaptation to the surrounding conditions, where one or the other microorganism dominates (temporally). Depending on the growth conditions, in particular the composition of the growth medium, it was possible to achieve stable cultivation with biomass densities similar to those of monocultures, while viable bacterial populations remained below critical levels.

In this study, we aimed to investigate the influence of bacteria on the quality and yield of proteins obtained after PEF pretreatment. In a second approach, PEF treatment was used as a method to selectively inactivate bacteria and microalgae in order to gain an understanding of the ecosystem dynamics potentially affecting the microalgae biorefinery. By investigating various parameters at different growth stages, including PEF-specific treatment energy, we aimed to unravel the complex dynamics of PEF application in a mixed culture environment. Other important aspects of our investigation were the effects of microalgae and bacterial growth stages on PEF efficiency, the dynamics of bacterial inactivation, the viability of algae after PEF

treatment, the antibacterial properties of algal PEF extracts, and the changes in extracted proteins due to the presence of bacteria.

The obtained results reveal that PEF treatment exhibited consistent efficiency on *C. vulgaris* inactivation exceeded 95% for all PEF treatments, showing no dependence on the cell growth stage. In contrast, the impact on bacteria displayed variability. PEF efficiency in inactivating bacteria relied on the cell growth phase and cultivation conditions (alone or with algae). An important result was that the bacteria can recover during the incubation step after PEF treatment. However, the protein yield obtained after PEF treatment did not change compared to that of monocultures (approx. 50 % of the total protein content). This indicates that the bacteria do not use the released protein as a nutrient substrate during the subsequent 24 hours of incubation, Fig. 2.1.5.
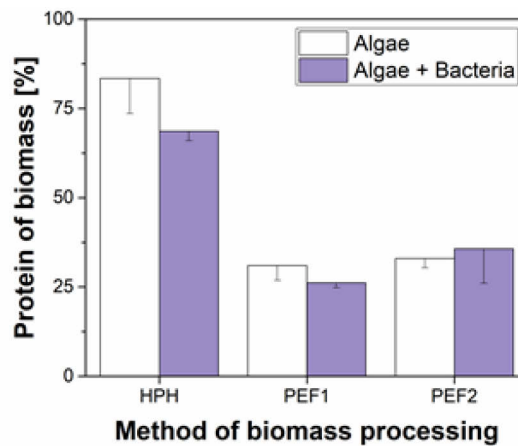
Fig. 2.1.5: Protein yield after pretreatment of algal biomass with PEF and HPH. *C. vulgaris* was cultivated alone or in co-culture with Delftia sp.

Furthermore, SDS-PAGE profiles after PEF treatment showed no significant differences between algae cultured alone and in the presence of bacteria. However, after HPH treatment, a subtle but statistically insignificant decrease in the amount of protein was observed in the sample of algae grown with bacteria. In addition, the SDS-PAGE gel, Fig. 2.1.6, revealed at least one prominent additional protein band in the HPH protein extract from the algal and bacterial samples compared to the algal sample alone which was attributed to proteins released from bacteria.The estimated molecular weight of this band, based on the molecular marker migration, was approximately 27 kDa.
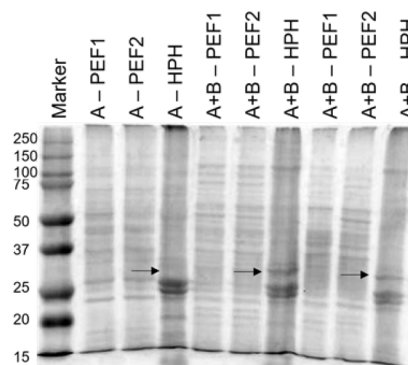
Fig. 2.1.6: Visualisation of protein extracts obtained by HPH and PEF treatment by SDS-PAGE. Samples obtained from concentrated *C. vulgaris* biomass (5 g/l) cultivated alone (A) or co-cultivated with bacteria (A+B).

This is a potential contaminant for HPH extracts derived from co-cultures of algae and bacteria, as they may be harmful or toxic when used as a dietary supplement in the human diet or as a feed additive. In view of this, PEF treatment appears to have the potential to selectively extract proteins from algae and bacteria, especially when low specific energies are applied that do not affect the viability of the bacteria and thus proteins are not released from them.

In summary, this study contributes to the understanding of the effects of PEF treatments in mixed cultures, in particular the influence of bacteria on the efficiency of microalgae utilisation and the resulting product yield, but also safety aspects such as contamination with undesirable molecules of bacterial origin. Although mixed cultures offer some advantages, the economic feasibility of such approaches depends on factors such as the target products, the cultivation methods and the scalability of the system. Ongoing research in this area aims to optimise the extraction technique and fully exploit the potential of mixed cultures for various applications, taking into account food safety and environmental concerns.

Collaboration: Centre for Physical Sciences and Technology, Vilnius, Lithuania

2.1.5 Biological signalling supports biotechnology: cell death triggers protein release from *Chlorella vulgaris*

Several studies have shown that after PEF treatment, an incubation step in buffer for more than 6 h (at 23-39°C and pH between 8 and 9) is required to improve the bioaccessibility of cell components such as proteins and lipids. The main reason for this has been shown to be enzymatic processes that occur during incubation and improve the release of proteins and facilitate solvent extraction of lipids from different microlayer types. This autolytic process can be triggered by various methods, e.g. by dark anoxia, in which the microalgae are incubated in the dark for 24 h to 48 h, or by PEF treatment even with very low specific energies (< 5 J/g).

In particular, in *C. vulgaris*, there is evidence that a specific cell death inducing factor (CDIF) of protein origin causes cell death in intact cells. The current concept implies that the CDIF plays an important role during the algae incubation period for protein extraction after PEF treatment, by triggering cell death in intact cells and subsequent autolytic processes, leading to an enhanced extraction process. The search for the identity of the CDIF led to the assumption that radical oxygen species (ROS) could play a decisive role as a signalling molecule involved in many cell signalling pathways. One possible mechanism of cell death triggered in *C. vulgaris* is based on the implication of L-amino acid oxidase (LAAO), a flavoenzyme that catalyzes stereospecific oxidative deamination of an L-amino acid to form corresponding α-keto acid along with ammonia and hydrogen peroxide (H_2O_2). It has been shown that LAAOs can induce cell death in yeast and several mammalian cancer cell lines as well as in the diatom *Phaeodactylum tricornutum*.

To clarify this possible mechanism, we investigated the development of intra- and intercellular ROS production during incubation of fresh algal suspensions with algal extract containing CDIF, as well as in extract only. Whereas algal cell death induced by PEF treatment, even at low specific treatment energies, leads to a dramatic increase in intracellular ROS, no changes in inter- and intracellular ROS could be measured due to cell incubation with CDIF containing extract. One reason for this result is that the algae extract not only contains CDIF, but also a high concentration of molecules with antioxidant properties that automatically suppress ROS. This finding suggests that ROS depletion interferes with signalling pathways in the cell, which in turn leads to programmed cell death. To test this new hypothesis, we investigated the citotoxicity of antioxidants such as trolox, glutathione and ascorbic acid on algal cells at different concentrations. Surprisingly, ascorbic acid was able to increase algal mortality during a 24 h incubation

period and also enabled the release of proteins that correlated with algal mortality. In addition, the combination of PEF treatment and the addition of ascorbic acid results in an increase in protein yield of more than 20%, Fig. 2.1.7. This finding holds significance as the synergistic application of cell disruption and ascorbic acid not only has the potential to enhance the yield of extracted cell components from algae but also preserves them from oxidative degradation. Furthermore, the antibacterial properties of ascorbic acid play a crucial role in controlling bacterial proliferation, particularly in mixed cultures of algae and bacteria.
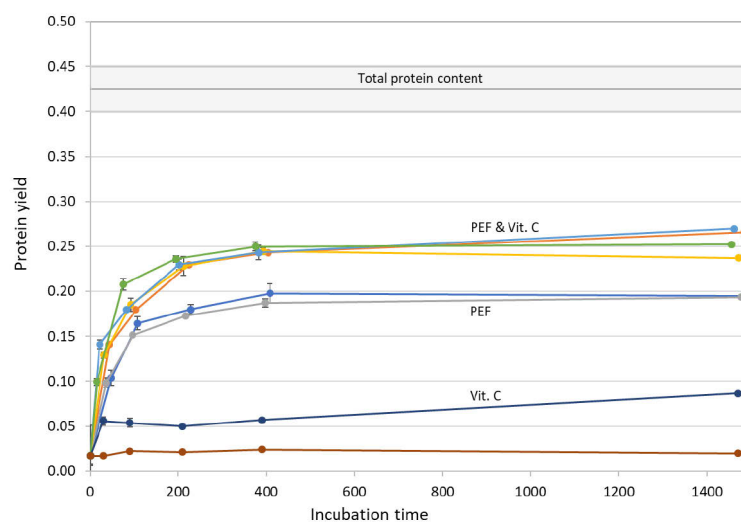
Fig. 2.1.7: Time course of protein release from *C. vulgaris* alagal biomass after pre-treatment with PEF and combination of PEF and ascorbic acid (vit. C). Addition of ascorbic acid alone also resulted in protein release during incubation.

This result has the potential to optimise the extraction process by minimising energy costs for cell disruption and increasing product safety, laying a new approach to sustainable biotechnology. This would allow for the development of new downstream processes that align with environmentally conscious practices, marking a significant step towards a more sustainable and efficient approach in biotechnological applications.

Collaboration: Botanical Institute, KIT Campus South

2.1.6 EU-Project SusAlageFuel: "Exploring the synergies between direct carbon-capture, nutrient recovery and next-generation purification technologies for cost-competitive and sustainable microalgal aviation fuel development of microalgae fuel production and purification technologies for advanced aviation fuels"

SusAlgaeFuel aims to revolutionize the production of sustainable aviation fuels (SAFs) from microalgae by integrating cost-efficient, circular, and scalable technologies. Key innovations include the use of CO_2 emissions and nutrient-rich waste from anaerobic digestion (AD) to support algae growth, advanced monitoring and purification tools to prevent culture contamination, and an energy-saving biorefinery for efficient biomass fractionation, Fig. 2.1.8. The project also develops algae-specific thermocatalytic pathways for efficient conversion of algae-lipids to Hydroprocessed Esters Fatty Acids-Synthetic Paraffinic Kerosene (HEFA-SPK) to meet aviation standards, supported by comprehensive economic, environmental, and policy analyses. With a total budget of approximately 4 million EUR distributed among 9 partners (3

universities, 1 research and technology organization, and 5 subject matter experts) from 5 European countries, SusAlgaeFuel culminates in a pilot facility in Ireland. This facility demonstrates the project's potential to transform EU energy independence by enabling significant waste valorization and contributing to 20% of Europe's SAF targets for 2030.
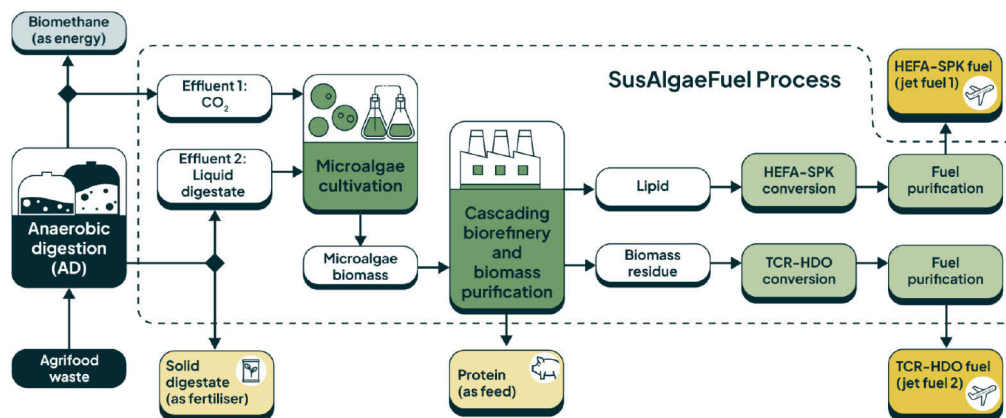

Fig. 2.1.8: Graphical Abstract of the EU-project SusAagaeFuel.

The SusAlgaeFuel project officially was kicked off on 25 May 2024 and is scheduled to run for a total duration of 4 years. The Bioelectrics group is actively involved in WP3: "Cascading biorefinery for biomass purification", which focuses on two key tasks: 1. autolytic cell-wall disruption for direct processing of wet microalgae and 2. solvent screening, recycling, and emulsion management. To support this work, a qualified biochemist was hired in September 2024, marking the official start of our activities in WP3. Initial efforts have been dedicated to laying the groundwork for task execution and ensuring smooth progress towards achieving the project objectives.

Collaboration: University College Dublin, A4F-Algafuel, S.A.

2.1.7 Investigation of electrode corrosion in pulsed electric field (PEF)-processes, using austenitic, stainless steel (AISI 316Ti) electrodes in combination with different processing electrolytes

For a better understanding of the corrosion behavior of high voltage (HV) electrodes during PEF-processing, electrical treatment parameters, applied electrolytes, electrode materials and processing duration need to be varied. Investigation of this influencing factors can help to find appropriate techno-economic solutions with respect to relevant, individual PEF-processing applications.

In a first approach two different electrolytes were evaluated, derived from different applications, with respect to their corrosion behavior. In all cases, HV-electrodes made of an austenitic, acid resistant Cr-Ni-steel alloy (AISI 316Ti / 1.4571: Cr 16.5-18.5%, Ni 10.5-13.5%, Mo 2.0-2.5%, Ti 0.7%, Mn < 2%, Si 1%, with minor shares of P, S and C) were used due to its known, good resilience e.g. to chlorine ions. As electrolytes we used ascorbic acid (due to its occurrence in numerous food juices and pastes, etc. processed in food industry) and a sodium chloride (NaCl) electrolyte, for the aggressive corrosion behavior of chlorine ions to many materials, demonstrated, last but not least on material in the marine environment). The electrical parameters were $W_{process}$ = 150kJ/kg, $E_{process}$ = 40kV/cm, f_{rep} =3Hz. Flow rate of the respective electrolyte was 360mL/h. Processing time was two hours or three hours respectively for each experiment. In Fig. 2.1.9,

surfaces of two electrodes, made of the described austenitic steel, are illustrated, after being processed with different electrolytes, for different treatment periods. As reference, an untreated electrode is shown on the left side in Fig. 2.1.9
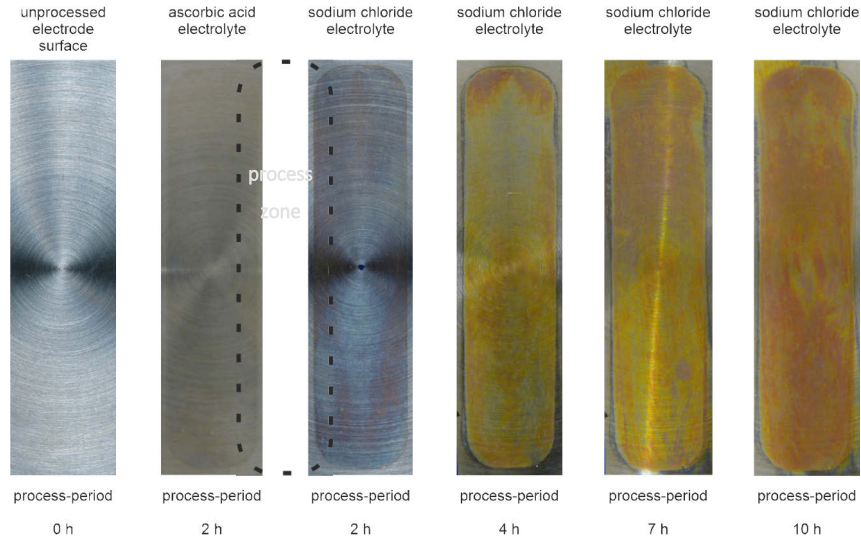
Fig. 2.1.9:   Austenitic steel electrodes processed with different electrolytes at different processing periods.

Discolorations on the electrode surfaces, caused by corrosion procedures during PEF-treatment, clearly indicate size and bounraries of the process zones. In the course of the treatment and the coupled corrosion mechanisms across the surface, material is removed. Mass losses and mass loss-rates during the conducted investigations where determined with appropriate analysis scales and are illustrated in Fig. 2.1.10. Corrosion intensity, where ascorbic acid-based electrolyte was applied, was much lower, compared to corrosion experiments, where sodium chloride electrolyte was used, Fig. 2.1.10.
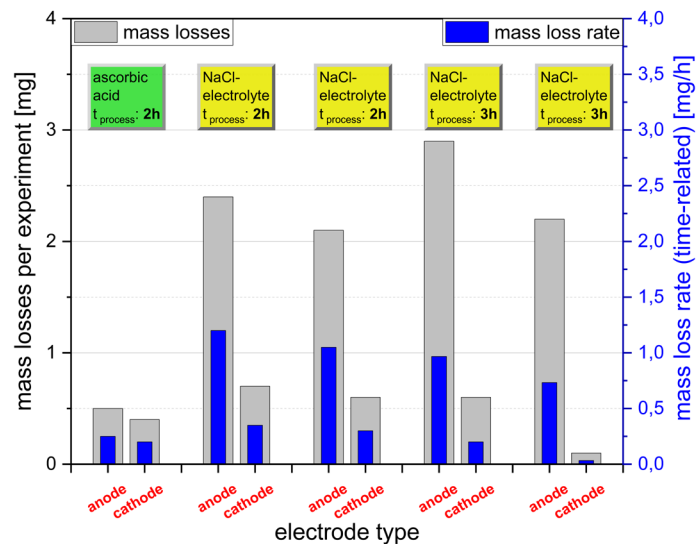
Fig. 2.1.10:   Electrode erosion for different electrolytes and processing periods.

The electrodes, employed with PEF-asisted corrosion experiments, together with sodium chloride electrolytes showed significant higher mass losses and loss rates than the electrodes stressed with ascorbic

acid electrolyte. The electrode-couple, treated with sodium chloride electrolyte was processed for a total period of 10 hours in the end, in time intervals of 2h / 2h / 3h and 3h. The mass losses and the mass loss rates as well decrease with continuous experiments, regardless of the length of the processing periods (2h / 3h). Mass losses of the cathodes are considerably lower in all experiments compared to the anodes mass losses. This observation is more pronounced with the sodium chloride electrolyte-based experiments in comparison to those electrodes, treated with ascorbic acid electrolyte.

| electrolyte	untreated	ascorbic acid	sodium chloride	sodium chloride
processing period	0	2h	2h	10h
S q [μm]	15.7	15,7	15.4	16.0

Table 2: Impact of different processing electrolytes and processing periods during PEF-treatment on electrode surface quality, described by S_q, the standard deviation of the height distribution, or RMS (Root-Mean-Square surface) roughness.

For evaluation of the surface quality, topographies of the considered electrodes were determined by means of a contactless laser assisted measuring system and characterized by the parameter S_q. S_q computes the standard deviation for the amplitudes of the surface root mean square (RMS). The S_q - values remain almost constant, regardless of the applied electrolyte, electrode type (anode/cathode) as well as with the surface of the untreated reference electrode, Table 2

Considering electrode material losses during PEF processing of NaCl-electrolytes, using stainless steel electrodes (AISI 316Ti, comprising the heavy metals iron, chromium, nickel, molybdenum and manganese), it needs to be clarified, where the lost material has gone. For that purpose, the liquid processed NaCl-electrolytes were analyzed with ion chromatographic- and optical emission spectrographic methods. The results of these analyzes are shown in Fig. 2.1.11. No iron-, chromium- and molybdenum-ions could be found in the investigated electrolytes. Thereby, it must be considered that the lower sensitivity limit of measurement, regarding potential ions in the processed electrolytes, was $conc_{detect} \geq 0.01$ mg/L. Only the concentrations of nickel-ions exceeded the limits of approved values for human consumption of nickel-contaminated food ($conc_{Ni\text{-}food, max} \leq 0.14$mg/L, substantially; ´European council-resolution CM/Res (2013)/9- metals and alloys used in food contact materials and acticals´. Allowed nickel-values in drinking water are significantly lower ($conc_{Ni\text{-}drinking\ water, max} \leq 0.02$ mg/L); values published in the german ´drinking water ordinance´. Concentration of metal-ions in the processed electrolytes remained at almost identical levels ($conc_{Ni} \sim 0.27$ mg/L), notwithstanding the different process durations of 2h and 3h, respectively (dotted line in Fig. 2.1.11).

The determined amount of mass losses, obtained by weighing the used electrodes, before and after PEF-treatment, are not reflected in the quantity of found ions in the liquid electrolytes. For that reason, it must be assumed that the missing material is located in small flakes, distributed in the processed electrolytes, which appeared to be organic contaminations, initially.

Specific composition of presumed particles, included in the observed flakes of the collected, processed electrolyte, must be examined. For that purpose, it is necessary to remove organic components. Electrolytes need to be rinsed, to remove remaining NaCl and subsequently evaporated to obtain a concentrate of the present metal particles. Composition of those particles can be quantitatively determined in the scanning electron microscope (SEM) by means of energy dispersive X-ray analysis (EDAX), then.
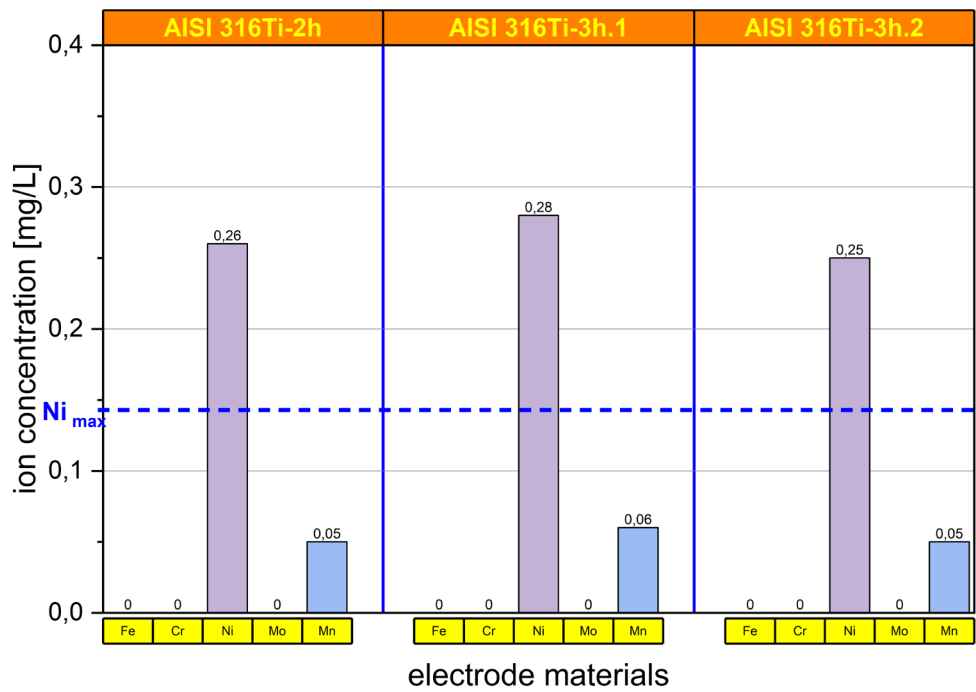
Fig. 2.1.11: Metal-ions found in PEF-processed NaCl-electrolyte, after 2h- and 3h-PEF-treatment, respectevely, using stainless steel-electrodes (AISI 316Ti). The dotted line represents the limits of approved maximum nickel-concentrations for human consumption of nickel-contaminated food (conc $_{Ni\text{-food, max}}$ ≤ 0.14mg/L).

2.2 Components and Electroporation Processes

Contact: PD Dr. Martin Sack

2.2.1. GaN-HEMT in gate-boosted operation

Commercially off-the-shelf available GaN-HEMTs are available for a maximum drain-source voltage of approximately 650 V and exhibit rise times in the order of 3 ns according to the data sheets. In order to invesigate the switching behaviour of a GaN-HEMT in gate-boosted operation, a test circuit according to Fig. 2.2.1 has been set up. The circuit features capacitive gate boosting operation and comprises a three-stage Marx configuration to generate a fast-rising driving voltage. Bipolar transistors operated in avalanche mode serve as closing switches of the Marx generator. The first stage of the Marx generator is triggered by applying an extra voltage to its switch causing its avalanche breakdown. The trigger signal is applied to the circuit at TTL level. Logic inverters serve as driver for an additional bipolar transistor operated in avalanche mode, which serves as closing switch for the generation of the extra voltage to trigger the Marx generator.

For the measurement of the voltages at the GaN-HEMT's gate and the drain versus ground potential the circuit features two resistive dividers of appropriate ratio. Thereby, the divider for measuring the voltage at the drain is coupled via a capacitor to measure the AC component only. The dividers are connected via 50-Ohm cables to an oscilloscope, which match to the characteristic impedance of the measurement system.

For the tests the GaN-HEMT has been operated as closing switch. A Blumlein configuration has been used as load. It has been arranged in two different configurations with cables having characteristic impedances of 50 Ohm and 16.6 Ohm. Additionally, the voltage across the load of the Blumlein configuration has been measured.
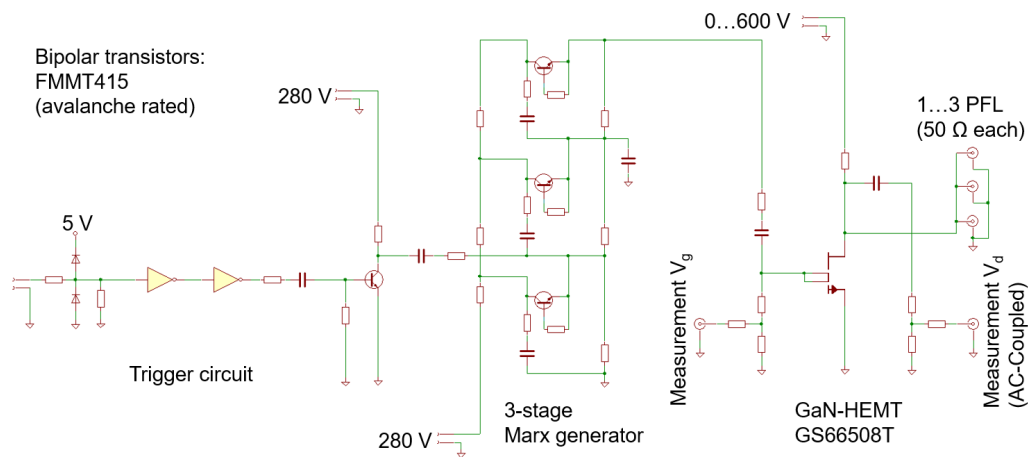
Fig. 2.2.1:   Gate-boosting circuit for a GaN-HEMT with a 3-stage Marx generator.

Fig. 2.2.1 shows the voltages at the gate (V_g) and the drain (V_d) versus ground potential with the switch being connected to a parallel configuration of three 50-Ohm cables acting as resistive load of 16.6 Ohm. For the measurements the voltage at the drain has been increased stepwise from 100 V to 600 V in steps of 100 V. A risetime of the voltage of 0.7 ns (10% -> 90%) at a charging voltage of 600 V has been achieved. Fig. 2.2.3 and Fig. 2.2.4 show measurements for the Blumlein configuration set up with cables having a

characteristic impedance of 16.6 ohm. Voltages at the gate, the drain, and the resistive load at the output of the Blumlein configuration of 33.2 ohm versus ground potential are shown. The voltages at the drain and the load exhibit rise times of 0.7 ns and 0.8 ns, respectively. Measurements with cables having a characteristic impedance of 50 ohm showed similar results with slightly faster rise time. The Blumlein configuration (Z_C = 16.6 ohm) has been operated for 6.25 hours at a charging voltage of 600 V and a pulse repetition rate of 1.4 Hz resulting in approximately 33000 pulses. Fig. 2.2.5 shows a superposition of measured voltages at the gate, the drain, and the resistive load of the Blumlein configuration versus ground potential. First and last pulse together with four randomly selected additional pulse shapes are displayed. The pulse shapes exhibit no substantial deviations.
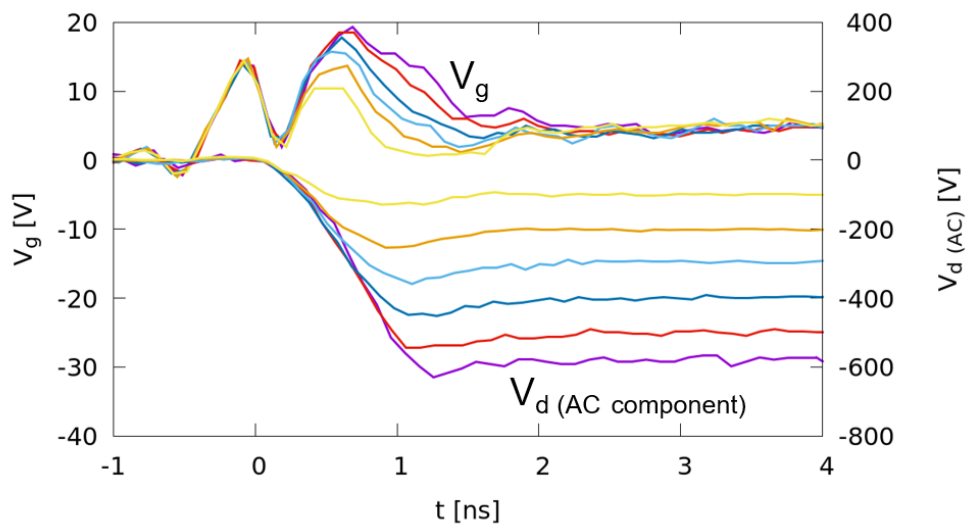

Fig. 2.2.2:   Voltages at gate (V_g) and drain (V_d) versus ground potential connected to a parallel configuration of three 50-ohm cables acting as resistive load of 16.6 ohm.
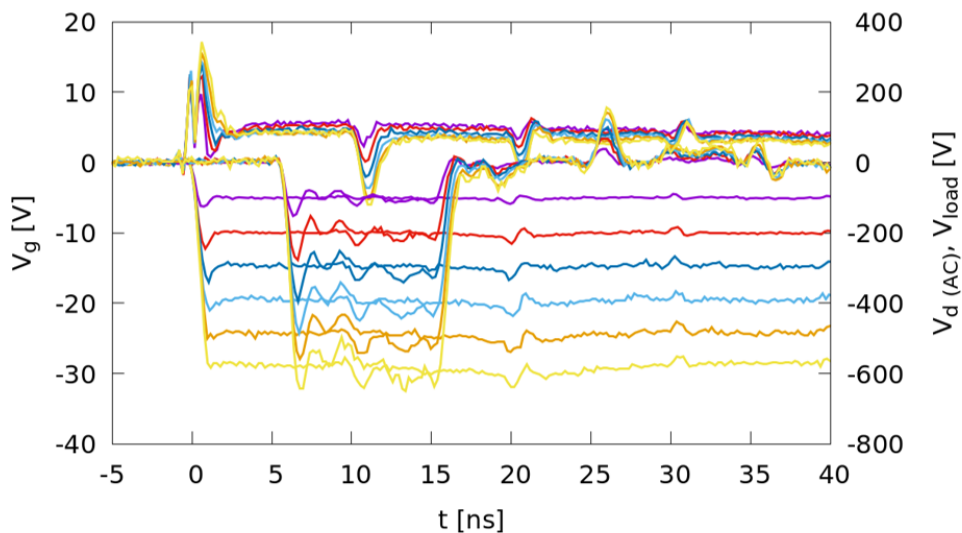
Fig. 2.2.2:   Blumlein configuration: Voltages at gate (V_g), drain (V_d), and resistive load versus ground potential (resistive load: 33.2 ohm).
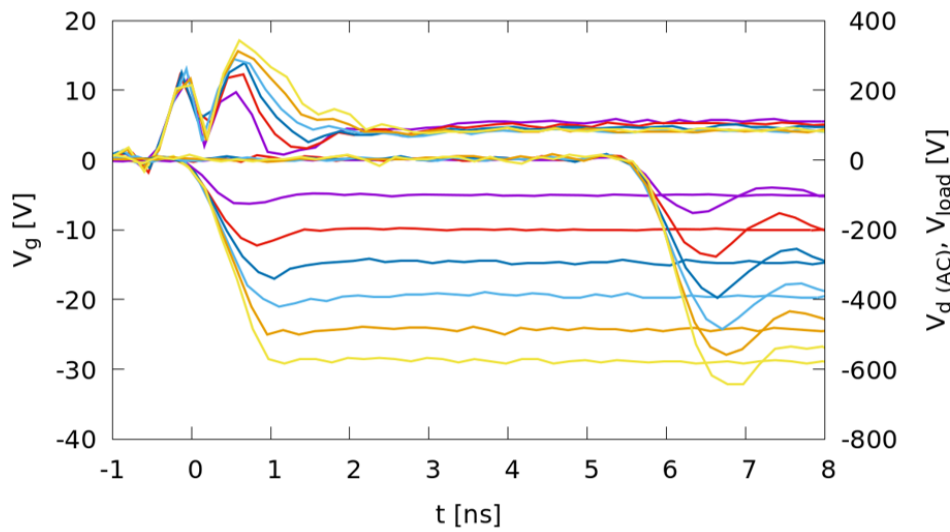
Fig. 2.2.3: Blumlein configuration (detail): Voltages at gate (V_g), drain (V_d), and resistive load versus ground potential (resistive load: 33.2 ohm).
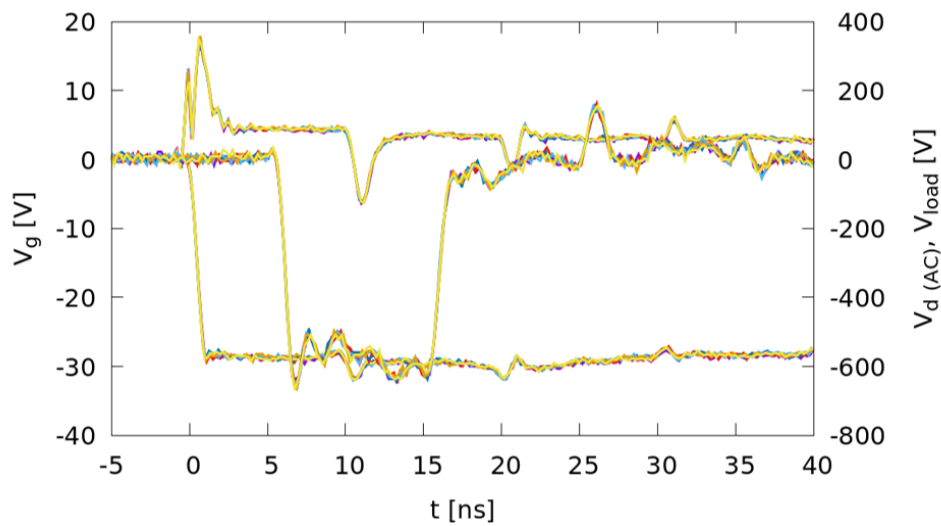
Fig. 2.2.4: Blumlein configuration: Superposition of measured voltages at gate (V_g), drain (V_d), and resistive load (33.2 ohm) versus ground potential in the course of an operation for 6.25 hours at 1.4 Hz pulse repetition rate. First and last pulse together with four randomly selected additional pulse shapes are displayed.

A setup comprising two closing switches with one closing switch at the end of each transmission line of the Blumlein configuration allows for a control of the pulse length and the polarity of the pulse. Thereby, the range of the pulse length is limited by twice the signal travelling time along each of the two lines of the Blumlein configuration. Fig. 2.2.6 shows such a configuration. Each switch comprises one GaN-HEMT in gate-boosted operation. For the experiments the desired delay between both switches has been adjusted by means of RC circuits. The Blumlein line has been set up using three paralleled 50 ohm cables per tranmission line resulting in a total characteristic impedance of 16.6 ohm.

Fig. 2.2.7 shows the output voltage of the Blumlein configuration for a charging voltage of 100 V, measured at a matched resistive load. Different delay times were selected between the closing of the switches in the

range between -5 ns and 5 ns, staggered with a step width of approximately 1 ns. An enlarged view of the curves in Fig. 2.1.8 shows rise and fall times of significantly less than 1 ns.
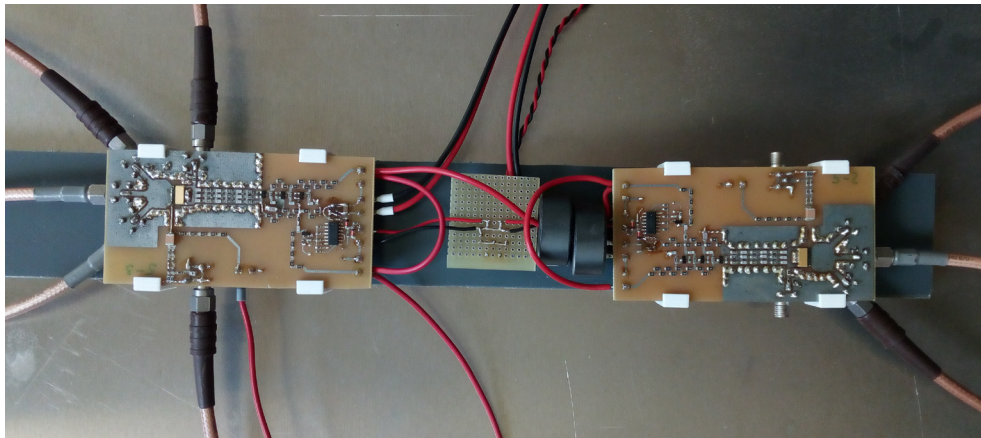
Fig. 2.2.5:   Blumlein configuration with two closing switches.
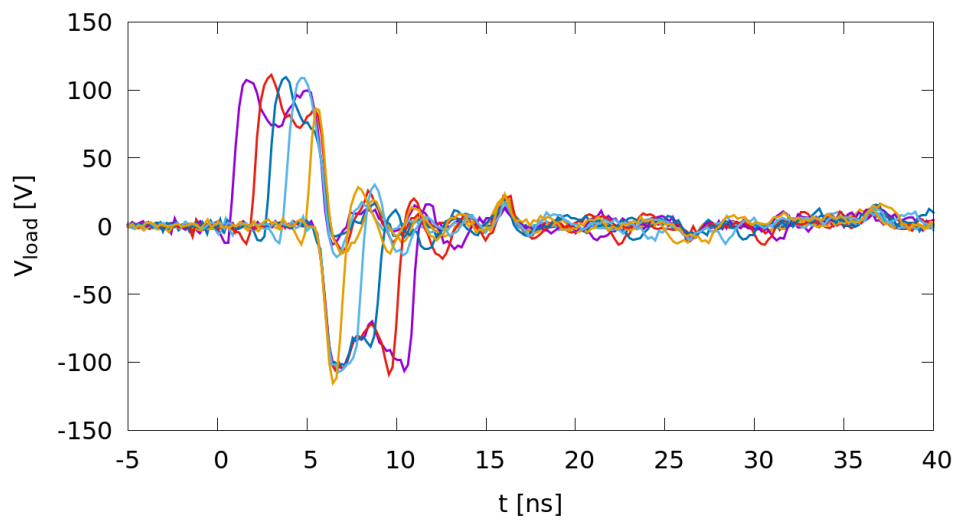
Fig. 2.2.6:   Variation of the delay time between closing of the switches: Voltages at the resistive load versus ground potential.
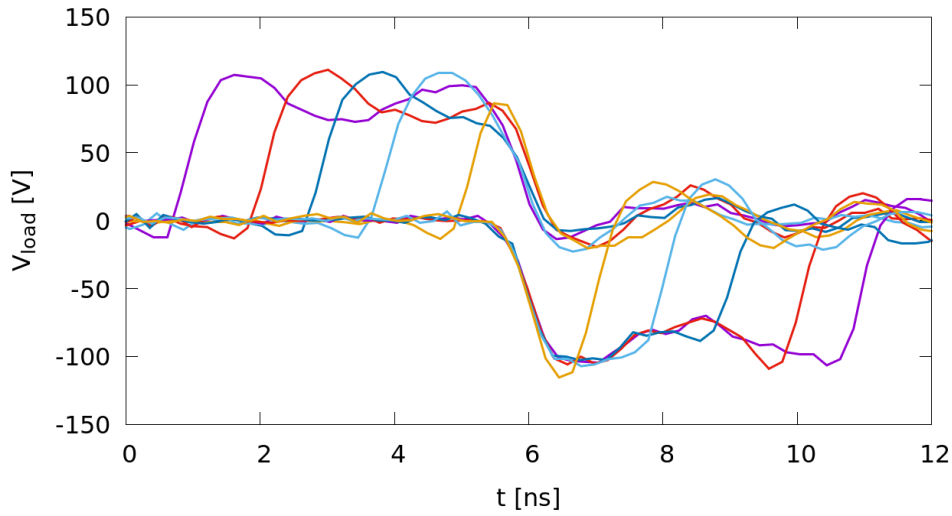
Fig. 2.2.7:   Variation of the delay time between closing of the switches in detail.

2.2.2. Approach towards improved modelling of GaN HEMTs

In the framework of DFG-funded research project which is conducted in close cooperation between the KIT institutes IHM and ETI, the description of dispersive effecs in commercially available GaN HEMTs like charge carrier trapping and temperature effects is being investigated based on S-parameter measurements and time-domain measurements. The research activities at IHM deal with the setup and operation of an advanced arrangement for S-parameter measurements under pulsed operating conditions of the device under test and the parameter extraction for modelling. It is the goal of the project to set up behavioural models of selected GaN HEMT devices, which may serve in future for circuit simulations at advanced precision compared to the currently commercially available models. Current work on the project comprises an evaluation of the algorithms for the setup of small-signal equivalent circuits based on the S-parameter measurements and time-domain measurements, and the description of the large-signal behaviour, both comprising a model for the description of charge carrier trapping effects Fig. 2.2.9 shows a comparison of simulated S-parameters for a small-signal and a large-signal model with the exemplarily original data at a selected operating point. Original and processed data are in very good agreement.
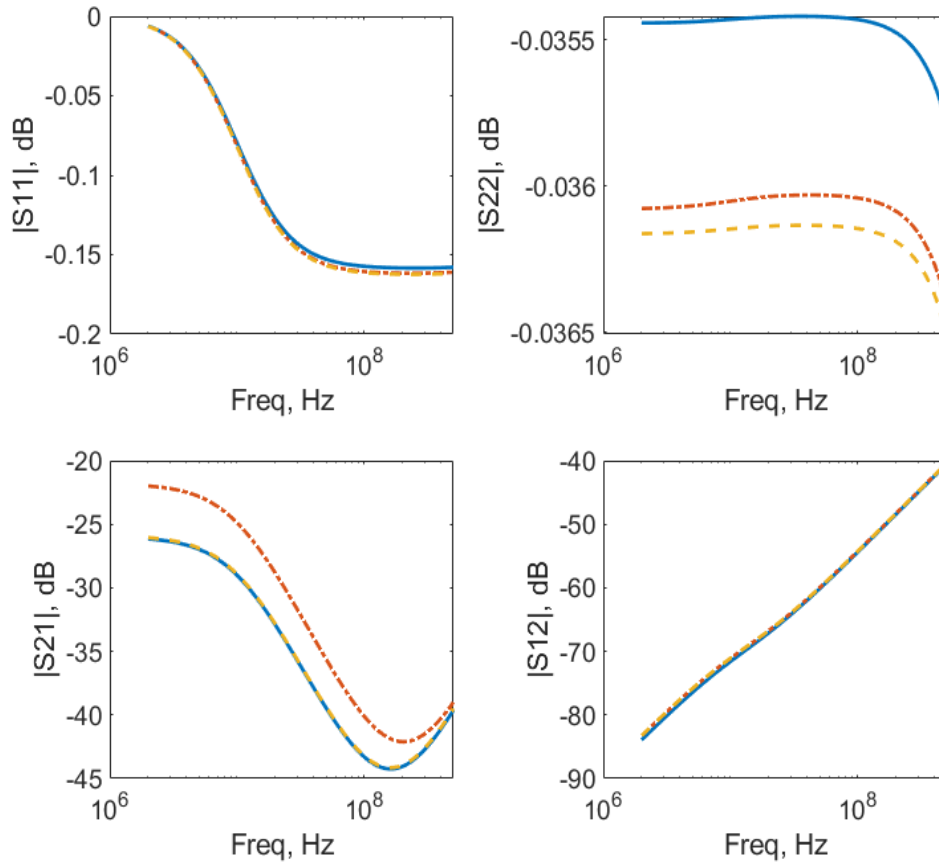
Comparison of simulated S-parameters for a small-signal and a large-signal model with the exemplarily original data

at an operating point $U_{gs} = 2V$, $U_{ds} = 20\,V$.

Fig. 2.2.8: Example for the algorithm evaluation: Comparison of original and processed data.

A streamlined method to model GaN high electron mobility transistor's (HEMT) behaviour based on I-V measurements is currently under investigation. An Angelov-based model is used to this end, modified to account for the device's off-tail of the transconductance function and the steeper output conductance behaviour in the ohmic regime, as well as the effects of self-heating. The resulting model features an equation for the equivalent circuit's current source with its numerical parameters obtained from the step-wise fitting of the measurement data (Fig. 2.1.10). The fitting helps modelling the current-voltage dependency of a GaN HEMT in the cases when the input dataset provides insufficient number of points to assess all critical parameters of the Angelov model using standard techniques.
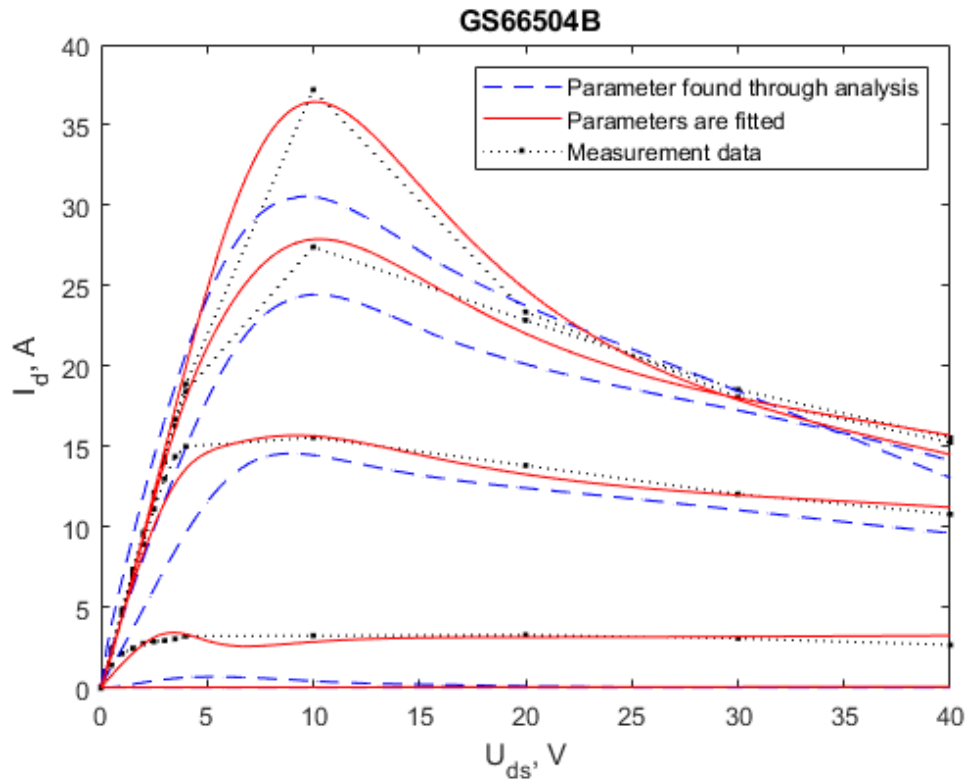
GS66504B

Fig. 2.2.9: Comparison of the I_{ds} characteristics shown for the gate bias between 1 and 5 V. Black dots represent the measured data; blue dashed curves represent its simulation using the Angelov model, parameters for which were found from measurement curve analysis; red curves represent the simulation using the Angelov model with parameters found via direct fitting.

2.2.3. Pulse generator for arbitrary waveform generation

In order to enable the generation of voltage pulses with a stepped arbitrary waveform, a pulse generator comprising individual control for each stage is currently under development.

Fig. 2.2.11 shows a photo of one stage. It comprises three H-bridge modules equipped with SiC MOSFETs and pulse capacitors. The pulse capacitors are charged via a chaging circuit controlling the charging voltage for the stage. Thereby, the charging voltage $V_{ch,i}$ can be selected individually for each stage up to a maximum voltage of 800 V. Each stage is powered by a local power supply which is coupled via a transformer to an AC current source providing the power for all stages at a frequency of approximately 100 kHz. Each stage is equipped with a local control unit which is connected to the main control unit of the generator via a bi-directional fiber-optic link. During pulse generation, the local control units control the operation of the H-bridges such that the bridges deliver an output voltage which is either zero or plus or minus $V_{ch,i}$. The stages will be connected in series, so the total output voltage of the generator will be the sum of the individual stage voltages. For the generation of a stepped arbitrary waveform, well before the pulse generation the individual switching pattern for each stage is stored to its local control unit. During pulse generation the main control unit generates a clock signal, which is distributed simultaneously to all stages.It serves as a time reference for a synchronized operation of all stages.

For the generation of well-defined voltage pulses it is of interest to study the generation of a precise voltage across a matched load. However, accross a semiconductor switch a voltage drop occurs depending on the

current. When connecting the generator to a matched load with a known and constant load impedance, for example 50 ohms, the ratio of voltage and current at the load is therefore known and enables a compensation of the voltage drops, especially of the voltage across the temperature-dependent internal impedance of each individual semiconductor switch (i.e. for a MOSFET the value $R_{DS,on}$) in the following ways:

a) the individual stage voltage U_{0m} of each module m is adjusted such that the absolute value of the module's output voltage stays within a predefined tolerance band when considering the voltage drops across the impedances $R_{DS,on}$ of the module's conducting MOSFET switches and the due to the discharging or charging process varying voltage of the module's capacitor. If the pulse repetition rate is sufficiently low, e.g. 10 Hz, the semiconductor switches have time to cool down significantly, so that the internal impedance (e.g. $R_{DS,on}$) is lower than after a longer period of time while conducting a significantly high current. If the capacitor of one module is discharged during pulse generation, both effects are superimposed and the module's output voltage drops accordingly with the time.

b) The pulse generator's output voltage is measured, e.g. by means of a voltage divider coupled to an oscilloscope and compared to the sum of voltages of the capacitors of all active modules, i.e. modules delivering a voltage different from zero in any individual step. Thereby, all voltages are acquired in the same moment of time. If only one module is active during the measurement, the voltage drop can be calculated as difference between the voltage across the active module's capacitor and the output voltage. If more than one module is active, the individual voltage drops can be calculated based on m measurements, if m is the total number of active modules in a series of i steps. The voltage drops at each individual module can be calculated by solving a linear equation system, provided, that the combination of active modules in the course of the m measurements is linearly independent in the mathematical sense. If the individual voltage drops of each module are known, the modules' charging voltages U_{0i} can be adjusted to compensate for the voltage drop and, hence, adapt the modules to varying environmental conditions, e.g. varying ambient temperature.

During signal transmission via fibre optic cables from the generator's main control unit to the individual generator modules differences in the individual propagation delay times occur due to different lengths of the fibre optic cables or unequal and time-variable attenuation of the light signal, e.g. due to bending of the fibre optic cables. These differences in propagation delay times are equalized by adding an adjustable delay module into each signal path, either as part of the main control unit or preferably as part of each individual stage module, which can be adjusted individually for each stage module to compensate for unequal delay times. This is done on the basis of individual measurements of the switching times of individual stage modules by determining the individual time difference between the generation of the switching signal in the main control unit and the change in the measured output voltage for each stage module. This works particularly well if only one or a few stages are active in a switching step. By comparing the measured delay times at different steps and configurations of active modules, the delay times for each stage module can be calculated, provided that the combinations of active modules is selected appropriately, i.e. allows for the solution of a linear equation system. For this evaluation the same measurement setup for the output voltage can be employed as for checking the voltage amplitude as described above. In addition to or as an alternative to determining the switching times during pulse generation, the switching times can also be determined before pulse generation or between two pulses by switching the stage modules individually or in groups especially for such measurements, either one time for calibration purpose or repeatedly in order to adapt the delays to changing conditions. Moreover, an over-all delay of the pulse at the generator's output versus the generator's input signal can be performed by means of adding an appropriate offset value to all delay modules.

Currently, the initial tests with the setup are performed. The diagram in Fig. 2.2.12 shows voltage and current at the output of one H-bridge connected to a resistive load. The pulse shape has an arbitrarily selected pattern. The magnified view on Fig. 2.2.13 shows a rise time (10% to 90%) for both voltage and current of approximately 20 ns.
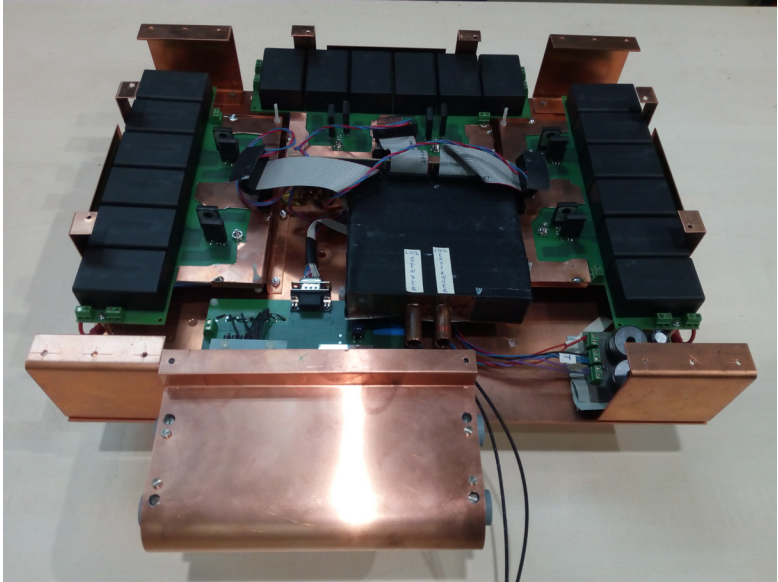
Fig. 2.2.10   Experimental setup of one stage of the pulse generator for arbitrary waveform generation.
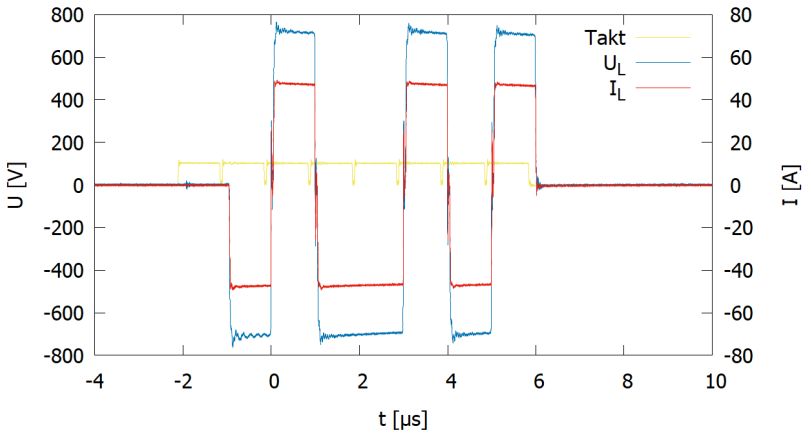

Fig. 2.2.11   Voltage and current at the output of one H bridge connected to a resistive load, together with the clock signal provided by the main control unit.
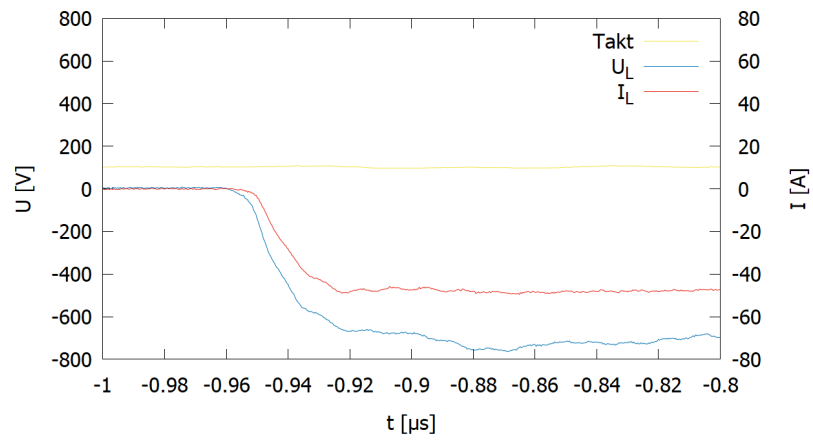
Fig. 2.2.12   Voltage and current at the output of one H bridge connected to a resistive load, together with the clock signal provided by the main control unit: magnified view.

2.3 Concentrating solar power (CSP) and high temperature thermal storage / liquid metal – material compatibility

Contact: Dr. Alfons Weisenburger

Liquid metals, used for example as advanced heat-transfer (HTM) and storage media for CSP and other high-temperature technologies, can make an important contribution to low-carbon energy production and storage. Within LIMCKA (Liquid Metal Competence Center KArlsruhe) several institutes and laboratories of the KIT combine their many years of experience and specific expertise in material research, system engineering, safety and thermal-hydraulics to tackle the relevant aspects of liquid metals. The IHM focuses on compatibility research through surface optimisation of existing materials using GESA and the development of new materials, both of which are able to mitigate corrosion in contact with liquid metals and salts. To realize a high-temperature thermal storage with liquid metals, filler materials that are compatible and inexpensive are required in addition. Liquid metal batteries are a further research area where the expertise of the IHM was combined with the expertise of the DLR and a Chinese university (HUST) to explore Sb-Bi(Sn)/ Na based low cost liquid metal battery concepts in the frame of a German-Chinese DFG project that was successfully finalized in this reporting period. In the BMWK-funded LIMELISA project, which is being coordinated by KSB, ITES, DLR and KSB are jointly investigating materials for valves and pumps for high-temperature heat storages based on liquid Pb and molten salts. In this project the IHM investigates the compatibility of materials in Pb up to 700°C and proposes potential candidates for the manufacturing of pumps and valves to be used in such conditions.

Some of the tasks are embedded in European projects, the EERA-CSP and cooperations like with DLR and HUST via the DFG or with KSB and DLR via the BMWK.

The most relevant results obtained in the reporting period are presented briefly:

2.3.1 CSP – experimental set-up transient heat loads

The experimental setup to investigate material compatibility during transient heat loads in a CSP sodium receiver was finally assembled and taken into operation in the frame of a Bachelorthesis. Previous simulations have shown that the diameter of the induction coil needs to be reduced to fit a 12 mm diameter tube used as a test section to get closer to the required energy density. The segment that was exposed to the first high temperature thermal cycles was a section of a tube with a diameter of 12mm and a length of about 4cm made from 316Ti. The influence of parameters like generator voltage and frequency as well as the orientation of the test piece with respect to the inductor coil were simulated using COMSOL Multiphysics. According to these simulations, the first tube was equipped with three thermocouples to measure the outside tube temperature before, in the middle, and after the area that is located within the inductor coil. The sodium flowed with constant velocity of about 0.04l/s and reached a temperature of 380°C before the test section. The two thermocouples at the in and outlet were rigidly and tightly connected while the one in the middle was fixed by a wire only.
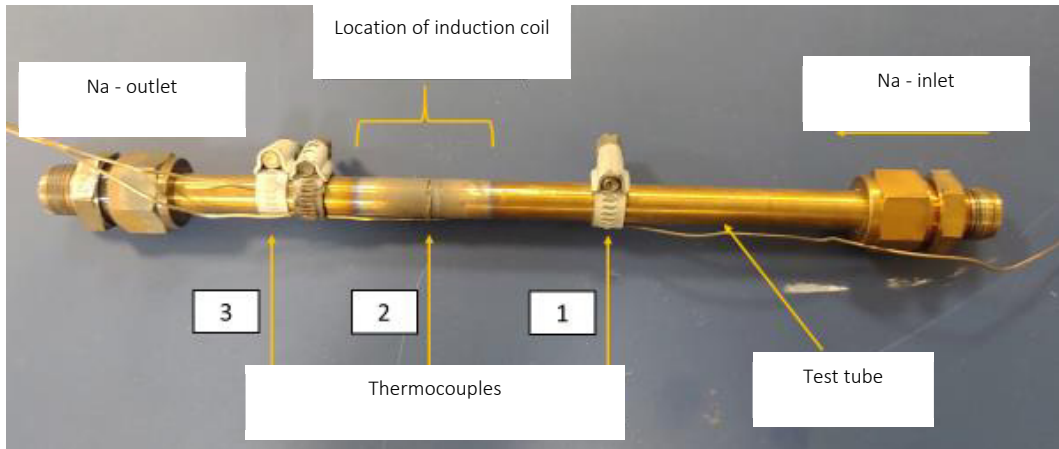
Fig. 2.3.1:   Test section of thermal cycling test

Thermocouple 2 measured a variation between 380°C and 720°C as foreseen at the location of the induction coil. However, these values seem to reflect more the temperature of the fixing wire than the tube surface temperature. The temperature at the outlet of the test-section increased from 380 to 450°C, which is close to the expected values considering the applied induction energy.

The change in microstructure and hardness of the tube test section was evaluated. The hardess decreased from HV 156 to 135 while the grain size was mainly unaffected.
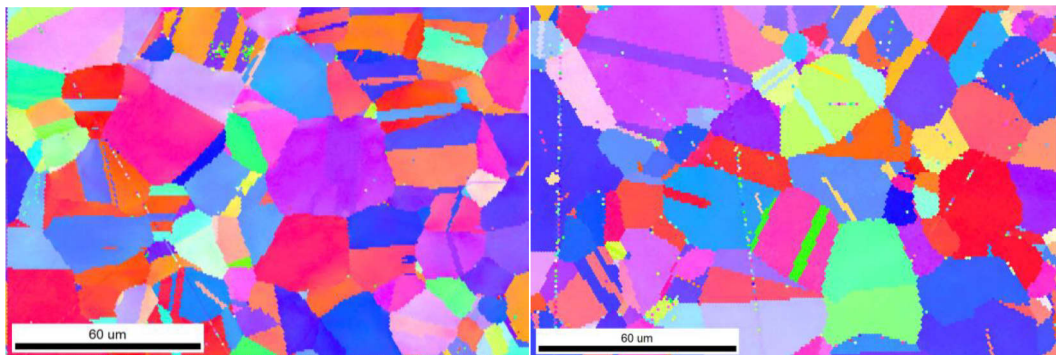
Fig. 2.3.2:   Grain size distribution of 316 tube section measured by EBSD before (left) and after (right) the thermo cycle test

Further tests with varying flow rate and heating loads and especially long-term cycling tests with more than 100 cycles are planned.

2.3.2   Material development

Packed-bed thermal energy storage (PBTES) systems are a promising alternative for cost intensive two-tank molten salt systems that er used in most commercial CSP plants. For high temperature (>500°C) thermal energy storage, liquid metals have great potential as heat transfer media due to their chemical stability and their wide fluid temperature range. Selected filler materials with promising physical and thermophysical properties have been exposed in lead-bismuth eutectic (LBE) at 500°C with a maximum oxygen content of 1×10^{-17}wt% oxygen for 1 and 4 weeks. Both of the glass materials (diamond beads and borosilicate glass

beads) show signs of surface corrosion and chipping. In particular, Na, Mg and Ca appear to be leached from the glass network. In the case of the two ceramics, steatite and alumina (90%), their more or less poor behaviour can also be attributed to the presence of a glassy phase. Zirconia and zirconia silicate showed good behaviour in LBE. In a second phase, 7 different ceramics were tested at 650 and 750°C in lead (Pb) up to 5000h with a reducing atmosphere above. The findings suggest that neither temperature nor time dependency plays a significant role in the observed attack on the beads. As observed in the initial tests, the glass content is of greater significance. The penetration depth of Pb is frequently depending on surface defects. Pre-existing fissures and cracks provide preferable penetration paths for Pb, thereby facilitating deeper penetration. The Y-stabilised ZrO_2 (YTZ) and the zirconia toughened Al_2O_3 (Minerax) ceramics show the most favourable behaviour, with only a negligible reaction with Pb. The two alumina ceramics (90% and 92%) and the zirconium silicate RIMAX exhibited a slightly inferior behaviour, as shown in Fig. 2.3.3. The zirconium silicate ER120 and the Ce-stabilised ZrO2 are both unsuitable for use due to their high glass phase content. which results in the associated Pb attack. In addition, the thermal shock resistance plays a more important role at the envisaged high temperature gradients envisaged. Consequently, the next step will be to test the materials that have performed well under isothermal conditions under frequent thermal cycling. A test facility is being set up for this purpose.

Fig. 2.3.3 :   Alumina 92%: cross section of the original material (left), samples after 1000h at 750°C in Pb (middle) and

The valves and pumps that are investigated in the LIMELISA project require abrasion resistant materials such as stellites. The Co-alloy Stellite 6 shows corrosion attack after 2000h and 5000h exposure to molten nitride salt at 600°C, while an oxide scale seems to protect the material at 700°C. In order to minimise damage during service at 600°C, it was suggested to grow an oxide scale by pre-oxidising the alloy prior to any contact with the molten salt. Pre-oxidation was carried out at 700°C and 800°C for different durations and oxygen contents. Only at 700°C in normal air and for 160 hours a 1μm thick stable Cr oxide layer is formed.

The second investigation focused on whether nitriding or diffusion of nitrogen into the material leads to material embrittlement. Hardness profiles were taken on materials such as Antinit Dur 300, SLM 316L dark and white, which had been aged in solar salt and where nitriding had been detected. They showed no increase in hardness near the surface. In fact, the hardness values decreased slightly but were still in the lower limit range, probably due to the reduction in Cr caused by spinel formation. A slight increase in hardness near the surface was observed when the indenter hit a hard phase, namely Cr-rich nitrides. It should be noted that the annealed SLM 316 dark has coarser Cr nitrides at the grain boundaries compared to the unannealed 316L white

Cr-Oxidschicht

Stellite 6

Stellite 6_voroxidiert_700°C_160h (3001x)   ⊢— 9 µm —⊣

a.

Cr-Reduzierung   Härteverlauf Antinit DUR 300
nach 5000 h Auslagerung (Solarsalz)

b.   Abstand von der Oberfläche [µm]

HV 0,05
HV 0,01

Cr-Reduzierung Härteverlauf SLM 316L dark, white (Solarsalz)

c.   Abstand von der Oberfläche [µm]

316L dark, 5000h
316L dark, 1000h
316L white, 5000h

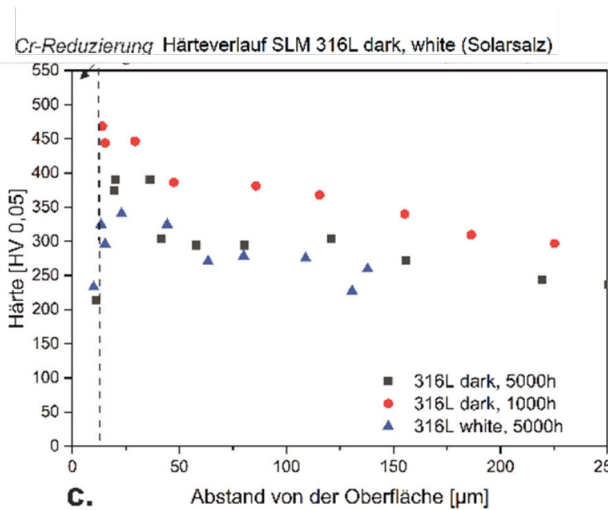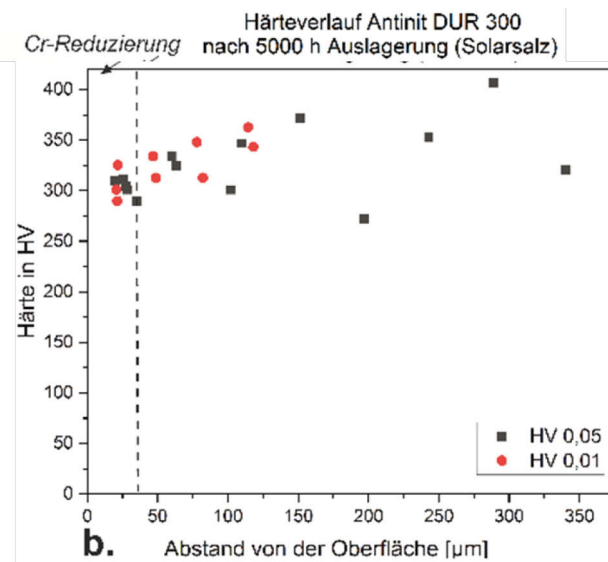Fig. 2.3.4:   a). Stellite 6 after 160-h pre-oxidation in normal air at 700°C b). Hardness values below the oxide scale measured at Antiit DUR 300 after der 5000-h exposure in solar salt c). Hardness values at SLM 316L dark and SLM316L white.

63

2.3.3 Liquid metal battery

Liquid metal batteries (LMBs) offer a cost-effective technology for grid-scale stationary energy storage. They are characterized by rapid kinetics, easy scalability, and long service life. Our institute concentrates its research activities on Na-based LMBs due their economic and environmental advantages over other negative electrode materials such as lithium. Main research topics are the material compatibility of the solid cell components with the electrochemically active liquid components and the electrochemical performance of the Na-LMB cells.

The active liquid components of a Na-based LMB cell comprise Na as negative electrode, a molten salt electrolyte, and a heavy liquid metal as positive electrode. The molten salt mixture LiCl-NaCl-KCl (61:3:36 at%) combines good electrochemical performance (high Na^+ conductivity, low Na solubility) with a relatively low melting temperature, which allows to reduce the working temperature to 450 °C. Antimony as positive electrode promises a high cell voltage and high storage density and is typically alloyed with Sn or Bi to reduce its melting temperature.

After static corrosion tests of various candidate positive current collector (PCC) materials in both Sb-Sn and Sb-Bi alloys performed in the preceding years, it was decided to proceed with the least aggressive $SbBi_9$ alloy as positive electrode. Excellent electrochemical performance of respective $Na//SbBi_9$ test cells could be demonstrated. In the reporting period, the electrochemical performance of $Na//SbBi_9$ LMB cells was further investigated. The influence of various design parameters on the cell performance could be quantified and important parameters such as the ohmic resistance of the electrolyte, contact resistances, self-discharge current, and the cell voltage as function of its state-of-charge could be determined.

Regarding the compatibility of the PCC material with the positive electrode, the corrosion behaviour under operating conditions is of most interest and concern. Static corrosion tests indicated that stainless steel might be suitable as PCC for short-term use, while molybdenum might sustain even long-term application. Therefore, LMB cells with the PCC made of stainless steel and such with Mo were built and their performance under continuous charge-discharge cycling was compared. It was found that the cell capacity decreased in both cells due to evaporation of Na into the cell's free space and subsequent condensation at the colder cover. After 800 h of operation, however, a much faster decrease in cell capacity is observed for the cell using stainless steel as PCC. This accelerated capacity loss is not observed for the cell with Mo as PCC. Post-analysis of the dismantled cells confirmed a much higher corrosion attack of the stainless steel compared with molybdenum.
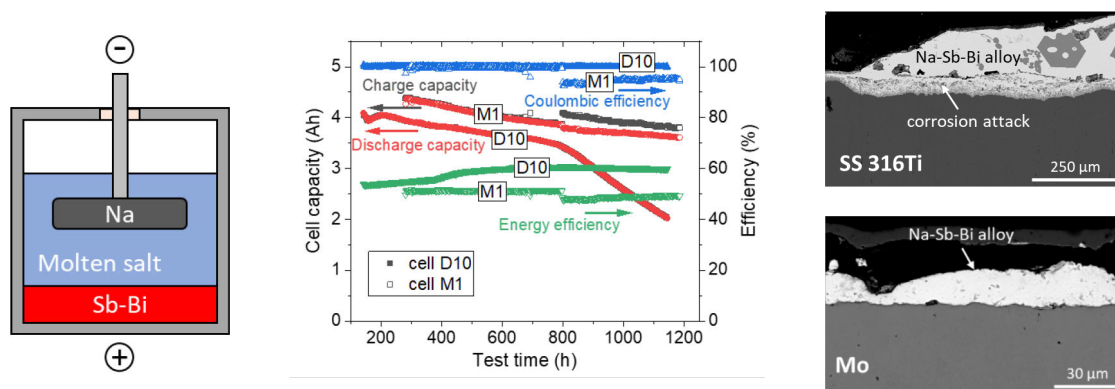

Fig. 2.3.5: Na-based LMB cells. Left: Schematic of cell design. Middle: Electrochemical performance under continuous charge-discharge cycling of Na-LMB cells with the PCC made of stainless steel (cell D10) and Mo PCC (cell M1). Right: Corrosion of PCC material after operation.

Journal Publications

Sack, M.; Herzog, D.; Hochberg, M.; Loisch, G.; Obier, F.; Mueller, G. (2023). Pulse Generator with an Individual Power Supply per Stage. *2023 IEEE Pulsed Power Conference (PPC)*, 1–4, Institute of Electrical and Electronics Engineers (IEEE). doi:10.1109/PPC47928.2023.10311026

Straessner, R.; Nikolausz, M.; Silve, A.; Nazarova, N.; Wuestner, R.; Papachristou, I.; Akaberi, S.; Leber, K.; Mueller, G.; Frey, W. (2023). Holistic exploitation of pulsed electric field (PEF)-treated and lipid extracted microalgae Auxenochlorella prototothecoides, utilizing anaerobic digestion (AD). *Algal Research*, 69, Art._Nr.: 102950. doi:10.1016/j.algal.2022.102950

Onea, A.; Fetzer, R.; Lang, F.; Weisenburger, A.; Hering, W.; Fuchs, J.; Stieglitz, R.; Müller, G. (2023). Thermocycling tests by inductively heated sodium in the high temperature SOLTEC-2 facility. *27th International Conference on Concentrating Solar Power and Chemical Energy Systems: Solar Power and Chemical Energy Systems, SolarPACES 2021*, Article no: 100007, AIP Publishing. doi:10.1063/5.0150350

Yu, R.; Gong, Q.; Shi, H.; Chai, Y.; Bonk, A.; Weisenburger, A.; Wang, D.; Müller, G.; Bauer, T.; Ding, W. (2023). Corrosion behavior of Fe-Cr-Ni based alloys exposed to molten $MgCl_2$-KCl-NaCl salt with over-added Mg corrosion inhibitor. *Frontiers of Chemical Science and Engineering*, 17 (10), 1608–1619. doi:10.1007/s11705-023-2349-1

Niedermeier, K.; Lux, M.; Purwitasari, A.; Weisenburger, A.; Daubner, M.; Müller-Trefzer, F.; Wetzel, T. (2023). Design of the LIMELIGHT Test Rig for Component Testing for High-Temperature Thermal Energy Storage with Liquid Metals. *Processes*, 11 (10), Article no: 2975. doi:10.3390/pr11102975

Ardila-Rey, J. A.; De Castro, B. A.; Rozas-Valderrama, R.; Orellana, L.; Boya, C.; Muhammad-Sukki, F.; Mas'ud, A. A. (2023). Variation in the spectral content of UHF PD signals due to the presence of obstacles in the measurement environment. *IEEE Sensors Journal*, 23 (19), 22620–22629. doi:10.1109/JSEN.2023.3306605

Orellana, L.; Ardila-Rey, J.; Avaria, G.; Davis, S. (2023). Danger assessment of the partial discharges temporal evolution on a polluted insulator using UHF measurement and deep learning. *Engineering Applications of Artificial Intelligence*, 124, Art.-Nr.: 106573. doi:10.1016/j.engappai.2023.106573

Ding, W.; Gong, Q.; Liang, S.; Hoffmann, R.; Zhou, H.; Li, H.; Wang, K.; Zhang, T.; Weisenburger, A.; Müller, G.; Bonk, A. (2023). Multi-cationic molten salt electrolyte of high-performance sodium liquid metal battery for grid storage. *Journal of Power Sources*, 553, Article no: 232254. doi:10.1016/j.jpowsour.2022.232254

del Barrio Montañés, A. A.; Senaj, V.; Kramer, T.; Sack, M. (2024). Updates on Impact Ionisation Triggering of Thyristors. Applied Sciences, 14 (10), 4196. doi:10.3390/app14104196

Silve, A.; Nazarova, N.; Wüstner, R.; Straessner, R.; Delso, C.; Frey, W. (2024). Excess of Water Enables Efficient Lipid Extraction from Wet Pulsed-Electric Field-Treated A. prototothecoides Microalgae Using Immiscible Solvents. ACS Sustainable Chemistry & Engineering, 12 (20), 7683–7692. doi:10.1021/acssuschemeng.3c06966

Jonynaite, K.; Stirke, A.; Gerken, H.; Frey, W.; Gusbeth, C. (2024). Influence of growth medium on the species-specific interactions between algae and bacteria. Environmental Microbiology Reports, 16 (4), Article no: e13321. doi:10.1111/1758-2229.13321

Gusbeth, C.; Krolla, P.; Bruchmann, J.; Schwartz, T.; Müller, G.; Frey, W. (2024). Bacterial decontamination of process liquids and paints in E-coating lines by pulsed electric field treatment. Journal of Coatings Technology and Research, 21, 1385–1398. doi:10.1007/s11998-023-00901-4

Gusbeth, C.; Frey, W. (2024). Processing liquid food with hundreds of Hertz and tens of kilovolts Comment on "Advances in pulsed electric stimuli as a physical method for treating liquid foods" by F. Zarea, N. Ghasemi, N. Bansal and H. Hosano. Physics of Life Reviews, 48, 201–202. doi:10.1016/j.plrev.2024.02.001

3 Safety Research for Nuclear Reactors (NUSAFE): Transmutation -Liquid Metal Technology-

Contact: Prof. Dr. G. Müller, Dr. A. Weisenburger

Long-living high-level radioactive waste from existing nuclear power reactors should be transmuted in short-living radio nuclides using fast neutrons provided by a spallation target in an accelerator driven subcritical system or by a fast nuclear reactor. The objective is to reduce the final disposal time of high-level radioactive waste (plutonium, minor actinides) from some 10^6 years down to about 1000 years. Lead (Pb) and lead-bismuth (PbBi) are foreseen as spallation-target and coolant of such devices.

The aim of the institute's contribution is to develop advanced corrosion mitigation processes based on in-situ formation of protective alumina scales especially for parts under high loads like fuel claddings or pump materials in contact with liquid Pb or PbBi. Pulsed large area electron beams (GESA) are used to create aluminum containing surface alloys on steels. In addition, bulk alumina formers like FeCrAl, AFA (alumina forming austenitic steels) and HEA (high entropy alloys) are developed.

All tasks are embedded in European and international projects and cooperations like e.g., ILTROVATORE, ORIENT-NM, INNUMAT, CONNECT-NM and EERA-JPNM.

The most relevant results obtained in the reporting period are presented briefly:

3.1 Material development and advanced corrosion mitigation strategies for heavy liquid metal-cooled nuclear systems

3.1.1 Investigation of GESA facility

The use of the Langmuir probe as an instrument for the measurement of plasma parameters is subject to fundamental problems which significantly limit the applicability of the measurement method to many plasma objects. Whether the positive bias of the probe violates the non-disturbing measurement principle is always an issue. In principle, the disturbed energy balance of the charged particles can spread to the entire plasma volume. Another problem is that the relationship between the plasma parameters and the measured current to the probe must be carefully checked or redefined for each measurement. Thus, the measurement method itself becomes the object of investigation.

Based on the LIF-Dip Diagnostics (An, Zhen, Weisenburger, Mueller Rev. Sci. Instr. DOI:10.1063/5.0064676 Feb. 2022), the „LIF-Dip-Probe" measurement method was developed at IHM. This method can detect a wide spectrum of plasma parameters, with sub-mm spatial and nano-seconds temporal resolutions. In particular, this method closes the diagnostic gap of diluted low-temperature plasmas of pulsed systems.

As with the classical Langmuir probe, the plasma parameters in a LIF-Dip-Probe are measured around a locally immersed conductive probe, where the probe potential for the collection of ions is maintained

(=<floating Potential). The potential difference between the plasma and the probe is equalized by the formation of a positive space charge area (the sheath). Thus, the disturbance due to the probe expands only on the sheath size into the plasma volume (a few Debye lengths). The characteristic of this sheath is largely independent of the properties of the probe (except its potential), representing only the specific parameters from the undisturbed plasma surrounding. In order to know the local plasma parameters, the electric field distribution in the sheath is measured using the LIF-Dip diagnostics. The measurement signal from the LIF-Dip (Fig. 3.1.1) delivers not only the amplitude of the field, but also the geometry of the space charge area.

To obtain the plasma parameters, a simulated curve generated by the numerical solution of the Poisson equation is fitted to the Dip shape. Plasma density, temperature and potential, the fitting parameters, are varied using a special algorithm. The boundary conditions of the Poisson equation include: Bohm criterium, continuity equation, conservation of energy for the ions in the sheath and Boltzmann distribution for the electrons.

As a side effect of the LIF-Dip-Probe, it is possible to use the method as a Mach probe to measure the drift velocity of the plasma. To do this, it is sufficient to compare the sheath characteristic in the up- and down-stream areas.
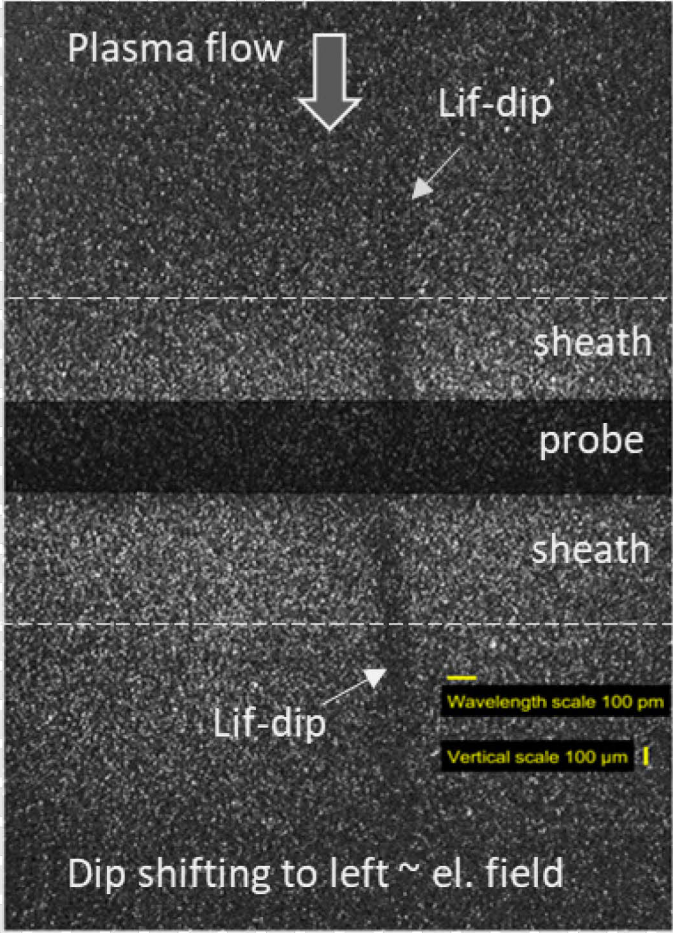

Fig. 3.1.1:   Measurement of Lif-dip delivers the amplitude of the field and the geometry of the space charge area.

3.1.2   Erosion corrosion experiments in the CORELLA facility

The new facility CORELLA-2 for erosion corrosion experiments in liquid lead alloys with controlled oxygen content was finally designed and constructed. Fluid dynamic simulations using COMSOL with varying inner geometries were the basis to construct the entire facility. The specimens are now rotating and the Pb is kept almost stagnant by adding flow inhibiting plates. The relative velocity can reach up to 6m/s at a rotation speed of 400 rpm only. To allow higher experimental temperatures (>550°C) all inner surfaces of the experimental container were aluminized by an external partner. Commissioning of the facility is almost finalized and first tests are in preparation.

3.1.3   Material development to mitigate corrosion

As part of the INNUMAT project three new AFA alloys were developed and finally produced by a partner. The main aim of the development was to obtain phase stable austenitic steels that can be employed at a temperature range above 600°C. Based on the experimental results from the GEMMA project the composition of the AFA alloys were optimized using thermodynamic simulations applying the Thermocalc software. The main criterion for optimization was to minimize the formation of sigma and other embrittling phases in the temperature range above 650°C, while maintaining the austenitic matrix. The addition of V and W should contribute to the formation of precipitates that can improve the mechanical properties at the envisaged temperature range. The amount of Al was kept as low as possible in combination with the Ni and Cr content to prevent the long-term formation of ferritic phases in the alloys.
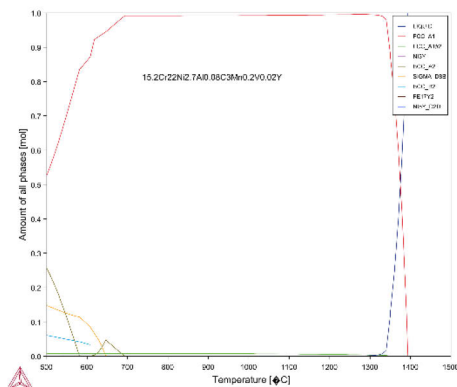
AFA-1: bal.Fe15.2Cr 22Ni 2.7Al 3Mn 0.8Nb 0.2V 0.08C 0.02Y

AFA-2: bal.Fe15.2Cr 24Ni 3.1Al 3Mn 0.8Nb 0.2V 0.08C 0.02Y

AFA-3: bal.Fe14.5Cr 24Ni 3.85Al 3Mn 0.8Nb 1.1W 0.08C 0.02Y

Composition of AFA alloys in weight%

Fig. 3.1.2:   Calculated amount of phases as function of temperature of AFA-A alloy using Thermocalc software.

Based on these simulations, three alloys were manufactured at SWERIM in SWEDEN and hot rolled for delivery to the partners in the INNUMAT project. A final heat treatment at 1150°C was performed to obtain a fully austenitic structure with homogenous grain size distribution, see Fig. 3.1.3. Samples are shipped after final heat treatment to the partners in the INNUMAT project for further studies. Beside tests in liquid Pb the three AFA steels will also be exposed to molten chloride salts. Therefore, pre-oxidation to form an alumina scale at the surface is investigated. At 850°C the formation of a continuous alumina rich oxide scale is observed at the surface.
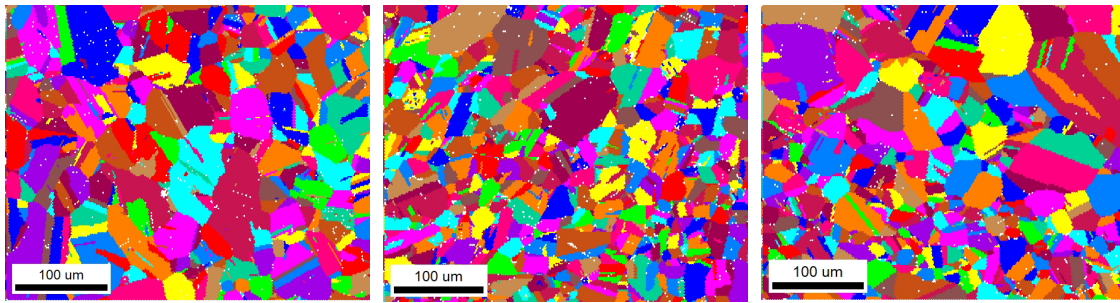
Fig. 3.1.3:   Grain size dirstrubtion of annealed AFA steels. From left: AFA-1, AFA-B and AFA-C

Journal Publications

Heinzel, A.; Fetzer, R.; Lang, F.; Weisenburger, A.; Cataldo, S.; Di Fonzo, F.; Müller, G. (2024). Corrosion tests on austenitic samples with alumina and alumina-forming coatings in oxygen-containing stagnant Pb and turbulently flowing PbBi. Journal of Nuclear Materials, 596, Art.-Nr.: 155121. doi:10.1016/j.jnucmat.2024.155121

Lu, K.; Shi, H.; Weisenburger, A.; Aktaa, J. (2024). Enhanced strength-ductility synergy of a partially recrystallized AlCrFeNi multi-principal element alloy. Materials Characterization, 207, Art.-Nr.: 113578. doi:10.1016/j.matchar.2023.113578

4 Materials and Technologies for the Energy Transition (MTET): Power-based Fuels and Chemicals - Microwave Process Technology -

Contact: Guido Link

Besides the activities on development of technologies and systems for the plasma heating in the FUSION Program, IHM is also in charge of research and development in the Power-based Fuels and Chemicals part of the MTET Program.

The main focus of IHM in this field of research is in plasma chemistry such as CO_2 dissociation or H_2 production by use of atmospheric plasmas sustained by high-power microwaves, generated by innovative solid-state amplifiers. For this purpose, the power of plasma sources has been increased and further efforts were undertaken regarding plasma diagnostic and multi-physics modelling. In the frame of the eXPlore project a container-based infrastructure has be elaborated for the development of a pilot scale plasma base reactor concept for CO2 activation.

The expertise on microwave engineering and the existing industrial scale high-power microwave infrastructure faces growing interest from industry and research. As a consequence, the research group is involved in several national and international joint research projects with objectives in various fields of applications. Further activities investigated microwave assisted additive manufacturing with continuous carbon fiber reinforce thermoplastic filaments in the framework of a Helmholtz Technology Transfer and Validation project MWPrint4ReCon. Within the IraSME project Phased-Array-Antenna for Microwave based Weed Control (PAMiCo) the design antenna has been built an test.

Within the highly multidisciplinary Helmholtz IVF project CORAERO (Airborn Transmission of SARS Coronavirus), which brings together scientists from virus biology, medicine, applied physics, chemistry, and engineering, IHM has design microwave-based applicator concepts for inactivation of coronavirus.

4.1   Plasma chemistry

Contact: Sergey Soldatov

In close collaboration with KIT-IMVT, KIT-IHM actively contributes to the Helmholtz energy research program MTET (Materials and Technologies for the Energy Transition) to address the increasing demand for power-to-X technologies. We investigate the endothermic reduction of CO_2 to CO in atmospheric microwave plasma discharges for its subsequent conversion into valuable chemical precursors and synthetic fuels: $CO_2 \leftrightarrows CO + 1/2 \; O_2$. At atmospheric pressure contrary to vacuum conditions, CO_2 plasma gets contracted that leads to very high plasma temperature (6000 K to 7000 K) resulting in 1) excessive (not required for the process) dissociation $CO \leftrightarrows C + O$ and 2) higher challenges for plasma quenching to avoid back reaction of CO with O. The first problem can be hardly combated and for the second one the special design of afterglow reactor zone is in the focus of our recent study to improve the process efficiency.

A special water-cooled nozzle constructions were designed and installed in the plasma afterglow reactor zone. The nozzle improves both quenching and gas cross mixing. To estimate the temperature and velocity fields in the reactor as well as the heat loads in the materials, multi-physical simulations of the gas flow dynamics coupled with heat transfer were performed. Experimental validation has proven that water-cooled nozzle as compared with no-nozzle configuration improves the CO_2 conversion and energy efficiency by factor of 4 and 3.5 respectively (Fig. 4.1.1).
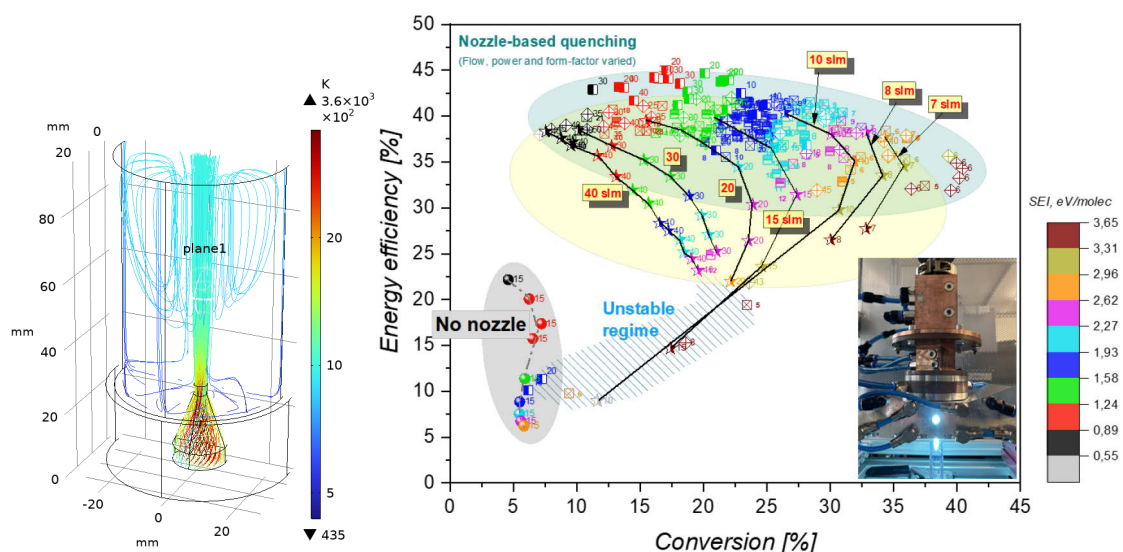

Fig. 4.1.1:   Simulated temperature and gas flow for nozzle configuration (left). Energy efficiency vs. conversion with and without nozzle in the afterglow. Specific energy input (SEI) is color coded. Inlet: photo of experiment (right).

Systematic investigations of pulse modulated microwave power with a high Q self-igniting TM_{010} microwave resonator have demonstrated for the first time specific modulation regimes with non-contracted CO_2 plasma at atmospheric pressure. Time resolved optical emission spectroscopy, which is used to analyze the evolution of plasma temperature demonstrate a large temperature change in the transition region from contracted plasma to diffuse, non-contracted plasma with a significant increase in the efficiency of CO_2 dissociation. This could be a promising approach for future atmospheric plasma-based gas-conversion systems.

4.2   e-XPlore

Contact: Sergey Soldatov

e-XPlore is a transportable research platform for new electricity-based low-emission synthetic fuels jointly developed by KIT and DLR. Its purpose is to validate selected options for electricity-based synthesis gas generation from carbon dioxide and water combined with selected utilization paths for converting the so-produced synthesis gas into high-quality fuels and chemicals in a modular format under the constraints of different concentration and contamination as well as electricity fluctuations in field test, i.e., for real on-site approval. Three different synthesis routes are considered as first choice options for the e-XPlore facility during its installation. Those shall further be modifiable to serve as installation basis for improved assemblies to allow other options being implemented with lower effort. Thus, e-XPlore can act as incubator for bridging the gap between lab and real environment.

In close collaboration with IMVT, IHM is supporting the elaboration and engineering of the e-Xplore synthesis route 3, which will be a container-based pilot-scale reactor concept for plasma assisted reduction of CO_2 with an overall microwave power of 12 kW. This reactor concept includes an oxygen separation stage based on a fixed-bed reactor with a redox material that allows to separate O_2 from the exhaust gas stream. For continuous operation, two parallel reactor lines with switching microwave power between those lines are envisaged. While the redox material used for oxygen separation during plasma activation of CO_2 in line one, it will be regenerated with forming gas $Ar+H_2$ in the second line and vice versa (Fig. 4.2.1). The engineering and construction of the pilot plant is finished (Fig. 4.2.2). The assembly has started recently, and commissioning of fully automated operation is projected to mid of 2025.
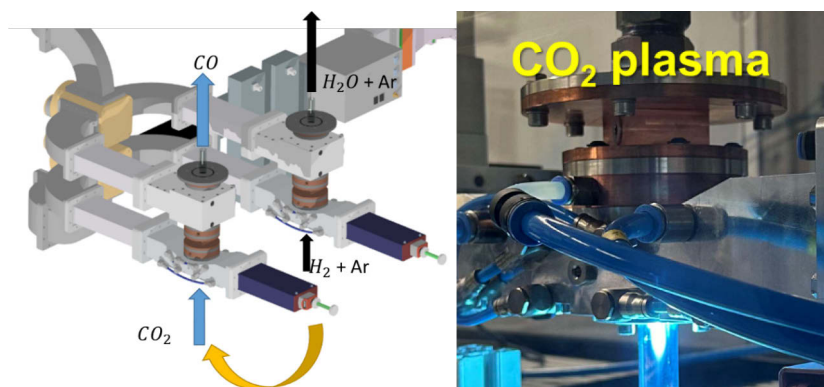

Fig. 4.2.1: CAD design of two parallel reactor lines including microwave plasma activation, plasma quenching and oxygen separation by use of redox-materials (left); corresponding lab-based set-up with CO_2 plasma (right).
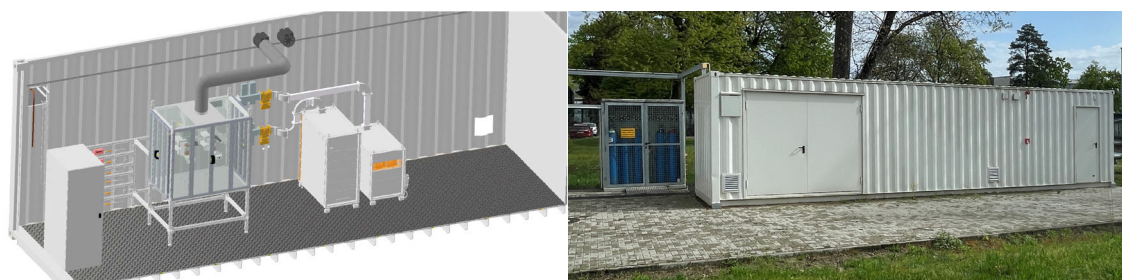

Fig. 4.2.2: CAD design synthesis route 3 (left). Container prepared for assembly or the plasma reactor (right).

4.3   MWPrint4ReCon

Contact: Moritz Engler

Carbon concrete offers the possibility of significant material savings compared to conventional reinforced concrete. On the one hand, this is possible due to the higher tensile strength of carbon fibers compared to steel, which allows comparable loads to be absorbed with smaller cross-sections. Secondly, carbon does not corrode, so there is no need for cover layers to protect the reinforcement from corrosion. The MWPrint4ReCon project aims to develop a process for the production of carbon concrete using robot-based microwave 3D Printing. With the robot-based approach large load optimized structures can be printed using continuous carbon fiber reinforced filaments. These structures require significantly higher profile cross-sections than in conventional 3D printing processes to be viable as concrete reinforcement. In conventional 3D Printing one limiting factor of print speed is the thermal conductivity of the filament. In contrast to that the volumetric nature of microwave heating makes it much less dependent of thermal conductivity. Therefore, microwave 3D printing is especially suited for printing of larger cross-section filaments.

For this project a new print head was developed which can print with filaments up to 4 mm diameter. While earlier designs used preformed filaments this approach is no longer viable at this diameter as they would be much too stiff to be fed into the printhead. To enable the filament consolidation inside the print heat commingled yarns of carbon fibers and PA6 fibers are used as a precursor. After heating inside the print head, the fiber mixture is pulled into a 4 mm nozzle where the molten PA impregnates the fibers and forms the ridged 4 mm filament.

The print head was tested on a purpose-built test stand which pulls the filament through the printhead at predefined speeds to evaluate the ideal operating parameters and their influence on the resulting profile quality. Following the evaluation on the test stand the printhead was handed over to the project partners at FAST where it was installed to the robot and successfully used to print multiple structures to test as reinforcement of concrete beams.

a)   b)
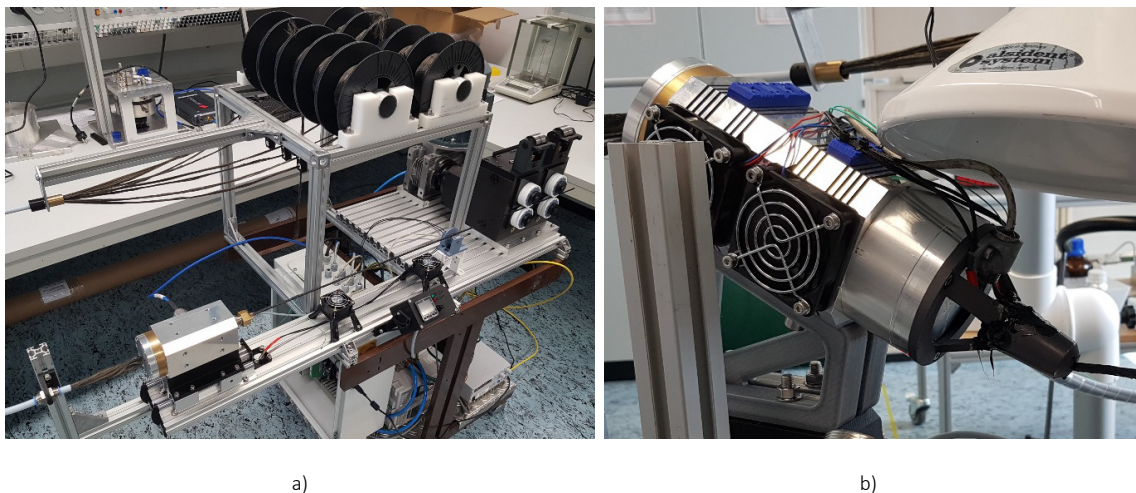
Fig. 4.3.1:   a) Test stand including print head (center left), fiber rack (top), pulling device (right) and control unit (center). b) Print head during pultrusion of 4 mm profile.

4.4   CORAERO

Contact: Jesus Nain Camacho Hernandez

The COVID-19 pandemic, caused by SARS-CoV-2, led to over 774 million cases and seven million deaths globally by January 2024, highlighting the continuing need for the development of innovative and effective technologies to prevent virus transmission and manage future pandemics effectively. The Helmholtz CORAERO project brings together a multidisciplinary group of scientists from virus biology, medicine, applied physics, chemistry, and engineering to understand virus spreading through aerosols and designing technical and administrative measures for mitigation, detection and virus control. The IHM participates in the CORAERO project, by researching on air purification systems that utilize microwave radiation to reduce virus load in enclosed spaces, targeting airborne viruses in public and private ventilation systems. Current research focuses on two distinct approaches for virus inactivation via structural damage, specifically employing moderate electric fields or microwave heating of high-efficiency particulate air (HEPA) filters.

In a biosafety level 3 laboratory, research has been conducted to investigate the inactivation of the active SARS-CoV-2 virus utilizing a resonant cavity as depicted in Fig. 4.4.1 (left). This cavity was designed to generate a uniform electric field of moderate strength along the flow channel transporting aerosols laden with SARS-CoV-2. This virus inactivation approach is designed to avoid air heating in ventilation systems and to reduce operational costs. Current efforts are dedicated to adjusting the experimental setup to work with various aerosol flow rates at different humidity levels.

On the other hand, the project also studies virus inactivation through energy-efficient microwave heating of virus-laden aerosols captured and circulating through filter media. This heating method aims at sterilizing pathogenic aerosols, a vital measure to inhibit virus re-entrainment into exhaust air or to avert infections during filter replacement or disposal. The considered filter media comprise tailored non-woven filters and custom ceramic hierarchical pore structures, as shown in Fig. 4.4.1 (right). Numerical calculations are employed to investigate the flow characteristics and effective permittivity of both filter types. From these studies, mixing relations that consider the filter structure geometry were formulated to estimate the effective permittivity of both fibrous and porous media. Subsequently, the design phase will focus on developing microwave applicators for uniform and efficient heating of the studied filters.
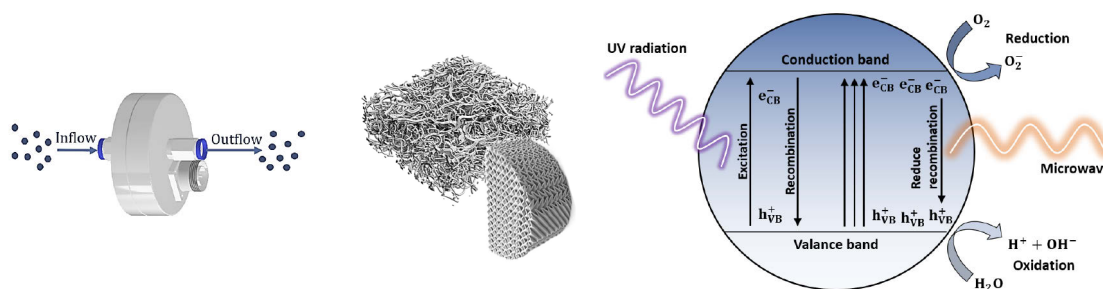

Fig. 4.4.1:   (left) Microwave cavity enhancing E-fields for virus inactivation, (right) aerosol filter media illustrating non-woven fibers and ceramic structures being investigated for efficient microwave-heating, and (center) microwave assisted photocatalysis to enhance hydroxyl production.

4.5 PAMiCo - Weed control with high-power microwaves

Contact: David Tomsu

In farming production, weeds compete with crops for sunlight, space, nutrients and water. The estimated global crop production loss due to weeds is 12%, even though there is an estimated amount of 2 million tons of pesticides applied globally. This is not only impairing the environment, but also human health. Weed control with high-power microwaves is an environmentally friendly candidate to reduce pesticide use. As part of an IraSME funded project, IHM is in charge of the development and the demonstration of a novel phased-array antenna at 5.8 GHz, which will allow to focus the installed microwave power to the weed location, which is identified before by an intelligent image recognition system. In the final application the antenna system will traverse the field on a vehicle and will be facing downwards to actively direct the microwave energy towards weeds at ground level. The sudden volumetric heating caused by the high-power density of the microwaves will lead to a bursting of the plant cells. In Fig. 4.4.1, the test stand for the validation of the slotted waveguide phased-array antenna connected to the phase-shifting system for active steering of the antenna's main beam and the measuring probe is shown. In Fig. 4.4.2 the nicely focused field profile of the zero phase-shift center position can be observed. The measured profile of the beam steering with a previously computed phase-shift distribution applied to each element of the array can be seen in Fig. 4.4.3. As the beam focusing and steering has been demonstrated at IHM, in the final steps of the project, the system will be fully integrated and prepared for field testing by our project partners.

Fig. 4.5.1: Test stand for measuring antenna characteristics using digital signal generators with phase shifting and the slotted waveguide array antenna (left) and a WR159 receiving antenna probe fixed to a xyz positioning stage (middle). Measured zero phase-shift x-y plane field profile at a distance of 50 cm to the antenna. Most of the energy is nicely focused in the center (right).
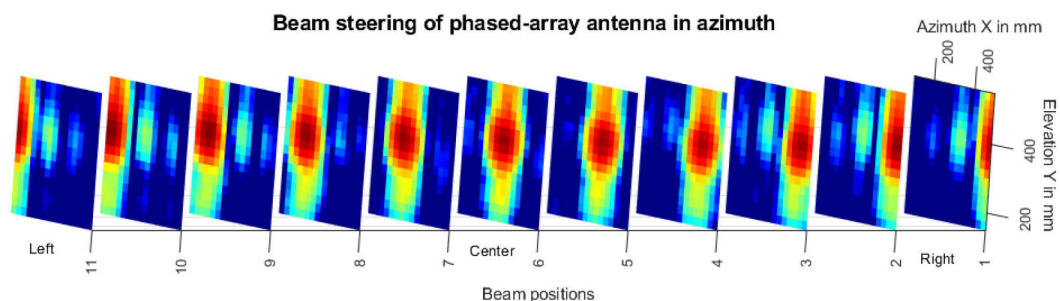

Fig. 4.5.2: Measured x-y plane field profiles at a distance of 50 cm from the antenna showing the beam steering in azimuth.

Journal Publications

Omrani, A.; Link, G.; Jelonnek, J. (2023). A Near-Field Focused Phased-Array Antenna Design Using the Time-Reversal Concept for Weed Control Purpose. arxiv. doi:*10.48550/arXiv.2302.01012*

Li, N.; Link, G.; Jelonnek, J.; Ong, S. K. (2023). Digital Twins towards Microwave-assisted 3D Printing of Continuous Carbon Fiber Reinforced Composites. Procedia CIRP, 119, 158–163. doi:10.1016/j.procir.2023.03.088

Zhang, Y.; Xuan, Y.; Yadav, R.; Omrani, A.; Fjeld, M. (2023). Playing with Data: An Augmented Reality Approach to Interact with Visualizations of Industrial Process Tomography. Human-Computer Interaction – INTERACT 2023 – 19th IFIP TC13 International Conference, York, UK, 28th August – 1st September 2023, Proceedings. Ed.: J. Abdelnour Nocera, 123 – 144, Springer Nature Switzerland. doi:10.1007/978-3-031-42283-6_7

Magro Togashi, M.; P. Fernandez Perdomo, C.; Link, G.; Jelonnek, J.; Herta G.A. Kiminami, R. (2023). Densification kinetics and in situ electrical resistivity measurements of hematite nanopowders during high frequency microwave sintering. Ceramic Materials - Present and Futur. Ed.: A. Borell, IntechOpen. doi:10.5772/intechopen.1001853

Engler, M.; Link, G.; Jelonnek, J. (2023). An Easy Method to Determine the Effective Conductivity of Carbon Fiber Composites Using a Wall Perturbation Approach. Materials, 16 (6), Art.-Nr.: 2404. doi:10.3390/ma16062404

Hernandez, J. N. C.; Link, G. (2023). Modelling of the effective permittivity of anisotropic filament structures. 2022 8th International Engineering, Sciences and Technology Conference (IESTEC), Panama, Panama, 19-21 October 2022, 740–746, Institute of Electrical and Electronics Engineers (IEEE). doi:10.1109/IESTEC54539.2022.00121

Malashchuk, V.; Walter, S.; Engler, M.; Hagen, G.; Link, G.; Jelonnek, J.; Raß, F.; Moos, R. (2023). Reducing Cold-Start Emissions by Microwave-Based Catalyst Heating: Simulation Studies. Topics in Catalysis. doi:10.1007/s11244-023-01788-6

Rybakov, K. I.; Mahmoud, M. M.; Link, G. (2024). Analysis of microwave heating of copper powder compacts. Materials Chemistry and Physics, 322, Artklnr.: 129548. doi:10.1016/j.matchemphys.2024.129548

Appendix

Equipment, Teaching Activities and Staff

IHM is equipped with a workstation cluster and a large number of experimental installations: KEA, KEA-ZAR, three GESA machines, eight COSTA devices, one abrasion and one erosion teststand, a gyrotron test facility including a microwave-tight measurement chamber and two teststands for gyrotrons, one compact technology gyrotron (30 GHz, 15 kW CW), several 2.45 GHz applicators of the HEPHAISTOS series, one 0,915 GHz, 60 kW magnetron system, one 5.8 GHz, 3 kW klystron installation and a low power microwave laboratory with several vectorial network analysers, a plasma laboratory with 2,45 GHz atmospheric plasma sources up to 6 kW and a laboratory for microwave assisted 3D printing of continuous fibre reinforced filaments.

The project FULGOR, targeting for a renewal of the KIT gyrotron teststand is progressing. In 2013, an agreement on the project structure including the involvement of the KIT project and quality management has been achieved. The final start of the procurement of the equipment was in 2014 whereas the first initial test of operation was starting in 2021.

Prof. John Jelonnek, strongly supported by Dr.-Ing. Alexander Marek has continued to teach the lecture course entitled "High Power Microwave Technologies (Hochleistungsmikrowellentechnik)" for Master students. In 2023/2024, additionally, Prof. John Jelonnek has started to teach part of the lecture course "Lineare elektrische Netze (LEN)" for undergraduate students. The lecture course LEN is coordinated by Prof. Sebastian Kempf of the Institute of Micro- and Nanoelectronics Systems (IMS). Prof. Georg Müller has continued to teach the lecture on "Pulsed Power Technologies and Applications" at KIT. Dr. Gerd Gantenbein has been teaching in 2023 the part "heating and current drive" of the lecture "Fusionstechnologie B" by Prof. R. Stieglitz, IFRT. Dr.-Ing. Martin Sack hold the lecture course "Elektronische Systeme und EMV".

At the turn of the year 2024/2025 the total staff with regular positions amounted to 38 (20 academic staff members, 10 engineers and 8 technical staff member and others). Additionally,15 academic staff members, 2 engineer and 2 technical staff members (and others) were financed by acquired third party budget.

In course of 2023/2024, 4 guest scientists, 20 doctoral students (1 of KIT-Campus South, 14 of KIT-Campus North, 5 others), 2 DHBW students, 3 trainees in the mechanical and electronics workshops worked at IHM. 2 Master students, 2 Bachelor students, 20 student assistants and 4 Research internships were supervised at IHM during 2022/2024.

Strategical Events, Scientific Honors and Awards

- Prof. Dr. Dr. h.c. mult. Manfred Thumm was awarded an honorary doctorate from the V. N. Karazin Kharkiv National University.

- Dr.-Ing. Alexander Marek was awarded the VDE-ITG 2023 Dissertation Prize for his dissertation entitled "New Type of sub-THz Oscillator and Amplifier Systems" in Berlin.

- Mr. Louis Müller was named the best of his class by the Baden-Württemberg Cooperative State University Karlsruhe as part of his bachelor's degree in mechanical engineering with a focus on design and development due to his outstanding examination performance.

Longlasting Co-operations with Industries, Universities and Research Institutes

- Basics of the interaction between electrical fields and cells (Bioelectrics) in the frame of the International Bioelectrics Consortium with Old Dominion University Norfolk, USA; Kumamoto University, Japan; University of Missouri Columbia, USA; Institute Gustave-Roussy and University of Paris XI, Villejuif, France; University of Toulouse, Toulouse, France, Leibniz Institute for Plasma Science and Technology, Greifswald, Germany.

- Cooperation on the technological development of a sodium liquid metal battery as an electrical storage device with DLR and the Huazhong University of Science and Technology – HUST in Wuhan (China).

- Development of protection against corrosion in liquid metal cooled reactor systems in the following EU-Projectes: GETMAT, IL TROVATORE (Partner: CEA, ENEA, SCK-CEN, CIEMAT).

- Development of large area pulsed electron beam devices in collaboration with the Efremov Institute, St. Petersburg, Russia (on hold).

- Development of advanced 1.5 MW gyrotrons, gyrotron for multi-purpose operation and new gyrotron control techniques for the ECRH System at the stellarator Wendelstein W7-X in collaboration with the Max-Planck-Institute for Plasmaphysics (IPP) Greifswald.

- Development of the European gyrotrons for ITER in the frame of the European GYrotron Consortium (EGYC) and coordinated by Fusion for Energy (F4E). The other members of the Consortium are EPFL Lausanne, Switzerland, CNR Milano, Italy, ENEA, Frascati, Italy, HELLAS-Assoc. EURATOM (NTUA/NKUA Athens), Greece. The industrial partner is the microwave tube company Thales Electron Devices (TED) in Paris, France.

- Development of 105 GHz 1 MW gyrotrons for WEST in collaboration with EPFL, Lausanne, Switzerland and CEA, Cadarache, France.

- In frame of EUROfusion, collaboration with EPFL Lausanne, Switzerland, CNR Milano, Italy, ENEA, Frascati, Italy, HELLAS-Assoc. EURATOM (NTUA/NKUA Athens), Greece and the industrial partner Thales Electron Devices (TED), Paris, France to develop gyrotrons for future European DEMOstration fusion power plant. EUROfusion is a consortium of national fusion research institutes located in the European Union, the UK, Switzerland and Ukraine.

- Development of Microwave Systems of the HEPHAISTOS Series for materials processing with microwaves with the Company Vötsch Industrietechnik GmbH, Reiskirchen.